UNIVERSITY OF TRENTO

MATHEMATICAL PHYSICAL AND NATURAL SCIENCE FACULTY

PhD THESIS IN PHYSICS

Cicle XXIII

Surface functionalization and characterization of diamond thin films for sensing applications

Thesis presented by:
Mrs. Simona Torrengo

Supervisor:
Prof. Antonio Miotello

Co-supervisor:
Dr. Giorgio Speranza

PhD coordinator: Prof. Lorenzo Pavesi
Academic years 2007 - 2010

“Contro le infamie della vita le armi migliori sono:
la forza d’animo, la tenacia e la pazienza.
La forza d’animo irrobustisce, la tenacia diverte e la pazienza da pace. ”
H. H.

Contents

Chapter 1

Introduction

Diamond possesses such out standing properties that its exploitation in many fields is desired and sought for several years now. It is famous among scientists for its combination of exceptional physical and mechanical properties such as high thermal conductivity, chemical inertness, optical transparency (from UV to IR), high mechanical stability and corrosion resistance. Due to its indirect optical band gap of 5.47 eV, diamond belong to the group of wide band gap semiconductors. It has a crystal structure identical to its more common relatives silicon and germanium. On first glance one might also expect similar surface properties in terms of reconstructions, surface states, and surface band diagrams. In part, this expectation is indeed fulfilled, but diamond also exhibits a number of unusual and potentially very useful surface properties [1, 2]. When the surface dangling bonds of diamond are saturated by monovalent hydrogen atoms, (donor-like) surface states are removed from the gap, the electron affinity changes sign and becomes negative and the material becomes susceptible to an unusual type of transfer doping where holes are injected by acceptors located at the surface instead of inside the host lattice. The negative electron affinity is used to fabricate cold cathode, while the diamond surface conductivity allows to use diamond as an electrode to collect electrical signals [3, 4].

The presence of oxygen on the diamond surface has also a significant influence on chemical reactivity [5, 6], electrical conductivity [7, 8], field emission [9, 10] and Schottky barrier heights [11]. If diamond surface is terminated by oxygen atoms it exhibits a positive electron affinity (PEA) and insulating properties [12]. Various conditions for diamond oxidation were reported in the literature including thermal [13, 14], plasma [15, 16], electrochemical techniques [17, 18], singlet oxygen [19] and ozone treatment [20, 21].

Diamond is known to be biocompatible [22] and is, therefore, potentially useful for *in vivo* electronic applications. When Takahashi et al. [23] first introduced a photochemical chlorination/amination/carboxylation process of the initially H-terminated

diamond surface, a giant step towards biofunctionalization of diamond was taken. After that, many other methods were introduced, as a photochemical method to modify nanocrystalline diamond surface using alkenes [24], followed by electrochemical reduction of diozonium salts which has been successfully applied to functionalize boron-doped ultrananocrystalline diamond [25] and recently, direct amination of diamond has been introduced [26] called *one step method*. In particular the *one step method* is very promising because allows to produce functionalized surfaces for DNA micropatterning by photolithography. It is based on the fact that amine groups are directly produced when diamond surface is exposed to UV irradiation in ammonia gas.

All these particular behaviours has made diamond a promising candidate for bio-electronics and some bio-devices, as field effect transistors [27, 28], ISFET (*Ion-sensitive field effect transistor*) [29,30] or other types of bio-applications [31–33] have been already realized.

An ideal biosensor should combine surface properties and bulk properties such as extreme mechanical hardness and, even more important, peculiar optical properties. The broad optical transparency of diamond, from the deep ultraviolet to the far infrared, makes it a suitable candidate for bio-devices, also because it could make possible simultaneous recording of electrical and optical signals from specifics chemical reactions happening on the surface. Even more, the possibility to use UV radiation to change the surface chemistry of diamond, and so its surface properties, is very promising because it is compatible with semiconductor technology in common use to day.

With the aim of exploiting the potentialities of this last proposal, in this thesis work nanoscrystalline optical properties of diamond and two recent new NCD functionalisation techniques involving UV light (*one step method* and photochemical oxidation) have been investigated. Firstly the oxidation of diamond surface caused by the irradiation of the surface with UV-light in oxygen atmosphere was considered. Two different experiments *in situ* were realized in order to understand the physic-chemistry of this method. The chemical bonds between oxygen and surface carbon atoms were investigated by firstly performing an annealing treatment in ultra hight vacuum of a oxidized UV surface and then comparing the obtained result with annealing treatments of two different oxygenated diamond surfaces using other two techniques: plasma oxidation and piranha solution oxidation.

An other interesting aspect on which clarity has to be made deal with amination process of diamond surface. In fact experimental data from literature show that ammonia functional groups are always accompanied by the presence of oxygen, which however degrades the NCD conductivity. As a first fundamental step, the efficiency on hydrogenated diamond surface was investigate. Successively the role of oxygen in the chemistry of amination process was studied performing *in situ* experiments

using different terminated diamond surface (hydrogenated, chemically oxidized, UV oxidized) and different gaese (pure NH_3 or $NH_3 + O_2$).

Concerning the spectroscopic technique employed for the diamond characterization, the choice was done on the basis of an important necessity. Since diamond electrical and chemical properties are strictly related to its surface termination, a surface non destructive analysis technique is essential to check its status. Among all the possible surface techniques, in this work, XPS (*X-ray Photoelectron Spectroscopy*) and UPS (*UV-ray Photoelectron Spectroscopy*) are the most suitable, since their scanning depth is nearly 3 nm and 1.5 nm respectively [34, 35]. UPS gives information about the valence band electronic states instead XPS gives information not only about chemical species present onto diamond surface, but it can also states how these atoms are linked together, thanks to their *chemical shift*.

Chapter 2

The diamond

In this chapter the diamond properties will be introduced with particular emphasis to the surface properties. Methods to modify the diamond surface chemistry will be shown in the next section 2.3.

2.1 Structure and *bulk* diamond properties

Diamond is one of the most precious gemstone and for centuries and it has aroused admiration for its exceptional brillance. Recently diamond has attracted attention of many research groups because, compared to other materials, provides an impressive combination of chemical, physical and mechanical properties suitable for several applications.

Diamond is also known for its extreme hardness, it has high Young modulus and it has the highest thermal conductivity at room temperature. It exhibits an exceptional wear resistance and a low coefficient of friction. These properties make synthetic diamond an ideal choice for highly demanding applications such as cutting tools for non-ferrous materials, surgical knives and wear resistant coatings.

Besides the mechanical properties, diamond possess also interesting electrical properties. It is a semiconductor characterized by a wide bandgap of 5.45 eV which coupled to its thermal conductivity useful in high power electronics and optoelectronic applications [28, 36], [37, 38]. The wide bandgap results also in high transparency in a wide wavelength range: diamond shows high trasmittance from UV to IR wavelengths. Furthermore chemical inertness and biocompatibility are suitable for electrochemical and biological applications [39, 40].

Properties listed above and summarized in tab. 2.1, are commonly defined *bulk* properties. They are, in fact, the consequence of the coupling of the atomic properties of carbon atoms and the specific crystalline structure assumed. Carbon atoms may assume two distinct allotropic forms: graphite and diamond. In the former, which is

Table 2.1: Diamond bulk properties [2].

Property	Diamond
Lattice constant (nm)	0.36
Mechanical Hardness (g/mm^2)	5700 - 10400
Dielectric constant	5.7
Thermal conductivity (W/cmK)	22
Young Modulus (GPa)	1143
Bandgap (eV)	5.45
Type	indirect
Work function (eV)	4.81
Electrical resistivity (Ω/cm)	$> 10^{11}$
Optical trasmission	220 nm $\leq \lambda \geq$ 2500 nm and $\lambda \geq$ 6000 nm
Biocompatibility	Yes

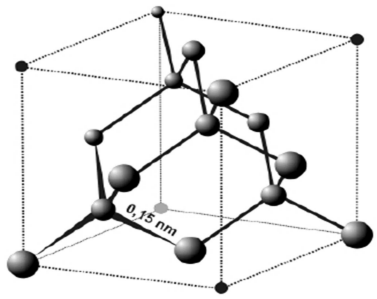

Figure 2.1: Diamond structure.

the more stable allotrope, carbon atoms are arranged in a hexagonal lattice. Diamond becomes the more stable allotropic configuration of carbon at high temperature and high pressure. It typically crystallize in the face-centered cube (FCC) (fig. 2.1) lattice with two atoms per primitive unit cell. The unit cell of diamond, with a side length a_0 approximately equal to 3.567 Å at room temperature [41]. The unit cell has a two atom basis at (0, 0, 0) and (1/4, 1/4, 1/4), which means half of the atoms are at lattice points and the other half are offset by (1/4, 1/4, 1/4), where 1 is the length of a side of the unit cell [42].

In the lattice structure, each carbon atom is tetrahedrally coordinated forming strong bonds to its four neighbors using hybrid sp^3 atomic orbitals, with equal angles of 109 ° to each other. Each tetrahedron combines with four other tetrahedre leading to the FCC crystalline structure. The covalent bonding between carbon atoms is

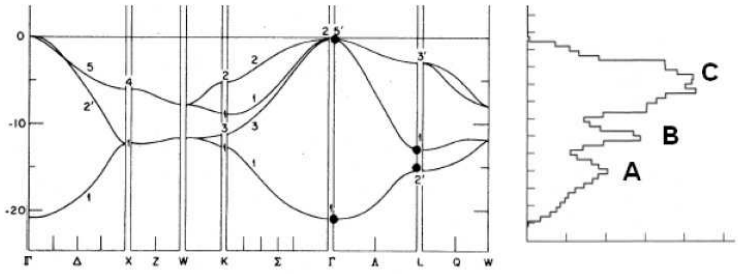

Figure 2.2: Diamond band diagram and DOS [43].

characterized by a small bond length of 1.545 Å and a high bond energy of 711 KJmol^{-1} [42]. The atomic density is 1.76 $\times 10^{23}\, atoms/cm^3$, while the diamond's density is 3.52 gcm^{-3}.

Thanks to the FCC symmetry has several crystalline shapes (habits) may be generated. They include the [100] cube, the [110] dodecahedron and the [111] octahedron. The structure of diamond characterized by a high molar density coupled to the very strong chemical bonding, leads to the aforementioned unique mechanical and elastic properties. For this reason, compared to other materials, diamond displays the highest thermal conductivity and sound velocity and the lowest compressibility and bulk modulus. Turning to electronic properties, as observed diamond is a wide indirect gap semiconductor. When not doped with impurities it is therefore a highly insulating material showing resistivity up to 10^{15} Ωcm. Diamond possess also a high breakdown electric field of 10 MV/cm, high carrier mobility of 4500 cm^2/Vs and 3800 cm^2/Vs (for electrons and for holes respectively) and low dielectric constant of 5.7. The band diagram of diamond (fig. 2.2) is similar to that of silicon. It is characterized by six equivalent electron minima located along the [100] k-axes, the valence band maximum at Γ - point (K = 0) and conductance band minimum at approx. 80 % of X-point position. It is possible to obtain the Density of State integranting the band diagram. The DOS is composed by three peaks:

- C peak is due to bonds σ_p;
- B peak is a typical structure of the diamond because it depends on hybridized sp^3;
- A peak is due to bonds σ_s.

Each of these three peaks can be associated with one or more points symmetry of the first Brillouin zone. The DOS corrected for the orbital cross section, is mirrored by photoemission spectra obtained form the Valence Band (VB) [44]. This enables one

to follow changes of the electronic structure by analyzing UV- or X-ray photoemission VB spectra.

In spite of its exceptional properties the use of diamond has been limited by high costs due to the scarcity of raw materials and to the strong selection to find the gems satisfying the high purity, low defect content requirements.This is why in recent years developed have techniques to produce diamond by artificial crystals growth.

2.2 Synthetic diamond

The development of the synthetic processes is a result of the extensive research during the 1940's and a detailed knowledge of the carbon phase diagram (fig. 2.3) developed by O. I. Leipunskii [45].

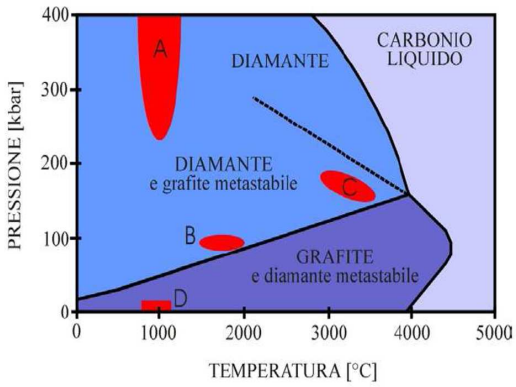

Figure 2.3: Carbon phase diagram with temperature and pressure ranges corresponding to various diamond synthesis process, as indicated by the shaded area [46].

The first public announcement of successful diamond synthesis was made by the *General Electric Corporation* in 1955. They developed the *High Pressure High Temperature* (HPHT) method [47] in which the synthesis of diamond essentially duplicates the natural process by converting graphite into diamond under conditions at which diamond is the thermodynamically favored phase. The General Electric breakthrough was the use of a *bell* press, which was capable of producing pressure above 10 GPa and temperatures above 2000 ℃. The *bell* press used a pyrophyllite container in which graphite was dissolved within molten nickel, cobalt or iron. Those metals acted as a *solvent-catalyst*, which both dissolved carbon and accelerated its conversion into diamond. This technique provides reproducibility and tailorability unavailable in natural diamonds in terms of chemistry, morphology, size, shape and toughness. The HPHT disadvantage is that the maximum obtainable crystal size is limited to few millimeters and the diamond crystals contain always impurities from

the growth environment. This type of diamond is too expensive and the small area and the nitrogen impurities become it no important for electronic applications. Even if these crystals are currently produced their use is mostly confined in the research labs, to few niche applications such as high energy radiation detectors and jewelry. Research in the HPHT synthesis of diamond is still underway in an effort to lower production costs and produce even larger crystals. The difficulties in the direct conversion of graphite to diamond has triggered the development of alternative processes to lower the temperature and pressure.

A second breakthrough came with the discovery by Angus [48] and W. G. Eversole [49] of the *Union Carbide Corporation* in the U.S.A. and by B. Derjaguin [50] in USSR, that diamond could be deposited on a substrate by *Chemical Vapor Deposition* (CVD). This method involves a gas-phase chemical reaction occurring above a solid surface causing deposition onto that surface. Working at low pressure and high temperature, where carbon is in a metastable regime both diamond and graphite may be produced. Growth conditions can be carefully tuned to reduce graphite formation and favor diamond growth.

A large variety of carbon-containing gas species have been employed to synthesize diamond by CVD. These include methane, aliphatic and aromatic hydrocarbons, alcohols, ketones, amines, ethers and carbon monoxide with methane being the most frequently used reagent. In addition to these carbon carriers, the gas phase usually must contain powerful both non-diamond carbon etchants and surface site preparation species such as hydrogen, oxygen or fluorine atoms.

It has been observed that a necessary condition for diamond growth to occur is the presence of a gas-phase non-equilibrium in the region adjacent to the deposition substrate. The gas-phase non-equilibrium is generated through gas-phase activation achieved typically using one of the three basic methods:

- external heating as in hot-filament CVD ;
- plasma activation as in plasma assisted CVD ;
- a combination of thermal and chemical activation as in flame CVD .

While each method differs in detail, they all share features in common. For example, growth of diamond normally requires the substrate to be maintained at a temperature in the range 1000 - 1400 K, and the precursor gas be diluted in an excess of hydrogen. Carbon containing gas and molecular hydrogen are dissociated by the activation energy, forming carbon radicals and atomic hydrogen, which drift toward the substrate by a gradient in temperature and concentration (fig. 2.4). The diamond growth is based on the gas phase chemical reactions which happening on the substrate surface involving carbon atoms deposited either in the form of diamond and graphite. Diamond growth takes place due to the different reaction rate

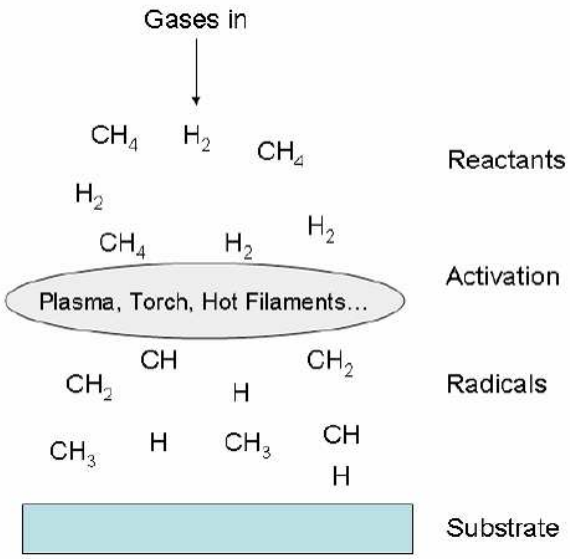

Figure 2.4: Schematic CVD diamond process; the main chemical species are shown.

between hydrogen-graphite and hydrogen-diamond; in optimized conditions atomic hydrogen removes graphite much faster than diamond, therefore leading to diamond growth. Roughly, the reactant gases form C_xH_y radicals and atomic hydrogen at the substrate surface these compounds undergo a series of reactions leading to sp^2 (graphite) and sp^3-carbon (diamond). The sp^2 bonds are removed by atomic hydrogen, which additionally terminates and stabilizes the sp^3 bonds. The chemical reactions occurring in the gas phase are complex and a comprehensive understanding of the growth mechanism is still needed.

An important contribution came in 1994 from Bachmann who drew the diagram illustrated in figure 2.5, which is now known as the *Bachmann triangle diagram*. The Bachmann diagram collects data from more than 70 experiments using different process gases and different growth techniques. The diagram shows that, diamond grows only in the region around the H-CO line. This result led Bachmann to conclude that diamond growth is independent of the gaseous precursors used because these are rapidly broken and converted to reactive components which are the responsible elements of the growth mechanism, as also stated by P. May in 2000 [51]. Of particular interest is the bottom left region, which represents a few percents of methane in hydrogen atmosphere; this is indeed the most common gas mixture used in CVD diamond growth, with methane concentration usually between 0.3 % and

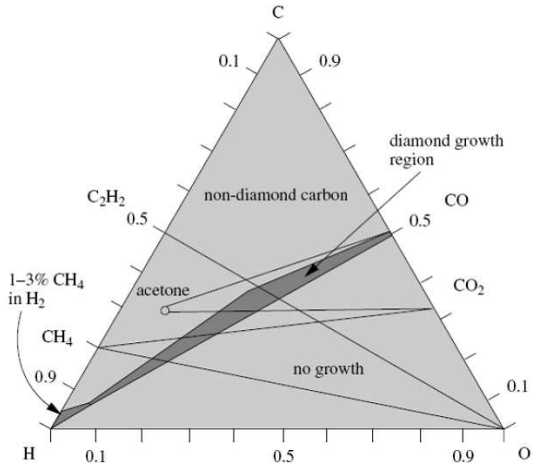

Figure 2.5: Bachmann triangle diagram.

5.0 % according to the activation energy and to the desired diamond quality. In the past 20 years many other studies have been carried out on the diamond CVD gas chemistry. The fundamental reactions are accredited to involve acetylene C_2H_2 and methyl radical CH_3, which are produced by the following reactions:

$$CH_4 + H \leftrightarrow CH_3 + H_2; \tag{2.1}$$

$$2CH_3 \leftrightarrow C_2H_6; \tag{2.2}$$

$$C_2H_6 + 2H \leftrightarrow C_2H_4 + 2H_2; \tag{2.3}$$

$$C_2H_4 + 2H \leftrightarrow C_2H_2 + 2H_2. \tag{2.4}$$

Other methyl groups CH_x and C_xH_y are also found to have a role in diamond growth. The reactions 2.1, 2.2, 2.3 and 2.4 are promoted from left to right in the proximity of the activation energy and from right to left on the substrate surface; the left to right reaction is however faster and thus a non equilibrium is created in the proximity of the substrate surface, where C_2H_2 and CH_3 are not completely converted and tend to precipitate on the substrate.

In figure 2.6 the schematic diamond growth process due to CH_3 is shown as proposed by P. May [51]. Here diamond growth is represented as a stepwise process where two carbon atoms are added to the lattice and locked in diamond bonds by double CH_3 absorption.

The H atoms are believed to play a number of crucial roles in the CVD process:

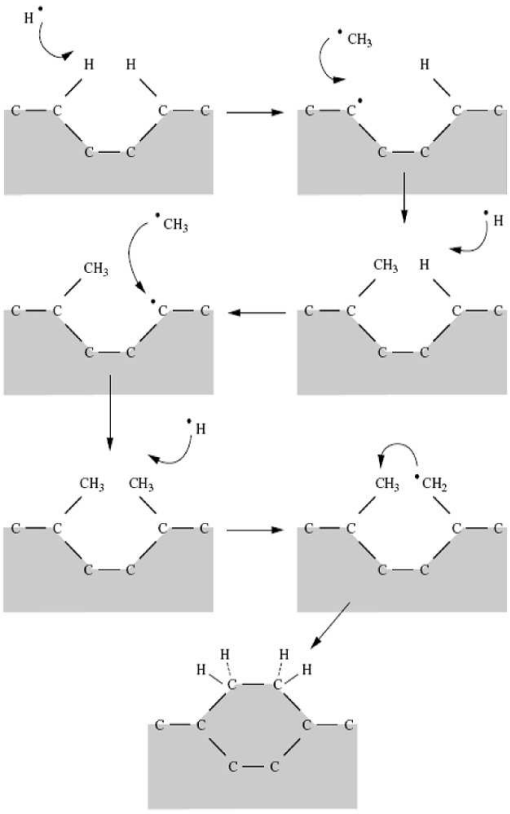

Figure 2.6: Schematic diamond growth due to addition of CH_3.

- they undergo H abstraction reactions with stable gas-phase hydrocarbon molecules, producing highly reactive carbon-containing radical species. This is important, since stable hydrocarbon molecules do not react to cause diamond growth. The reactive radicals, especially methyl (CH_3) can diffuse to the substrate surface and react, forming the C-C bond necessary to propagate the diamond lattice;
- H-atoms terminated the *dangling* carbon bonds on the growing diamond surface and prevent them from cross-linking, thereby reconstructing to a graphite-like surface;
- atomic hydrogen etches both diamond and graphite. As observed, under typical CVD conditions, the rate of diamond growth exceeds its etch rate. This is believed to be the basis for the preferential deposition of diamond rather graphite.

The concept of applying catalytic processes to diamond CVD has not attracted

close attention. This is due primarily to the difficulty of controlling the chemistry in an already complex and poorly understood process involving atomic hydrogen and hydrocarbon species. In this situation the development of an efficient catalyzer requires considerably more time and effort in spite of the potential importance of the approach from an energetic and economic viewpoint.

In CVD diamond, the [111] octahedral faces are observed at low temperatures and low hydrocarbon concentrations; the [100] cubic faces predominate at high temperatures and high hydrocarbon concentrations. Generally cubo-octahedral crystals combining both these faces are found. Using CVD processes, thin polycrystalline diamond films are obtained. These materials are identified as nanocrystalline diamond (NCD) films even if the crystallite dimension is of some hundreds of nanometers.

Recently it has been discovered that replacing almost completely hydrogen with argon it is possible to grow poly-crystalline diamond with grain size below 5 nm. Such material is called ultra nano-crystalline diamond UNCD [52].

2.2.1 Nano-crystalline Diamond (NCD)

Nano-crystalline diamond is by definition a heterogeneous material with a mixture of diamond, graphite and amorphous carbon phases. The diamond phase is constituted by nano crystals with different orientation. Many studies demonstrated that (100) and (111) are the most present because (110) surface is unstable under CVD growth and gas phase etching processes.

The diamond crystal arrangement has been investigated firstly by C. Wild et al. in 1993 [53] when they first introduced the α parameter, which is the ratio between the growth speed of [100] and [111] orientations:

$$\alpha = \sqrt{3}\,\frac{V_{100}}{V_{111}}. \tag{2.5}$$

The α parameter defines the shape of one diamond grain, which results to be cubic for $\alpha = 1$, octahedral for $\alpha = 3$ and a combination of these shapes for α between 1 and 3. Wild et al. have also correlated the α parameter with the substrate temperature and the CH_4/H_2 ratio [54] defining suitable growth conditions for different NCD configurations. In particular for $\alpha < 1.5$ we have the so called 2D grains arrangement.

In the 2D type (fig. 2.7 A) diamond crystals have an elongated shape along the growth direction and form a columnar grain structure where some of the initial crystals, from the nucleation process, prevail and continue to grow uninterruptedly. These crystals also tend to become larger during the growth and thus the final grain size of 2D NCD depends on the layer thickness.

If $\alpha > 3$ results 3D NCD structure (fig. 2.7 B). Diamond grain have isotropic shape and the resulting structure has no preferential directions. In this configuration

the grain size remains constant during growth and is therefore independent of the layer thickness.

The diverse arrangement and different concentration of the phases may change NCD properties drastically so it is important to gain a comprehensive knowledge about the growth conditions having thus the opportunity to grow the most suitable NCD film for the designed application.

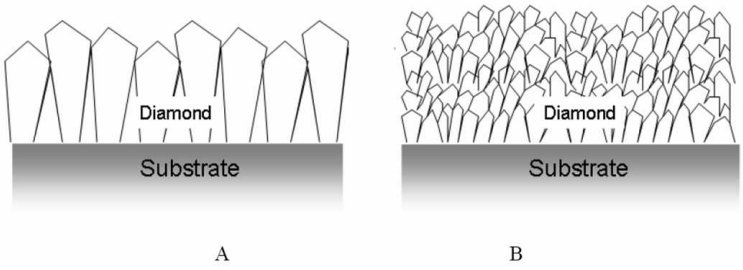

Figure 2.7: A: 2D structure NCD. B: 3D structure NCD.

2.3 Diamond surface

Diamond exhibits a number of unusual and very useful surface properties depending on the surface dangling bonds saturation by hydrogen or oxygen atoms.

The most important crystallographic orientations are (100) and (111) which can be selectively grown by CVD when process parameters are thinly controlled. The crystallographic orientation (110) being is unstable under CVD growth and gas phase etching processes is less frequent [12].

2.3.1 Clean surface

In this case *clean* means with no adsorbates on top of the surface. A diamond (100) surface contains two dangling bonds per surface atom. They can lower their energy considerably by forming mutual bonds. As a consequence, the clean diamond surface is unstable in the 1 x 1 geometry and reconstructs into a 2 x 1 geometry (fig. 2.8) with neighboring atoms forming π-bonded dimers. In a simple tight-binding scheme the coupling of surface dangling bonds in π-bonded dimers induces a bonding-antibonding splitting between occupied and unoccupied (dimer) π orbitals. The dimers themselves are arranged in rows and interact with each other. This causes a further albeit weaker splitting of the dimer orbitals. This ends up in the formation of the surface band structure with an occupied band originating from the π (bonding) orbital and an empty band originating from the π (antibonding) orbital. As a consequence of the rather large distance of 2.52 Å maintained between

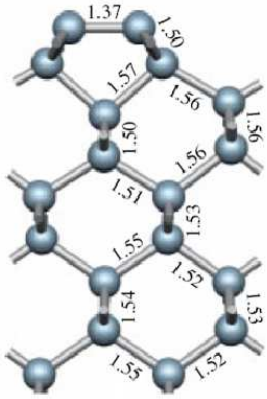

Figure 2.8: Atomic geometries for the clean (100)-(2 x 1) diamond surface.

the surface dimers, their mutual interaction which broadens the π and the π^* bands does, however, leaves a gap of 1.3 eV between occupied and unoccupied surface states so that the surface is semiconducting [55]. As an important point it should be mentioned that the occupied surface states do not extend into the band gap of diamond being placed within the valence band. Thus, they can exchange neither electrons nor holes with the diamond bulk and are electronically inactive. The structure of the occupied surface states of the (100) diamond was also measured by photoemission spectroscopy and found in good agreement with theory [56].

For the unoccupied surface states of the diamond (100)2 x 1 surface only qualitative experimental information was indirectly obtained from surface core excitons analysis via near-edge X-ray absorption [57].

The (111) surface of diamond is the natural cleaving plane of diamond and shows one dangling bond per surface atom in its bulk terminated form. This termination is not stable and undergoes a rather complicated 2 x 1 reconstruction similar to that firstly suggested by Pandey [58] for (111) Si. The uppermost C atoms form zigzag chains that run in parallel across the surface. As these atoms are only threefold coordinated, they share a delocalized π network extended along the chain, causing this (111)2 x 1 surface to exhibit semi-metallic behavior. This surface band structure was confirmed experimentally, with one important difference, however. While the theory predicts a metallic surface with occupied and unoccupied surface states merging at K in the surface Brillounin zone, angle-resolved photoemission spectra show a clear gap of at least 0.5 eV [56].

2.3.2 Oxygenated surface

Two different models were suggested for the bonding structure of the diamond (100)1 x 1:O surface:

- the *ketone* or top-site model (fig. 2.9 (a) with one oxygen double bonded to each carbon surface atom;
- the *ether* or bridge-site model (fig. 2.9 (b) with oxygen atoms connecting adjacent surface carbon atoms.

Total energy calculations find for both models almost identical values for the oxygen chemisorption energy with a slight advantage for the on-top model. Photoemission spectroscopy reveals no occupied surface states in the gap and no donor-like surface states exist in the gap.

In the case of the (111) diamond surface oxygen monolayer coverages do not lead to a surface dereconstruction, i.e. it maintains the 2 x 1 geometry of the clean surface. This result suggests that the divalent oxygen atoms may be bonded to the bridge sites of the π-bonded Pandey chains 2.3.1. This configuration, which can be considered the simplest one when starting from the clean C (111) - (2 x 1) surface, is indeed found to be stable by total energy calculations, albeit only up to half a monolayer of coverage [59]. From the same calculations, for monolayer coverages the formation of Pandey chains is suppressed and various configurations are found in which oxygen atoms are bound pairwise as molecular units onto bridge sites or top sites of the bulk terminated surface. In all such cases, however, only each second site is occupied, leading again to a 2 x 1 symmetry of the surface. This rater complicated picture for the structure of the oxygen-covered C (111) surface is exclusively based on total energy calculations. Only recently some experimental results on that surface were presented, with a focus on surface states and electron affinity. Ultraviolet-excited photoemission (UP) spectra show no indication of donor-like surface states in the gap [60].

2.3.3 Hydrogenated surface

All the as-grown CVD diamond present a hydrogenated surface because hydrogen is usually introduced in the reactor at the end in order to remove the π and π^* states deleting dimers and inducing single bonds.

In the case of (100) diamond hydrogen termination does not lead to a stabilization of the bulk terminated 1 x 1 structure and the mono-hydrogenated (100)2 x 1:H surface is widely accepted to be the most stable under normal conditions. Due to the tight diamond lattice a complete saturation of all surface dangling bonds is prevented by the steric repulsion of the hydrogen atoms as found by the majority of total energy calculations [61, 62]. Surface atoms remain arranged in dimer rows as

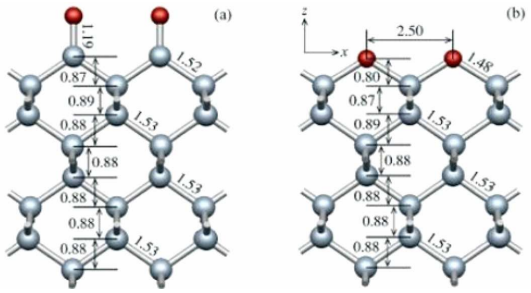

Figure 2.9: Atomic geometries for the oxygenated (100)-(1 x 1) diamond surfaces: a) *ketone* and b) *ether*.

for the clean diamond (100) surface, and only the π bond between the dimer atoms is replaced by a covalent bond to one hydrogen for each surface atom. Due to the change in bonding structure the π and the π^* states of the clean surface are replaced by bonding and antibonding states of the carbon-hydrogen bonds. The corresponding surface state bands are shifted in energy further into the valence band and toward the conduction band, respectively. From density functional theory the occupied surface states are found more than 2 eV below the valence band maximum (VBM), whereas unoccupied surface states are predicted between 3.3 and 6.0 eV above the VBM, i.e. in the upper half of the band gap and extending into the conduction band [55]. The absence of occupied surface states in the band gap of diamond (100)2 x 1:H is also confirmed by photoemission spectroscopy [56].

For the (111) surface two hydrogen-terminated structure are considered:

- the monohydride surface where each dangling bond of (111)1 x 1 is terminated by one hydrogen atom

- the trihydride surface where the dangling bond is terminated by methyl. This structure on as-grown (111) surfaces has been measured by Aizawa et al. using HREELS.

The coexistence of the two reconstruction configurations is possible on as-grown surfaces.

The formation of the covalent carbon-hydrogen bonds leads to bonding states inside the valence band till to 4 eV below the VBM. Photoemission experiments show no occupied surface states within the gap, in agreement with the calculations. Concerning unoccupied acceptor-like surface states we have again to rely on indirect information from X-ray absorption [57], or on theory which predicts antibonding C-H bands between 3.6 eV and 6.0 eV above the VBM.

2.3.4 Properties of hydrogenated surface

The hydrogenated diamond surface is the most studied because it has interesting properties such as:

- hydrophobic [63];
- electron negative affinity [64–67];
- surface conductivity [68].

Negative electron affinity

The electron affinity χ is the energy difference between the conduction band minimum E_{CBm} and the vacuum level E_0. It can be modified by chemisorbed surface atoms because generally they generate to heteropolar bonds. They carry a dipole moment whose sign and magnitude depend on the difference in electronegativity between the carbon atoms of the diamond lattice and the surface-terminating atoms [69]. Since hydrogen exhibits a lower electronegativity than carbon because the C-H bond is polarized with a positive charge δ^+ on the H atom. From basic electrostatics, a layer of such dipoles with areal density n causes an electrostatic potential step ΔV perpendicular to the surface over a distance of the order of the surface bond lengths. The potential step is proportional to the change $\Delta\chi$ in electron affinity caused by the surface dipoles [70]:

$$\Delta\chi = -e\Delta V = -ep\frac{n}{\varepsilon_0 f\,(n)}; \tag{2.6}$$

where e is the elementary charge, ε_0 is the dielectric constant of free space and p the magnitude of the dipoles. The function f which depends on n takes the interaction of dipoles into account with the result that the contribution of each dipole to ΔV is reduced for high dipole densities. An expression for *f(n)* with the polarizability α of the dipoles as a parameter can be obtained according to the calculation of Topping [71]:

$$f(n) = \left(1 + 9\alpha n^{\frac{3}{2}}/4\pi\varepsilon_0\right)^{-1}. \tag{2.7}$$

Carbon is more electronegative than hydrogen so the component p_z is positive. Using 2.6 we can calculated:

$$\chi_{sup} = \chi_{bulk} - \Delta\chi. \tag{2.8}$$

The negative electron affinity of hydrogenated diamond surface can be measured experimentally.

Surface conductivity

Undoped diamond with a band gap of 5.5 eV, is commonly considered an electrical insulator or sometimes a semiconductor with a wide band gap. Surprisingly a surface conduction of the as-grown (on both single crystals and thin films samples) hydrogenated diamond surface was observed by Landstrass and Ravi [72] in 1989. Later the presence of a conductive layer was confirmed, using the Seebeck effect, and identified as p-type by Maki et al. [73].

During the last years many other experiments have shown the same behavior on H-terminated diamonds. The surface conductivity (SC) of hydrogenated diamond is of the order of 10^{-4} to 10^{-5} $\Omega/\square$ at room temperature (RT). The areal density of the p-type carriers responsible for the conductivity is about $\rho_S = 10^{13}$ cm^{-2} and it is hardly temperature dependent between RT and 150 K. The Hall mobility of the carriers varies also little with temperature ($\approx T^{1.2}$) and is of the order of 30 cm^2 $V^{-1}s^{-1}$ with a maximum value of 70 cm^2 $V^{-1}s^{-1}$ reported for a carrier density of 1.2 10^{12} cm^{-2}.

The mechanism of surface conduction is still puzzling, but it is definitely ascertained that the conduction is related to hydrogen. So SC is associated to surface band bending due to hydrogen termination [74], hydrogen incorporation [75] and deep level passivation [76]. Since surface wet-chemical oxidationdrastically change the p-type semiconducting nature to the intrinsic insulating behavior of diamond, there is thus general agreement that the carriers are holes residing in an accumulation layer at the surface.

The depth distribution of the acceptors responsible for the hole accumulation is discussed controversially, ranging from species at the surface over layers extending up to 10 nm into the diamond. It has also been suggested that the acceptors form a layer buried 30 nm below the surface [77]. In the limit of a quasi-two-dimensional acceptor layer at or up to 30 nm below the surface, the observed areal density of 10^{13} cm^{-2} holes requires a band profile with a surface Fermi level position lying, within a few kT, at the valance band maximum (VBM) [68].

Despite the exceptional nature of SC on diamond, there is no clear understanding of the nature of the doping mechanism that leads to the surface-near hole layer. Such an understanding is, however, highly desirable in order to be able to exploit fully considerable potential of SC for applications.

Electrochemical model

The *electrochemical model* is the model that explains the SC of the diamond. The electrochemical model was explained for the first time in the article *Origin of Surface Conductivity in Diamond* by Maier et al. [68]. They give experimental evidence that hydrogen is only a necessary requirement for SC; exposure to air is also essential.

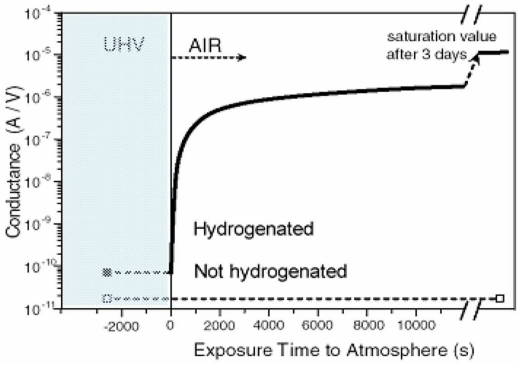

Figure 2.10: Surface conductance of the hydrogenated (masked) and the dehydrogenated (irradiated) part of a diamond (100).

Hydrogen termination of the surface bonds leads to a particular low ionization energy of 4.2 eV, in spite of the large band gap. As a consequence, hydrogenated diamond can be doped by physisorbed surface adsorbates, provided their electron affinity exceeds this value.

In order to explain this, they performed an experiment, using different types of diamond with different crystallographic orientations. The experiment consisted in the measurement of the surface conductance combined with the evidence of negative/positive Negative Electron Affinity (NEA) obtained from the total photoelectron yield spectrum. A diamond sample was annealed in UHV (Ultra High Vacuum) at $\approx$ 400 ℃ for 15 min. After the thermal treatment the conductance dropped to 10^{-10} A/V while the hydrogenation remained intact as demonstrated by the NEA property of the surface. Thermal desorption of chemisorbed hydrogen, in fact, requires temperatures higher than 700 ℃. Then the authors removed hydrogen from one half of the sample using an electron beam (1 keV, 0.2 mA/cm^2, 90 min). The untreated area still showed the fingerprint of NEA, while this feature was absent in the irradiated surface, proving that the hydrogen termination was removed and the electron affinity turned to positive. Again conductance was measured (see fig. 2.10). Both the sample halves were found in a low conductance state which persisted as long as diamond was kept in UHV. However, when the sample was brought up to air, the conductance of the hydrogenated area rised by 4 orders of magnitude in a time of $\sim$ 0.5 hours and increased more slowly until 10^{-5} A/V after three days. By contrast, the dehydrogenated part of the sample remained in its low conductance state with no sign of change whatsoever. This experiment clearly demonstrates that the hydrogenation of diamond is a necessary but not a sufficient condition for high surface conductivity. An additional ingredient that is coming from the air and that thermally desorbs in UHV above 400 ℃, is necessary.

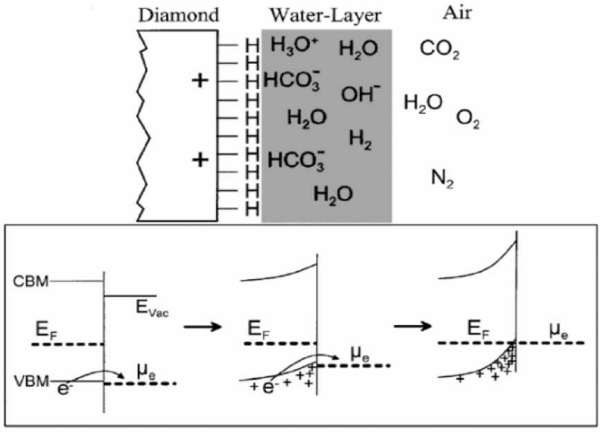

Figure 2.11: Evolution of band bending during the electron transfer process at the interface between diamond and the water layer [78].

In order to act as an acceptor, the adsorbate must have its lowest unoccupied electronic level below the VBM of diamond. With an electron affinity $\chi_{C:H}$ = -1.3 eV for hydrogenated diamond, this requirements sets a lower limit for the $\chi_{ad} = (E_g - 1.3)$ eV = 4.2 eV, where E_g = 5.5 eV is the band gap energy of diamond. Electron affinities of molecular atmospheric species lie below 2.5 eV and even for halogen atoms χ_{ad} does not exceed 3.7 eV. Thus, direct electron transfer from the diamond into an atmospheric adsorbate appears to be impossible. However, a thin water layer, as it forms naturally on all surfaces exposed to atmosphere, provides an electron system which can act as a surface acceptor for diamond. Electrons exchange from diamond to the water layer is governed by the redox reaction:

$$2H_3O^+ + 2e^- \rightleftharpoons H_2 + 2H_2O. \tag{2.9}$$

The reaction is driven by the difference in the chemical potential of electrons in the liquid phase (μ_e) and in diamond (Fermi level, E_F). Since μ_e is below E_F, electrons are being transferred from diamond to the water layer and the reaction is left to right (2.9). The compensating holes in the diamond form the accumulation layer and the associated space charge induces a potential (surface bad bending) taht raises μ_e. At the equilibrium μ_e and E_F are equal at the interface as shown schematically in fig. 2.11. The equilibrium value of μ_e relative to the vacuum level as the common reference for the aqueous layer and the solid depends, according to Nernst's equation, on the H_2 partial pressure (pH_2) and on the pH value of the aqueous layer as:

$$\mu_e = -4.44\,eV + \frac{0.058}{2}\,eV\left[2pH + log\left(\frac{pH_2}{bar}\right)\right]. \tag{2.10}$$

Supposing a concentration of dissolved hydrogen at the interface between diamond and the thin water layer in the ppm range, which should correspond to a partial pressure of $pH_2 \approx 10^{-3}$ mbar, the chemical potential μ_e of an aqueous wetting layer is -4.26 eV. Taking the electron affinity of -1.3 eV for hydrogenated diamond, the position of E_F at the water/diamond interface lies about 50 meV below VBM (see fig. 2.12): the VBM of all semiconductors, including hydrogen-free diamond, lies more than 0.7 eV below μ_0. Standard atmospheric conditions will therefore never produce hole accumulation within those materials. Only the strong reduction of the electron affinity by hydrogen termination does the VBM of diamond shift up above the chemical potential of typical surface wetting leyers. The hole charge is then compensated by those anions (HCO_3^-) that are left uncompensated by the reduction of the oxonium ions. This explains the surface conductivity of hydrogenated diamond. Once surface conductivity has been established, the sample can even be put into vacuum and the wetting layer be removed. As long as the anions remain at the surface the hole accumulation will also be preserved. Thermal desorption of the anions which takes place at much lower temperatures ($\approx$ 300 °C) than those necessary for surface dehydrogenation in UHV $\approx$ 700 °C removes the accumulation layer and leaves a hydrogenated but highly resistive surface.

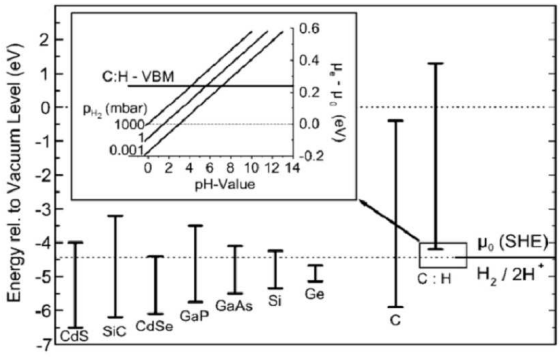

Figure 2.12: Energies of the band edges of several semiconductors and of hydrogenated and hydrogen-free diamond relative to the vacuum level [68].

Chapter 3

Principles and experimental set up of surface analysis thecnique

In this chapter the physical principle behind the analytical techniques together with the correspondent experimental apparatus used for the diamond characterization will be illustrated. In the first part will be described in detal the surface sensitive techniques such as X-ray photoelectron spectroscopy (XPS) and Ultra light Photoelectron spectroscopy (UPS). In the second part a brief description of the other surface analysis thecnique used in this work as contact angle, sheet resistance and Atomic Force Microscopy (AFM).

3.1 XPS and UPS surface analysis techniques

Considering the tight bond between chemistry and electronic structure which dictate the behavior of the diamond surface, XPS and UPS occupy a prominent position among the analytical techniques.

The photoemission spectroscopy is based on energy of electrons emitted from a solid, liquid or gas when a electromagnetic radiation impact the sample. In the case of XPS the photon source generates X-rays while in UPS UV photons are used as excitation radiation. Since photons do not carry any electric charge, they can easily penetrate in the matter. Accordingly to the dielectric constant of the material and the wavelength of the exciting radiation, the electromagnetic waves interact more or less easily with the dielectric environment being partially or totally absorbed or transmitted. X-rays can penetrate in depth in the materials (typical penetration depth $\approx \mu$m) and along their path, any photon can easily generate highly energetic photoelectrons. Differently from photons, photoelectrons emitted in the bulk strongly interact with the surrounding matrix which causes intense scattering. Only a fraction of the photoelectrons are able to reach the sample surface and exit in the

vacuum. This fraction is dependent on the initial energy of the photoelectron which determinates the number of possible collisions i.e. energy losses. Only those electrons reaching the sample surface with an energy higher than ϕ (sample forw function)) may exit in the vacuum. Apart the unavoidable decrease in signal intensity there is a positive effect on photoelectron spectra. In fact, scattered electrons which still retain a residual amount of energy sufficient to escape from the sample, carry information relative to the nature of the network causing the energy losses. The photon energy then defines the sampling depth λ which is the maximum depth at which one photoelectrons can be generated and, after scattering, emitted from the surface. λ depends on the material density i.e. scattering probability. Practically it varies from 1 - 2 nm in the case of high density materials as in the case of diamond, to 6 - 8 nm in the case of soft materials like polymers. This explains why the X-ray or UV photoelectron spectroscopies (XPS) are surface sensitive techniques. Also, XPS and UPS are a non-destructive technique which is suitable to obtain information about the composition and the chemical bonds formed. This technique is then very helpful to study the surface functionalizations induced by wet chemical processes, plasmas o radiation induced graftings. In principle with XPS is possible to analyze all the materials which can be brought under ultra high vacuum (UHV). So a wide class of materials ranging from metals, metal alloys, glasses or ceramic materials, polymers and biomaterials, thin organic/inorganic films may be analyzed.

3.1.1 Photoelectron spectroscopy

The photoemission process is based on the photoelectric effect (see fig. 3.1).

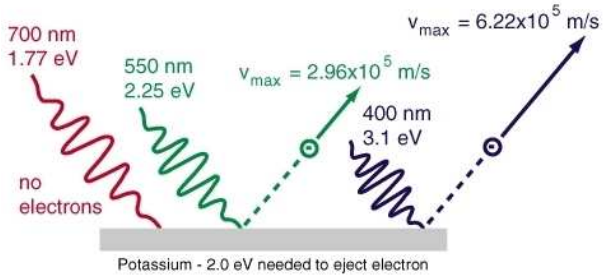

Figure 3.1: Scheme of Photoelectric Effect.

If the energy of the exciting radiation is higher than the energy required to excite an electron above the vacuum level, that electron will be *photoemitted* in the vacuum with a kinetic energy equal to:

$$E_{k,max} = h\nu - E_B - e\phi_c, \tag{3.1}$$

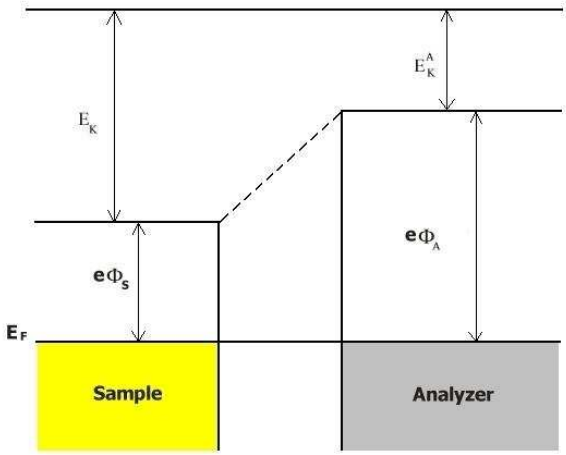

Figure 3.2: Sample and analyzer energy levels.

where E_k is the electron kinetic energy (which is the measure quantity), hν is the incident photon energy and E_B is the binding energy and ϕ_c is the sample work function.

Let us consider the equation 3.1. In principle it should be necessary to know the sample work function to be able to establish the photoelectron binding energy (since the photon energy is known and the kinetic energy is measured). However, as the kinetic energies are estimated by the analyzer, which has its own work function ϕ_A, referred to a conductive sample in electrical connection with the instrument chassis (i.e. the analyzer itself), photoelectrons have to overcome a potential barrier given by $\Delta\phi = \phi_A - \phi_S$ (fig. 3.2). So the kinetic energies, measured by the spectrometer, becomes:

$$\begin{aligned} E_k^S &= E_k - e\Delta\phi \\ &= h\nu - E_B - e\phi_S - e(\phi_A - \phi_S) \\ &= h\nu - E_B - e\phi_A. \end{aligned} \tag{3.2}$$

As we can see, the only work function involved in the equation is the spectrometer work function ϕ_A. For any kind of conducting materials the chemical potential (Fermi level) equalizes with that of the instrument which, being grounded, corresponds to zero. In the case of non conducting materials the binding energy scale is aligned respect to reference peaks (normally C1s from graphite). This allows measure exactly the kinetic energy of photoelectrons coming from eny kind of material.

3.1.2 Photoemission process

Several models have been proposed to treat the photoemission process theoretically. A phenomenological description that splits the process into three steps as called *three step model* has been developed by Berglund and Spicer [79, 80]. In this approach, optical excitation between two Bloch states, transport of the electron to the surface, and escape of the electron through the surface into the vacuum are treated separately. In more recent models, photoemission is described as a one step process (one step model) [81]: the electron is excited from the Bloch initial state into a state that is composed of a free propagating part outside the crystal and a damped part inside the crystal, the damping taking account of the limited mean free path of the photoelectrons (see fig. 3.3).

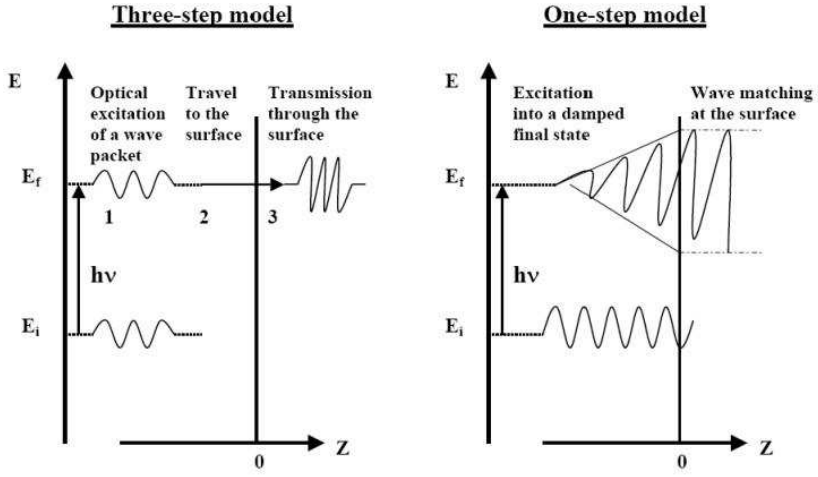

Figure 3.3: Illustration of the three-step and one-step models.

In principle, during the photoemission process, the solid behaves as a multibody system, which interacts with incident radiation as a whole; however a good simplification is to neglect the interaction between the photoelectron and N-1 electrons that do not take part in the process, with N the number of all the electrons in the solid. With this assumption the number of electrons emitted from an atom with momentum (p, p+dp), along Ω direction, within an angle dΩ, in the time unit, depending on the *Fermi golden rule* [82], is:

$$d\nu = (2\pi\hbar^2)^{-2} \, |M_{if}|^2 \, \delta(E_k - E_{nl} - h\nu) \, p^2 \, dp \, d\Omega; \tag{3.3}$$

where hν is the incident photon energy, E_k is the photoelectron kinetic energy, E_{nl} the ionization energy of the involved energy level and $|M_{if}|^2$ is the matrix element

given by:

$$M_{if} = \int \psi_f \, \hat{H} \, \psi_i \, d\vec{r}; \tag{3.4}$$

in which $\hat{H} = (\frac{e}{m}) \, \vec{A} \cdot \vec{p}$ is the Hamiltonian which describes the incident radiation-electron interaction ($\vec{A}$ is the vector potential). The differential photoemission cross section is given by the ratio between dν and the incident photons flow F = $\omega^2 \, \frac{A}{8\pi\hbar c}$:

$$d\sigma_{ph} = \frac{d\nu}{F} = \left(\frac{\alpha}{\pi^2}\right)\left(\frac{v}{\nu}\right)|m_{if}|^2 \, d\Omega, \tag{3.5}$$

where v is the photoelectron speed, α is the fine structure constant and $|m_{if}|^2$ is the reduced matrix element:

$$m_{if} = \int \psi_f \nabla \psi_i \, d\vec{r}. \tag{3.6}$$

If we suppose that the final state is represented by the wave function $\psi_f \sim e^{i\vec{k}\cdot\vec{r}}$ and that the initial state is given by (*Thomas-Fermi theory* [83], [84]):

$$\psi_i \sim (\pi a_{nl}^3)^{-\frac{1}{2}} e^{\left(-\frac{r}{a_{nl}}\right)}, \tag{3.7}$$

where a_{nl} is the shell and nl radius, we can write the reduced matrix element as $16\pi a_{nl}/(k a_{nl})^6$. Replacing in the equation 3.5 we finally obtain the *photoemission cross section*:

$$\sigma_{ph} = 2^7 \pi \, \alpha \, a_0^2 \left(\frac{a_0}{a_{nl}}\right)^{-5} \left[\frac{I_0^{\frac{7}{2}}}{h\nu (h\nu - E_{nl})^{\frac{5}{2}}}\right] \quad \text{with} \quad (h\nu >> E_{nl}), \tag{3.8}$$

where $I_0 = e^2/a_0 = 27.2$ eV (in the CGS system). As it can be observed from equation 3.8 the photoemission cross section is a function of the photon energy and it decreases when the energy increases. Now we can calculate the probability that one electron is excited at the energy state E_f which is x by the surface, by a photon of energy hν:

$$\xi(E_k, h\nu) dE dx = \sigma_{ph} * (1 - R(h\nu)) * e^{-\alpha(h\nu)x} dE dx, \tag{3.9}$$

where R is the optical reflectivity at the surface and α is the optical assorbance coefficient.

3.1.3 Migration of the electron toward the surface

After the photoemission process, photoelectrons pass through the solid and travel toward the surface; during this phase they are scattered by crystal lattice electrons

and ions. For high kinetic energies the prevailing process is the electron-electron interaction, while for lower kinetic energies electron-phonon interaction overbear.

Electron *Inelastic Mean Free Path* (IMFP), λ, defined as the average distance traveled between two inelastic interaction, is shown in figure 3.4 for different materials. Is important to notice the dependence of λ on the energy. This dependence imply that electrons which exit from the sample surface originate from atoms which are located near the surface [85]. We can notice that this trend is pretty similar for different

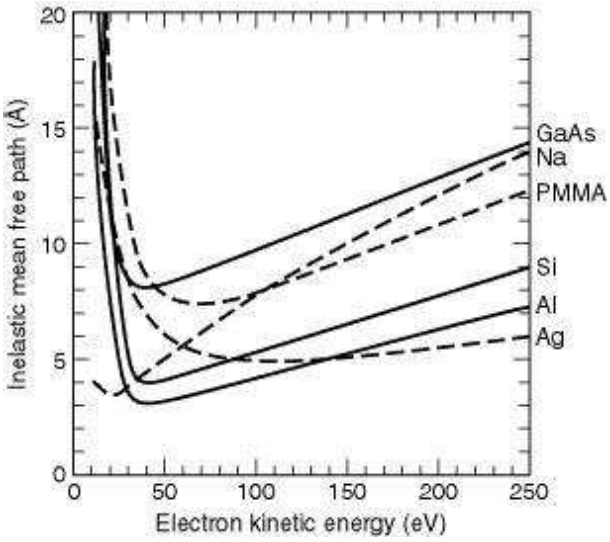

Figure 3.4: Inelastic Mean Free Path in Ag, Al, GaAs, Na, PMMA and Si.

materials: it decreases until 10 - 15 eV, reaches a minimum and then increases monotonically over 100 eV.

From experimental data analysis, Tanuma et al. [86] have derived this expression for λ [87]:

$$\lambda(E_k) = \frac{E_k}{E_p^2[\beta \ln(\gamma E_k) - (C/E_k) - (D/E_k^2)]}, \tag{3.10}$$

where E_p is the fundamental plasmon energy, β, γ, C and D are experimental parameters, which are considered constant in the range 50 - 2000 eV.

In the *weak* X-rays region (100 - 1000) eV, λ can be approximated with a universal formula, valid for each material [88]:

$$\lambda(E_k) = \frac{a}{E} + b\sqrt{E_k} \quad \text{Å}, \tag{3.11}$$

with a = 2170 and b = 0.365 for inorganic compounds.

In a XPS measurement the energy range is typically (100 - 1500) eV; in such an interval λ assumes values in the range (10 - 50) Å. Thus only electrons generated within a distance equals to λ from the surface are able to escape from the solid without loosing all their kinetic energy; for this reason XPS can be regarded as a *superficial technique*. If the electron are detected perpendicular to the sample surface, the inelastic mean free path λ corresponds to the escape depth. It is commonly assumed that the sampling depth corresponds to 3 $\lambda \sin(\theta)$. This simple relation clarify why decreasing the take-off angle θ the sampling depth reduces and the surface sensitivity od the analysis increasea. Let us consider again the process of photoemission illustrated in fig. 3.1. The probability that an electron, generated at a depth x, leaving the surface perpendicularly without inelastic interactions is simply given by:

$$P(E_k) = e^{-\frac{x}{\lambda(E_k)}}. \tag{3.12}$$

Let us now consider the more general situation in which also losses are present. In this case the probability of a photoelectron to be excited at the energy E_f, overcome the surface potential, reach the vacuum level and escape is given by the product of the three probabilities:

$$Q(E_k, h\nu, x) = \xi(E_f, h\nu)\, dE\, dx \ * \ P(E_k)B(E_k). \tag{3.13}$$

$B(E_k)$ represents the probability of an electron to overcome the surface potential generated by the discontinuity of the material network which ends at the surface. Then this value is zero if the electron kinetic energy is lower than the surface potential. N($E_k, h\nu$) represents the photoelectron distribution as a function of their kinetic and excitation energy as it that can be observed experimentally. N($E_k, h\nu$) is formed by two contributions. The first is exactly Q($E_k, h\nu$)dE descring photoemission without any energy loss. The second contribution, *scattering interactions* [S($E_k, h\nu$)dE], derives from scattered photoelectrons. So the total distribution is given by:

$$N(E_k, h\nu)\, dE = Q(E_k, h\nu)\, dE + S(E_k, h\nu)\, dE. \tag{3.14}$$

The spectral contribution of Q(E_k,hν) and S(E_k,hν) can be easily recognized. In photoelectron spectra Q(E_k,hν)dE is described by very narrow structures called core lines. Differently, S($E_k, h\nu$) describes the back ground and, on the proximity of the low energy side of the core lines, the spectral features originated by plasmon, shake-up and shake-off processes as it will be described in more detailed in the next section.

3.2 The X-ray photoelectron spectrum

An XPS spectrum represents the number of emitted photoelectrons depending on their energy (Kinetic or Binding). It is made up by *primary* and *secondary* structures which arise from a *background*.

Elastic photoemission, in which a photoelectron is ejected from an atom in the solid and escape from the surface without suffering energy loss, gives rise to discrete peaks whose energies obey equation 3.1 which reflects the shell structure of the atomic electrons. Thus, at binding energy (BE) close to zero, the closely-spaced valence band levels, labelled 5d, appear and with increasing BE the increasingly tightly-bound core levels (5p, 4f, 4d, 4p, 4s, 3d, 3p, 3s). Finally, the decay of core holes resulting from photoemission can give rise to Auger electron emission and the appearance of Auger peaks (series). The peaks sit on a background which rises with BE the background is dominated by the electrons resulting from inelastic scattering. The background is seen to have a step-like character, with increases on the low KE side of each peak, due to electrons which have suffered some energy loss during their escape.

3.2.1 Core levels

Photoelectric peaks are thin lines which represent electrons emitted from core levels that haven't inelastic interactions. Binding energy possessed by these levels is characteristic for each chemical element and it is registered in appropriate database; thus it is possible to identify each element, which has emitted a particular electron (see eq. 3.2).

Peaks width ΔE, defined as the full-width-at-half maximum (FWHM), is due to different reasons: the intrinsic energy level width ΔE_i excitation source width ΔE_x and other extrinsic factors, such as analyser energy resolution ΔE_a. To a first approximation, assuming that the components are all of Gaussian form, these can be convoluted such that:

$$\Delta E = \sqrt{(\Delta E_i)^2 + (\Delta E_x)^2 + (\Delta E_a)^2}. \tag{3.15}$$

The nomenclature for core levels is nl_j where n is the principal quantum number, l is the orbital angular momentum quantum number and j is the total angular momentum quantum number, j = (l + s) where s is the spin angular momentum quantum number $\left(\pm\frac{1}{2}\right)$. Thus s levels (l = 0) are singlets but all other levels (l > 0) give rise to doublets. The two possible states are different in energy because the unpaired electron left in an orbital following photoionisation can have its spin and orbital angular momentum vectors either parallel or anti-parallel. This is known as *spin-orbit (j-j) coupling*. The difference in energy between the doublet components, ΔE_j, is proportional to the spin-orbit coupling constant ξ_{nl} which depends on the expectation value $\left\langle \frac{l}{r^3} \right\rangle$ of the orbital involved, r being the average radius. The separation, which can be many electron volts, therefore increase with atomic number z for a given subshell (constant n, l) and decease as l increases for constant n. Doublet

Table 3.1: Energy levels and doublets areas ratio.

Livel	Values of j	Area ratio
s	1/2	-
p	1/2 , 3/2	1:2
d	3/2 , 5/2	2:3
f	5/2 , 7/2	3:4

relative intensities are given by:

$$\frac{I_{l+1/2}}{I_{l-1/2}} = \frac{l+1}{l}. \tag{3.16}$$

Rations between doublets intensities are given in table (3.1).

Another important aspect of XPS analysis is the possibility to discern, not only the elemental composition of a sample surface, but also its chemical bonds. Photoelectric peaks, related to the same element, but corresponding to different *non-equivalent atoms* that means they are surrounded by dissimilar chemical or crystallographical enviroment show different binding energies: this charge is called *chemical shift*, in analogy with the terminology used in Nuclear Magnetic Resonance (NMR). Evaluating this shift it is possible to go back to the chemical bonds involved and their chemical species. Just to show an example of the chemical shift magnitude, in table 3.2 are shown the most common chemical shifts affecting the carbon core line in presence of different bonds [89]:

A simplified model to explain the chemical shift is the *charge-potential model* [90], which states that the ionization energy E_i of a particular level in an atom depends on

Table 3.2: C1s *chemical shift* for the most common chemical bonds.

Group	Description	Binding Energy (eV)
-CH	Aliphatic	285.0
-C-C=O	Carbon β	285.2
-C-O-C	Ether	286.4
-C-O-H	Alcohol	286.5
-C=O	Carbonyl	287.9
O=C-N	Amide	288.2
$-CF_2-CF_2-$	PTFE	293.0 ∴ 294.0

the potential generated by the atom valence band electrons and on the surrounding atoms electrons:

$$E_i = E_i^0 + kq_i + \sum \frac{q_i}{r_{ij}} \quad with\ i \neq j; \tag{3.17}$$

where E_i^0 is the reference binding energy witout chemical shift, kq_i is the valence band electrons contribution to the shift, k takes into account valence and core levels electrons interaction and q_i is the valence electrons charge and the last term is the the potential generated by all the surrounding atoms.

If we consider the atom as a sphere with surface charge kq_i (deriving from its valence electrons), the potential inside the sphere is given by $\frac{q_i}{r_v}$ where r_v represents average valence orbitals radius. A charge variation equals to Δq_i induces a potential variation $\Delta \frac{q_i}{r_v}$ inside the sphere, which reflects also upon deep levels binding energy; in particular an increasing in valence electrons number $\Delta q_i < 0$ causes a decreasing of the binding energies. Otherwise if r_v increases for a fixed q_i then $\frac{\Delta q_i}{r_v}$ decreases. For example, considering the orbital 2p of titanium in its neutral metallic state, the peak maximum will be located at 454.2 eV, while for TiO_2 (oxidation number +4) its binding energy will be at 458.7 eV.

Quantitative analysis

Another important feature of XPS analysis technique is the possibility not only to identify chemical elements but also to perform quantitative analysis, to obtain the composition and information about the stoichiometric ratios among elements . The intensity of a given peak is directly proportional to the abundance of those atoms in the sampled volume. After background subtraction it is then possible to estimate the atomic concentration starting from the relative peak intensities.

The intrinsic photoelectron spectrum $I^{'}(E)$ is given by difference between the measured spectrum I(E) and the background B(E):

$$I^{'}(E) = I(E)B(E),\ \forall E. \tag{3.18}$$

There are many ways to evaluate B(E) and then $I^{'}(E)$ which are reported below:

- constant background;
- linear background;
- Shirley background;
- Tougaard background.

The simplest possibility for background correction is the subtraction of a constant (*constant background*) from the measured spectrum using B(E) = const minor of I(E).

Linear background is an another easy way and it is determined by a line connecting two points P and Q located on the high- and low- KE sides of the analyzed peak. Even if it is a very simple method, it introduces some errors in the peak intensity evaluation due to the arbitrary choice of P and Q.

An alternative method is the one introduced by Shirley [91], in which it is assumed that B(E_k), for a given kinetic energy, it is proportional to the peak area, integrated between E_k and infinite:

$$B(E_k) = k \int_{E_k}^{\infty} I(E^{'})dE^{'}. \tag{3.19}$$

Generally, for each photoelectron peak, two integration terminal points are chosen E_{min} and E_{Max}:

$$B(E_k) = k \int_{E_k}^{E_{Max}} I(E^{'})dE^{'}, \tag{3.20}$$

where it is assumed that $I^{'}(E^{Max}) = I^{'}(E^{min}) = 0$, we obtain k:

$$k = I(E_{min}) \diagup \int_{E_{min}}^{E_{Max}} I(E^{'})dE^{'}. \tag{3.21}$$

Shirley method describes quite well step trend due to electrons inelastic losses, even if it does not base on a physical model.

The last method here presented is *Tougaard model*, which has originally been developed as an alternative to the Shirley background for transition metals and is therefore especially suited for asymmetrical signals like metal 4f lines. In this model $I^{'}(E)$ is given by [92]:

$$I^{'}(E) = I(E) - \lambda(E) \int_{E}^{\infty} K(E|E^{'} - E)I(E)dE^{'}, \tag{3.22}$$

where λ represents the electron mean free path inside the solid while $K(E|E^{'} - E)$ is the probability, for an electron of energy E to loose an energy quantity equals to $(E^{'} - E)$ due to inelastic scattering in an path length = 1. $K(E|E^{'} - E)$ function can be obtained theoretically or experimentally for example via REELS (Reflactive Electron Energy Loss Spectrum) measurements. Performing different measurements on policrystalline sample like Au, Ag and Cu, Tougaard proposed the following relation [93]:

$$\lambda K(E^{'} - E) = \frac{B(E^{'} - E)}{[C + (E^{'} - E)^2]^2}; \tag{3.23}$$

where B = 2866 eV^2 and C = 1643 eV.

The choice of the correct background depends on the kind of sample analyzed After background subtraction is possible to calculate the elemental concentration.

XPS signal intensity, measured for a fixed E_k at a deph z from the surface, depends firstly on incident photons intensity I_o, on spectrometer efficiency D(E_k) and on photoionization cross section $\sigma_{ph}(h\nu)$ [88]:

$$I(E_{k,z}) = I_0\sigma_{ph}(h\nu)D(E_k)Nexp[-z/\lambda(E_k)cos(\theta)]T(E_k)L(\gamma), \tag{3.24}$$

where L(γ) represents angular asymmetry of photoemission intensity from each atom, T(E_k) is the analyzer transmission factor and θ is the angle formed by photoelectrons escape direction and the normal to the sample . For a homogeneous solid, integrating over all sample thickness, we have:

$$I(E_k) = \int_0^\infty I(E_{k,z})dz = I_0N\sigma_{ph}(h\nu, E_B)D(E_k)L(\gamma)\lambda(E_k)\cos(\theta)T(E_k), \tag{3.25}$$

Equation 3.25 is defined with these approximations:

- homogeneous and flat sample;
- the sample is amorphous which means that electrons do not suffer diffraction phenomena;
- unimportant elastic scattering influence.

The ratio between I_A/I_B, two peaks intensities, with kinetic energies E_A and E_B is:

$$\frac{I_A}{I_B} = \frac{N_A\sigma_A\lambda(E_A)T(E_A)}{N_B\sigma_B\lambda(E_B)T(E_B)}, \tag{3.26}$$

where we supposed that detector efficiency is constant. Remembering that, for kinetic energy ion the range (100 - 1500) eV, $\lambda(E_k) \sim \sqrt{E_k}$ (see equation 3.11) and that from experimentals relations $T(E_k) \sim \frac{1}{\sqrt{E_k}}$, we obtain:

$$\frac{I_A}{I_B} = \frac{N_A\sigma_A}{N_B\sigma_B} \implies \frac{N_A}{N_B} = \frac{I_A/\sigma_A}{I_B/\sigma_B}. \tag{3.27}$$

In other words, the ratio between atomic concentrations is equals to ratio between intensities weighted for their cross sections. If the sample is an alloy made by N elements, it is possible to evaluate each concentration, c_i, just using the following relation:

$$c_i = \frac{I_i/\sigma_i}{\sum_j^N I_j/\sigma_j}, \tag{3.28}$$

with the condition that the overall sum is equals to unity:

$$\sum_j^N c_j = 1. \tag{3.29}$$

The equation 3.28 rapresents the simple case of a homogeneous solid, or at least homogeneous within the sampling depht.

3.2.2 Auger peaks

The *Auger effect* (fig. 3.5) is a phenomenon in which the emission of an electron from an atom causes the emission of a second electron. When an electron is removed from a core level leaving a vacancy, an electron from a higher energy level may falls into the vacancy releasing a certain amount of energy. Although sometimes this energy is emitted in the form of a photon, the energy can also be transferred to another electron, which is ejected from the atom. This second ejected electron is called an *Auger electron* (from the French physicist Pierre-Victor Auger, who described this process in 1925).

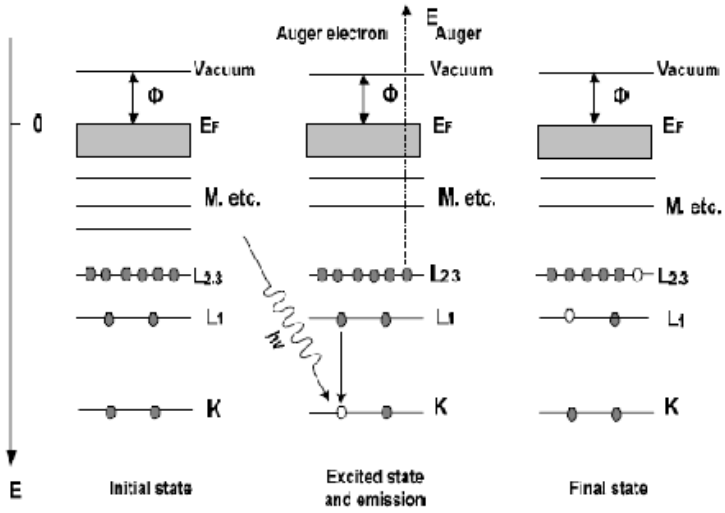

Figure 3.5: An example of an Auger process.

Let us suppose that an incident x-ray generates a vacancy in the K level, which will be later occupied by an electron from level L_1. This transition will create a photon with energy $E_K - E_{L_1}$. Let us suppose also that this photon will be adsorbed by a third electron in the L_2 level which will be emitted with kinetic energy:

$$E_K - E_{L_1} - E^*_{L_2}, \tag{3.30}$$

As it can be seen, E_K does not depend from x-ray excitation energy.

An Auger transition is always described using three letters, which refer to the energy levels involved during the process. Thus, if X-rays ionize a K level, which is filled by a L_1 electron, and the photon produced in this transition ionize a M_2 level, then the whole Auger transition will be named KL_1M_2 .

Auger transitions are also visible in a XPS spectrum with less intense features. As observed, the kinetic energy (KE) of an Auger electron is independent, in contrast

to the photoelectrons, on the exciting radiation. If, for example, the X-ray source is changed from Mg K α (1253.6 eV) to Al K α (1486.6 eV) all photoelectron peaks increase in KE by 233 eV while the Auger peaks remain unchanged. If the spectrum is plotted in Binding Energy (BE), the reverse is true. This allows one to easily distinguish between the two kind of peaks. The three main Auger series are KLL, LMM and MNN.

3.2.3 Valence band

Valence levels are those occupied by electrons with low binding energy (say 0 - 15 eV) which are involved in delocalized or bonding orbitals. The spectrum in such a region consists of many closely spaced levels, which give rise to a *band* structure. Hence, this region is usually referred to as the valence band.

Cross-sections for photoelectron emission from valence levels are much lower than for core levels, giving rise to low intensities in general. However valence band spectra relate closely to the occupied density of states structure. This is very useful in the study of both electronic and chemical properties of materials, although theoretical calculations are required to fully exploit their potential.

3.2.4 Secondary structure

Apart from primary peaks, we can find other *secondary structures*, with lower intensities, in a XPS spectrum. They are summarized as follow:

- satellites peak;
- ghost peaks;
- plasmons and phonons.

X-ray satellites. The X-ray emission spectrum from a non-monochromatic source exhibits not only the characteristic X-ray emission but also some minor X-ray components. For each photoelectron peak that results from the routinely used Mg and Al Kα x-ray photons, there is a family of minor peak at lower energies, with intensity and spacing characteristic of the X-ray anode material. In table 3.3 are listed principle secondary lines for Al and Mg X-ray sources.

When a X-radiation from an element other than the X-ray source anode impinges the sample, resulting in small peaks corresponding to the most intense spectral peaks but displaced by a characteristic energy interval there is the formation of *x-ray ghost lines.*

These lines may result from impurities present in the anode, oxidation of the anode, or generation of X-ray photons in the Al foil X-ray window. Occasionally, such lines can originate via generation of X-ray within the sample itself. This last

Table 3.3: X-ray satellites of Mg K$\alpha_{1,2}$ and Al K$\alpha_{1,2}$ and relative positions of the O kα and Cu kα ghosts on the kinetic energy scale [94].

Relative Intensity		
Line X	Mg	Al
K α_1	0 (100.0)	0 (100.0)
K $\alpha^{'}$	4.5 (1.0)	5.6 (1.0)
K α_3	8.4 (9.2)	9.6 (7.8)
K α_4	10.0 (5.1)	11.5 (3.3)
K α_5	17.3 (0.8)	19.8 (0.4)
K α_6	20.5 (0.5)	23.4 (0.3)
K β	48.0 (2.0)	70.0 (2.0)
O K α	-728.7	-961.7
Cu K α	-323.9	-556.9

possibility is rare because the probability of X-ray emission is low relative to Auger electron emission. Because such ghost lines rarely appear with non-monochromatic X-ray sources (they cannot be generated with monochromatic sources) problems related to line identification can be reasonably excluded.

Electron exiting the material can lose part of their energy in exciting collective oscillation of conduction electrons.

These oscillation have frequencies characteristic of the particular material analyzed and are quantized. An electron which spent part of his energy for the excitation of these collective oscillation is said to have suffered a *plasmon loss*.

Within the solid the loss is said to be of a *bulk plasmon*, and if the frequency of the bulk plasmon is ω_b, then the plasmon energy loss is clearly hω_b. The value of frequency ω_b depends on the material physical properties as shown by the following simple relation:

$$\omega_b^2 = \frac{ne^2}{m\varepsilon_0}, \tag{3.31}$$

where n is the material atomic density, m electron mass and ε_0 is the vacuum dielectric constant.

At a surface the atomic lattice of the solid terminates and the conditions allowing bulk plasmon excitation are no longer satisfied. Instead, a rather localized type of collective oscillation can be excited at a frequency ω_s, which is less than ω_b:

$$\omega_s = \frac{\omega_b}{\sqrt{2}}. \tag{3.32}$$

These features are of most importance for clean metal surfaces bat they are present, with a minor contribution, also in isulating sample as diamond.

3.3 The UPS photoelectron spectrum

Ultraviolet photoelectron spectroscopy is a technique complementary to XPS . It involves application of the photoelectric effect to the study of electronic structures of the materials because the energy of ultraviolet light (HeI = 21.22 eV and HeII = 42.2 eV) is sufficient to only eject electrons from the valence orbitals.

As in XPS, the spectrum is obtained by scanning the range of kinetic energies and plotting the number of electrons exhibiting a given kinetic energy (or binding energy using the relation $E_B = h\nu$ - E_k), that is, *counts per unit time* versus kinetic energy. Spectra are normally displayed with the ordinate labeled as *count rate* or simply *relative intensity*. The latter designation is sufficient because the absolute count rate is a facet of any complex experimental variables, usually varying from one instrument to another, and is essential meaningless for any given sample; however, the relative intensities are meaningful. Relative intensities of spectral bands are related to the relative probabilities of photoionization to different states of the molecular ion, that is, the relative differential photoionization cross sections.

With the analysis of the spectrum HeI and HeII, is possible to have direct information about the position of the Fermi level (E_F) of the material, to evaluate the work function of the material and also the electron affinity in the case of semiconductors [95]. Direct measurements of diamond work function in ultrahigh vacuum (UHV) using the inelastic secondary electron peak is possible. The figure 3.6 illustrates the relation between the width of the spectrum (W), the sample work function ϕ and the photon energy hν. The spectral window is determined by the distance between the inelastic cut-off and the valence band maximum (VBM).

HeI and HeII radiation may be used in a combined way. In HeI-UPS the secondary electron peak appears as a sharp feature whose position determines the minimum detectable kinetic energy of electrons leaving the diamond surface into the vacuum. A linear extrapolation on the low kinetic side of this peak allows to evaluate the *cut off* as shown in fig. 3.6 a. The cross section of the σ orbitals is higher for all the atoms when using the HeII excitation respect to HeI. The VBM is then calculated by the linear extrapolation of the onset of emission (see fig. 3.6 b) on a HeII spectrum.

Once W is estimated from HeI and HeII spectra, knowing the energy gap (E_g) of the material, the electron affinity can be simply calculated as:

$$\chi = h\nu - E_g - W; \tag{3.33}$$

where hν is the photon energy.

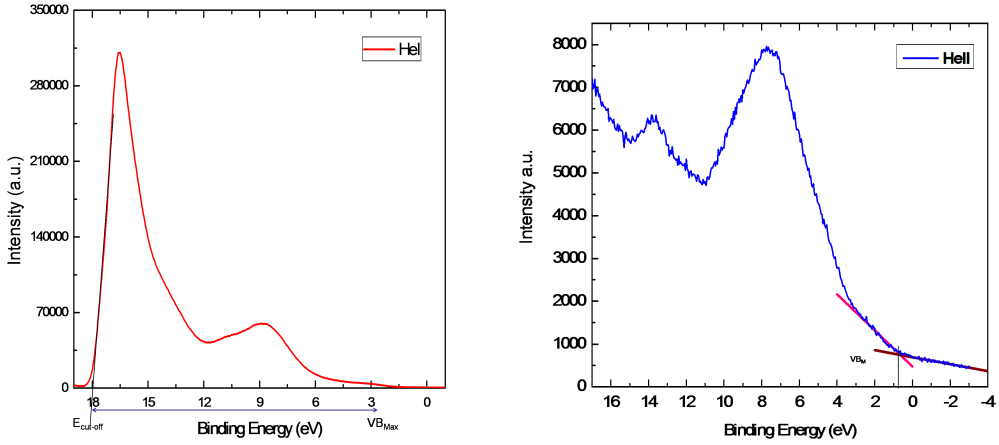

(a) (b)

Figure 3.6: (a) Shows a typical HeI UPS spectrum of diamond. The relation between spectrum width, hν and work function ϕ is illustrated. (b) Shows a typical heII UPS spectrum od diamond and the linear extrpolation for the detection of valence band maximum.

3.4 XPS and UPS experimental apparatus

This section is devoted to the description of the instrument XPS/UPS system which was used for the characterization of the diamond samples.

The main components of an XPS or UPS system include:

- an excitation source (X-rays or UV photons);
- an ultra-high vacuum (UHV) stainless steel chamber with UHV pumps;
- sample introduction chamber;
- an electron energy analyzer;
- an electron detector system (with a channeltron, electron multiplier);
- a readout system connected to a pc with a proper acquisition software.

An irradiated specimen with X-ray or UV photons, ejects photoelectrons and a portion of these are collected by a lens system which lead them into an energy analyser. Electrons selected by the analyser are then collected and registered by an electron detector. The source, specimen, lens, analyser and detector are mounted in an ultra-high vacuum (UHV) chamber. Electronics include the necessary power

supplies and the control and logic circuitry needed for the spectrometer and the data acquisition. The user interface is usually implemented on a computer. The output is in the form of an electron energy spectrum or a map (or image) of the distribution of chemical elements from analyzed area of the sample surface.

All the commercial XPS or UPS systems have a chamber in which the analysis is carried out. This is linked to a sample introduction system consisting of a simple chamber equipped with an introduction system such as a magnetic coupled transfer arm. Sometimes, as in our case, the system possess also aa sample treatment chamber in which sample cleaning, thermal treatments, scraping, sample fracture, etc. may be performed. Again proper means are provided to transfer samples from chamber to chamber.

Vacuum requirements for XPS and UPS

Ultra high vacuum (UHV) conditions are required to perform XPS or UPS. There are several reasons for this:

- in XPS instruments the X-ray sources commonly operate with tungsten filaments which require a good vacuum;
- the major source of contamination comes from the gas molecules which may be present in the vacuum chamber. Cleanliness during analysis may be ensured only in UHV conditions;
- XPS and UPS are surface sensitive analysis techniques requiring an atomically clean surface. This may be created with *in-vacuum* fracture or ion sputtering.

Most manufactures of current XPS and UPS instrumentation use similar pumping systems. The analysis chamber is most commonly pumped with an ion or turbomolecular pumps, and is isolated from the specimen insertion chamber with a gate valve. Also the preparation chambers are equipped with same pumps and separated from the other chambers with gate valves. If the system has to be opened to atmospheric pressure for repairs, it is evacuated through the specimen insertion system. The specimen preparation chamber is most commonly pumped from atmospheric pressure to about 1 Pa using direct-drive rotary vane mechanical oil less pumps, such as a diaphragm or molecular drag pump. These are used as backing pumps for turbo molecular pumps (TMP), which evacuate this region to pressure (10^{-6} Pa) where a sputter ion pump (SIP) will start (10^{-5} Pa). Titanium sublimation pumps (TSP) and non evaporable getter (NEG) pumps are also used in analytical chambers to improve the vacuum.

Specimen cleaning

Heating is one way to clean a specimen because contaminations are desorbed. Unfortunately it cannot be used for any kind of sample because it cal alter the surface composition and it also specimens outgassing may occur. The preparation chamber of the PHI 545/590 instrument is equipped with a heating system to clean and anneal the sample in UHV before the UPS or XPS analysis This system allows to heat the sample until a temperature of 1000 ℃ and to perform *in situ* the XPS or UPS.

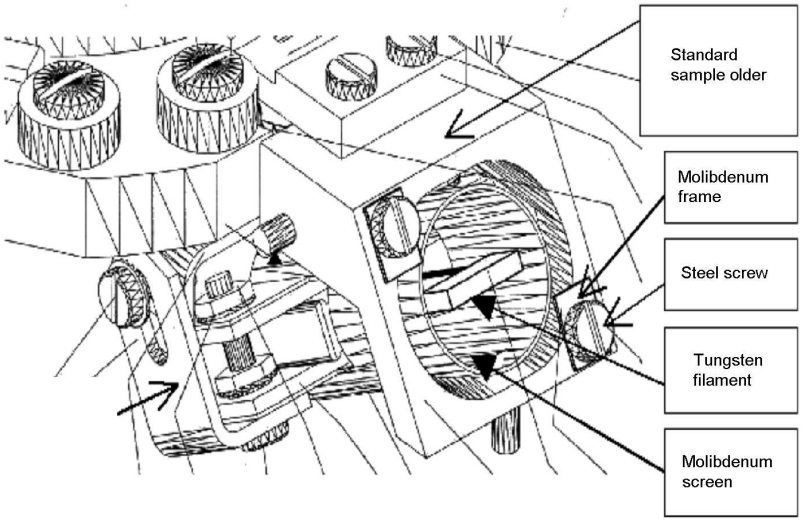

Figure 3.7: Eating system presents in the preparative chamber of the instrument PHI 545/590.

3.4.1 The X-ray source

All the laboratory XPS instruments use the same method of producing X-rays: the bombardment of a metallic target with high-energy electrons. A small portion of the bombarding electrons cause vacancies in inner electron shells of the target atoms. Electrons from higher levels *fall* down to fill the vacancies with the simultaneous emission of X-ray photons.

Two types of X-ray source are generally utilized. The targets used to generate the X-radiation are made of Al or Mg. These materials (as thin films deposited onto water-cooled copper targets) are bombarded with electrons up to 15 KeV in energy. The X-ray output consists of a continuous energy distribution extending up to the incident electron energy (Bremsstrahlung), with a much higher intensity at the characteristic Kα energy. This line, actually an unresolved doublet ($\alpha_{1,2}$), results

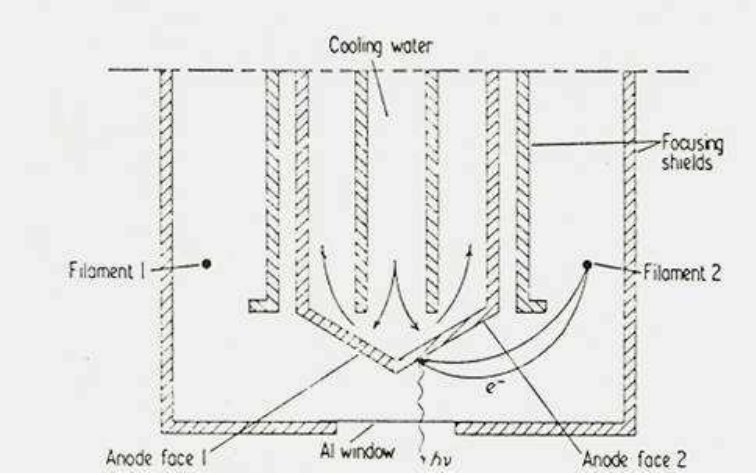

Figure 3.8: Scheme of dual anode source.

from the transitions $2p_{\frac{3}{2}} \rightarrow 1s$ and $2p_{\frac{1}{2}} \rightarrow 1s$ in the ionized target atoms. Weaker satellite lines also result from valence band $\rightarrow$ 1s ($\alpha\beta$) transitions and transitions involving multiply-charged atoms (for example, $K\alpha_3$, K α_4). All these photons excite peaks in the photoelectron spectrum according to equation 3.1. The characteristic energies and widths of the principal lines are 1253.6 (0.70) eV for Mg Kα and 1486.6 (0.85) eV for Al kα. The relative intensities and separations of the satellites are given in table 3.3.

Old or damaged targets may also produce Cu Kα from the exposed copper base and/or O Kα from heavy target (anode) oxidation. The peaks which these X-ray excite are related to as ghost peaks and their relative energy positions are also given in table 3.3.

Al and Mg targets are usually included in a single dual-anode source (fig. 3.8) for easy switching between photon source. Two filaments are provided to excite the respective targets. The aluminum/magnesium combination is chosen because both lines gives relatively intense photoelectron spectra and both have relatively narrow characteristic Kα lines. The use of a dual anode allows one to electrically switch X-ray source, thereby changing the position of Auger peaks in an XPS spectrum.

In order to increase the XPS instrument energy resolution, the X-ray source is monochromated using a single anode source with an aluminum target, combined with a focussing monochromator composed by a single or multiple quartz crystals. In this case a small focused spot (down to 10 μm diameter) can be produced at the sample surface with an intense photon flux. The monochromators may reduce the FWHM of the (Al Kα) radiation down to $\sim$ 0.26 eV Moreover all satellite lines and Bremsstralung radiation are removed, producing a cleaner spectrum with re-

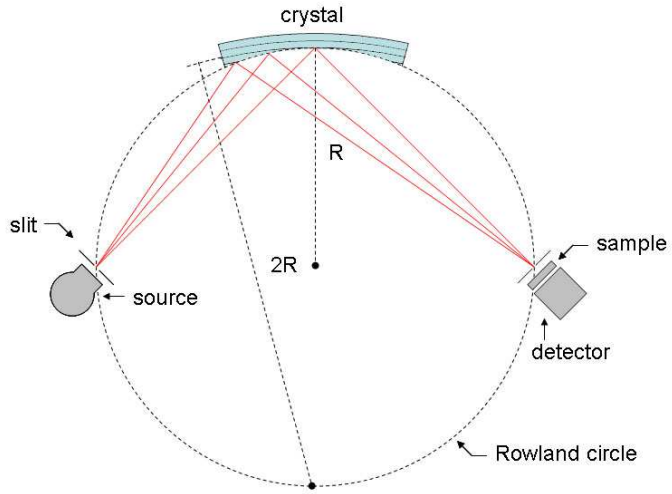

Figure 3.9: Scheme monochromator.

duced background intensity, particularly in the low binding energy (BE) region. The monochromator is shown schematically in figure 3.9. The selection of the X-wavelengths is based upon the Bragg diffraction of Al Kα X-radiation by the $(10\bar{1}0)$ planes of quartz. The diffracting crystal is set on a Rowland circle of radius R with the crystal bent to a radius 2R in the dispersive direction (Johann geometry) and to $2Rsin^2\theta$ in the non-dispersive direction. In this configuration the Bragg angle is high [$\theta = 78.5$ ° for Al Kα on quartz $(10\bar{1}0)$] thus allowing the Johann geometry without any serious geometric aberrations. The line width can be determined from the dispersion of the monochromator:

$$\frac{\Delta E}{\Delta x} = \frac{E}{2Rtan\theta}; \tag{3.34}$$

this means that for a source spot size of 1 mm diameter the energy spread will be 0.61 eV.

The X-ray source, typically, operates at an accelerating voltage of 15 kV, with the target grounded and and the filament kept at high voltage. This configuration prevents backscattered electrons damaging or penetrating the source window. The window, a thin, metallic, X-ray transparent foil is designed to prevent any stray source electrons from entering the analysis region. The electron beam current can be as high as 30 mA, so that at 15 kV electron beam energy, 450 W of power has to be dissipated almost all in the form of heat. The heat removed by cooling water deionize to avoid anode incrustations.

3.4.2 UV source

The incident radiation used in UPS spectroscopy must be monochromatic so that monoenergetic electrons can be ejected from a given level. Photon source that inherently produce monochromatic radiation are the most efficient and most intense ionizing sources. For this purpose resonance lamps has proven to be the best. The most common source for ionizing low energy electrons has been the intense resonance lines of the rare gases produced by discharges or microwaves. Resonance radiation can be produced by, microwaves, or direct-current discharge through a rare gas confined in a 1 to 2 nm diameter capillary. These lamps require high voltages and currents (5 kV, 150 mA) and need frequent cleaning and electrode change. The discharge between the anode and cathode takes place through the capillary in the center of the quartz tube and is viewed through a fiber optic pipe. Since the discharge takes place in the capillary, a high flux is generated. Photons pass to the analysis chamber through a second coaxially aligned collimating capillary tube. A pumping port is provided in the intermediate region between the two capillaries for removing the rare gas. This differential pumping of the lamp is necessary to prevent selfabsorption and to keep the analysis chamber in UHV because to have high UV intensities no quartz window are used. The radiation produced by a resonance lamp is usually very narrow and no monochromatization is needed Helium is the most commonly used gas, which, with its most probable transition $1s^1 2p^1 \rightarrow 1s^2$, gives origin to two different energy lines: 21.2 eV (HeI) and 40.8 eV (HeII) if the atom is singly ionized.

3.4.3 Energy analysers

All commercial XPS instruments use electrostatic analysers. There are the electrostatic hemispherical analyzer (HSA) or the double-pass cylindrical mirror analyzer (DPCMA).

The HSA analyzer, that is shown in figure 3.10, is made by two concentric hemispherical plates characterized by two different radius: R_1 and R_2 and two different voltage V_1 and V_2. In the middle is electrons trajectory with the radius R_0 and characterized by E_0 energy. The electron entering the hemispherical analyser are repelled by V_2 (negative with respect to V_0), are attracted by V_1 (positive with respect to V_0) and travel along, or near to, mean radius R_0 to refocus at the exit slit. The negative voltages V_2 and V_1 are related to R_0, R_1, and R_2 by the equations:

$$V_1 = V_0 \left(3 - 2\frac{R_0}{R_1}\right), \tag{3.35}$$

$$V_2 = V_0 \left(3 - 2\frac{R_0}{R_2}\right). \tag{3.36}$$

In the middle the voltage is:

$$V_0 = \frac{V_1 R_1 + V_2 R_2}{2R_0}. \tag{3.37}$$

Only the electrons with energy E = e V_0 and that tangentially enter passing by the entrance slit in the HSA analyser describe the radius R_0 and will be focused at the exit slit above the detector. The energy E_0 is known as the pass energy. Even though the electrons are monoenergetic, the focus is not perfect and the electrons are characterized by ΔE:

$$\Delta E = \frac{E_0 \left(W_1 R_1 + W_2 R_2\right)}{2R_0} + (\delta\alpha)^2 ; \tag{3.38}$$

Where$(\delta\alpha)^2$ is the difference between the ideal tangent trajectory and the real tangent trajectory,W_1 and W_2 the the entry and the exit slit-widths respectively.

Differently, the CMA consists of two concentric metal cylinders arranged in a way that their axes are coincident. A negative potential is applied to the outer cylinder, while the inner one is connected to ground. Electrons, which escape from sample surface, enter the analyzer and are reflected from the electric field applied toward the inner cylinder, with a trajectory depending an their kinetic energy. Hence only electrons in a narrow energy region (called pass energy E_0) succeed in travelling along the cylinders to the detector:

$$E_0 = \frac{Ke}{ln\frac{b}{a}} U; \tag{3.39}$$

where K is a geometrical constant depending on the analyzer, a and b are the inner and the outer cylinders radii, U is the cylinder applied potential and e is the elementary charge. The energy resolution is improved by apertures within the analyzer:

$$\frac{\Delta E}{E} = 2.75 \left(\delta\alpha\right)^3 ; \tag{3.40}$$

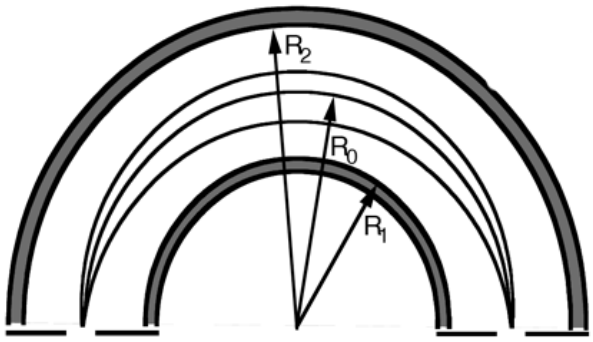

Figure 3.10: Scheme of HSA analyser.

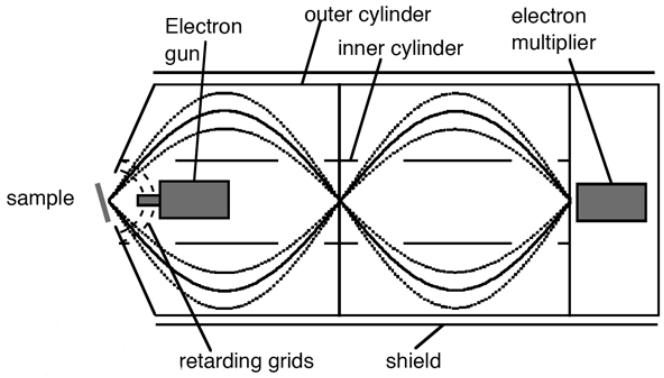

Figure 3.11: Scheme of CMA analyser.

where $\delta\alpha$ is the angolar dispersion. Differently from the CHA, this analyser is particularly sensitive to the sample position. The sample must be positioned at the correct focal distance using selected by a moving it in and out. Despite this the CMA has the advantage of a far higher solid angle of acceptance, which can be up to 100 times greater than that of a CHA. Although, this increase is achieved at the expense of the ability to detect angle resolved features. The concentric cylinder design also means that an electron gun can be accomodated within the central cylinder (fig. 3.11) to provide an excitation source for Auger Electron Spectroscopy (AES). The current collected at analyzer and, opportunely amplified by using a channeltron, is given by:

$$I \propto EN(E) \tag{3.41}$$

where N(E) is the electrons energy distribution.

3.4.4 Flood gun

Photoemission from an insulating material leads to the generation of a positive charge unless this can be dissipated in some way. Non-monochromated X-ray souces produce a broad, diverging X-ray beam which illuminates the sample holder and other parts of the analysis chamber, generating low-energy electrons. Bremsstrahlung excited low-energy electrons also emerge from the front face of the aluminum window, separating the X-ray source from the analysis chamber, which is close to the sample. A sufficient flux of these low-energy electrons are attracted to the sample surface by a positive potential of few eV generated instantaneously when the X-ray source is switched on leading to surface *neutralization* This fortuitous situation does not apply with a monochromaticed X-ray source, which produces a focused beam illuminating only part of the sample. Any electron flux is eliminated as well as the Bremsstrahlung radiation. An external source of low-energy electrons, the electron *flood gun*, is

therefore, required to perform the sample neutralization. The introduction of highly-focused X-ray sources led to more severe differential charging problems.

The *flood gun* is based on a filament which thermo-emitts electrons at a well controlled energy.

3.4.5 Fondazione Bruno Kessler facilities

During my PhD time I have the possibility to work with two different surface analysis setups both located at the *Fondazione Bruno Kessler* (Trento, Italy): a SCIENTA ESCA 200 model and PHI 545-590 multiple analytical system (XPS, UPS, AES).

The SCIENTA ESCA 200 (see fig. 3.12) operating since 1995, which has an hemispherical analyzer with a radius of 200 mm. The x-ray source is a monochromatic Al kα radiation with a spatial resolution of 10 μm. To carry out charge compensation on insulating samples, the instrument is equipped with a food gun and to perform in depth profile analysis it it is equipped with Ar ion gun (up to 5 keV accelerating voltage) for sputtering. The energy resolution of the instrument is 0.3 eV (measured on the Ag Fermi edge with a pass energy of 75 eV) and a sensibility of 0.5 - 1 % at. conc.. A completely automatized 5 axis manipulator allows sequential analyses on different samples. In addition, the possibility to redice the take-off angle by tilting the sample allows to increase the surface sensitivity of the analysis.

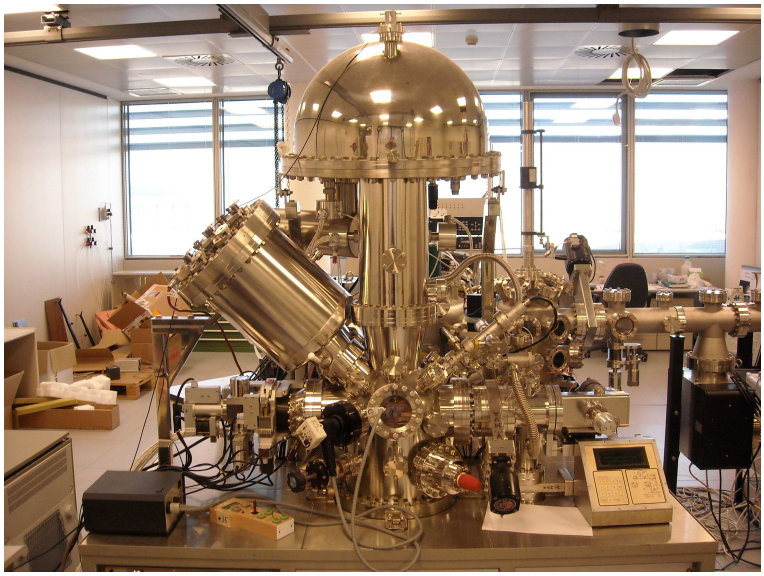

Figure 3.12: SCIENTA ESCA 200 located at PAM-SE laboratory of Fondazione Bruno Kessler.

The PHI 454-590 3.13 is a very interesting instrument because its analysis cham-

ber is equipped with a x-ray source (non-monochromatic), two electron gun and a UV source. It possible to perform XPS, UPS and Auger spectroscopy. It is equipped with a single- and a double-pass cylindrical analyzer which is used to get a higher energy resolution. Typical energy resolutions are ~ 0.9 eV for XPS and ~ 0.6 eV for UPS. This instrument gives the possibility to perform *in situ* analyses because it is equipped with a preparation chamber in which thermal treatments can be performed under UHV.

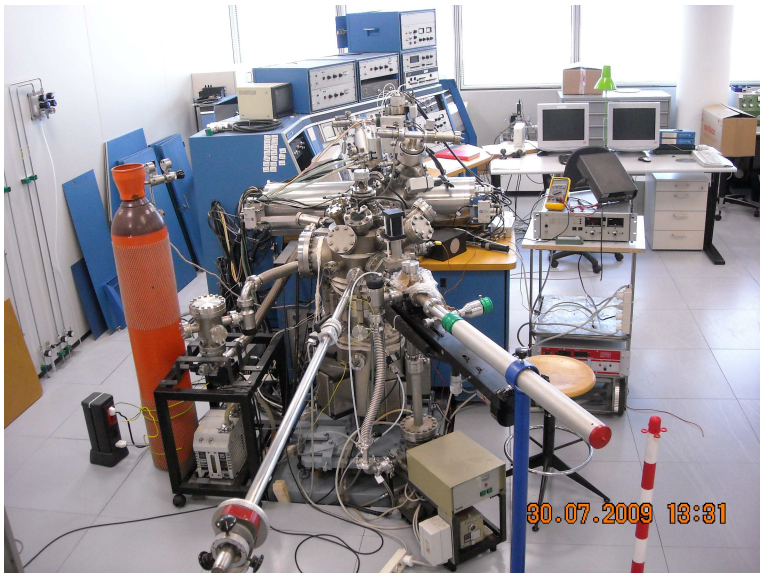

Figure 3.13: PHI 545-590 located at PAM-SE laboratory of Fondazione Bruno Kessler.

3.5 Static Contact Angle

The wettability reflects the thermodynamic properties of a surface and is measured through the *contact angle*. The contact angle of a fluid on a solid is the degree of interaction between the solid and fluid itself and depends on the chemical composition and the topography of the surface. Most often the concept is illustrated with a small liquid droplet in equilibrium on a flat horizontal solid surface (Static Contact Angle). The shape of the droplet is determined by the *Young-Laplace equation*, which describes the pressure difference over a meniscus between two fluids:

$$\Delta p = \gamma \left(\frac{1}{R_1} + \frac{1}{R_2} \right) = 2\gamma H; \tag{3.42}$$

where Δp is the pressure difference over the interface, γ the surface tension, H is the mean curvature, and R_1 and R_2 are the principal radii of curvature at the interface. For a spherical meniscus of radius R, the equation simplifies to:

$$\Delta p = \gamma \frac{2}{R}. \tag{3.43}$$

The *sessile drop method* is used to estimate properties of a localized region on a solid surface. The angle between the baseline of the drop and the tangent at the drop boundary is measured using a goniometer. This technique is ideal for non flat samples or where one side of the sample has different properties The theoretical description of contact arises from the consideration of a thermodynamic equilibrium between the three phases: the liquid phase of the droplet (L), the solid phase of the substrate (S), and the gas/vapor phase of the ambient (V) which will be a mixture of ambient atmosphere and an equilibrium concentration of the liquid vapor) (fig). The V phase could also be another (immiscible) liquid phase.

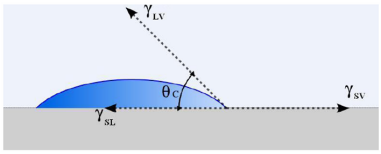

Figure 3.14: Contact angle scheme.

At equilibrium, the chemical potential in the three phases should be equal. It is convenient to discuss the problem in terms of the interfacial energies. We denote the solid-vapor interfacial energy as γ_{SV}, the solid-liquid interfacial energy as γ_{SL} and the liquid-vapor energy (i.e. the surface tension) as simply γ; we can write an equation that must be satisfied at the equilibrium (known as the *Young Equation*):

$$\gamma_{SV} - \gamma_{SL} - \gamma \cos\theta = 0 \tag{3.44}$$

where θ is the *experimental* contact angle. Thus the contact angle can be used to determine an interfacial energy (if other interfacial energies are known). This equation can be rewritten as the *Young-Dupré* equation:

$$\Delta W_{SLV} = \gamma \left(1 + \cos\theta\right) \tag{3.45}$$

where ΔW_{SLV} is the adhesion energy per unit area of the solid and liquid surfaces when in the medium V.

The wetting angle is an informative characteristic of the structure and physico-chemical state of the materials (roughness, disturbance, presence of impurities in the near-surface layer, and chemical nature of surface functional groups [96].

Contact angle measurements were performed on diamond films using an *home made* contact angle instrument (see fig. 3.15). It consists in a web came in a micrometric manipulating system where the sample is placed. Illumination of the sample is very important to obtain high quality drop images. The illumination system is obtained with white leds and a light diffusing shield. All the datas were analysed using the free software *ImageJ*.

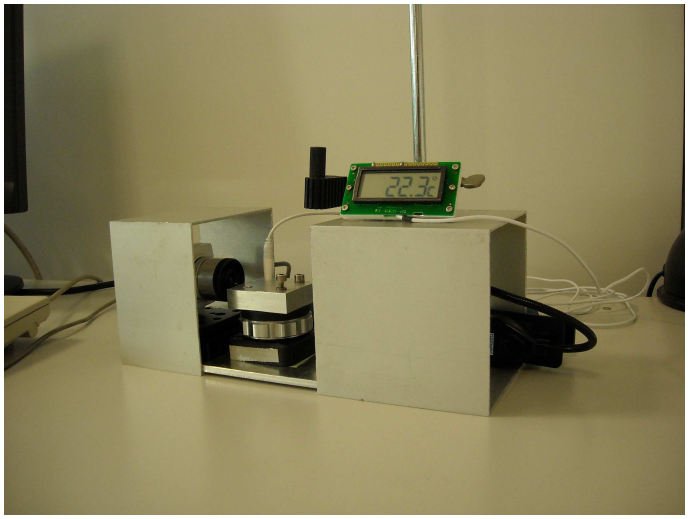

Figure 3.15: Contact angle apparatus located at PAM-SE laboratory of Fondazione Bruno Kessler.

3.6 Analytical microscopy

Scanning-probe microscopy refers to a class of techniques in which a very fine needle probe is mechanically moved across the surface of a sample in a series of straight lines (scans). The interaction of the probe with the surface is recorded as a function of position on the surface, hence the nature of the surface is determined in a very direct manner.

Since we are dealing with microscopies, direct images are produced, although only very small surface area on the sample are probed. Many different types of surface probes exist corresponding to different modes of operation.

3.7 Atomic Force Microscope AFM

One of the most important microscopy is the Atomic Force Microscope (AFM). In an AFM apparatus, the probe is mounted on the free end of a very sensitive mechanical cantilever. As the probe is scanned across the sample, the force existing between the atoms at the tip and those of the sample surface causes deflection of the cantilever, which is typically detected by deviations of a laser beam which is reflected by the oscillating cantilever.

In practice, a feedback loop is used to move the cantilever/probe up and down (in a contact, non-contact or tapping mode) so that a constant force (deflection) is maintained. The cantilever deflection required is recorded as a function of surface coordinate. This way, one can ensure that only small cantilever oscillations occur, which keeps the theoretical calculation of forces accurate. In addition, this prevents damage to the surface which could arise from the large forces of a greatly strained cantilever. As will be seen, one advantage that AFM has over other scanning-probe microscopies is that both electrically conducting and non-conducting surfaces can be investigated [97].

In the *Fondazione Bruno Kessler* laboratory there is an AFM SOLVER P47 model which was used to characterize NCD diamond films for photonic applications.

Chapter 4

Bulk characterization techniques

In this chapter, techniques used to characterize material *bulk* properties are illustrated.

4.1 Raman Scattering

Fascination with the marvelous blue of the Mediterranian sea [98] caused C. V. Raman to investigate and explain how the scattering of light by liquids changes with the change of the frequency [99]. As a result he obtained the Nobel Prize in 1930 "for his work on the scattering of light and for the discovery of the effect named after him" [100]. An independent prediction of this phenomenon was made few years earlier by Smekal using classical quantum theory [101]. In the same period other distinguished scientists as Kramers and Heisenberg (1925),Schrodinger (1926) and Dirac (1927) studied this phenomenon.

Only with the availability of laser sources in 1960's, Raman scattering became a standard spectroscopic technique. Indeed, with these new and more intense photon sources the sensitivity to the weak Raman signal was improved and, moreover, the possibility to tune the excitation wavelength allowed to perform experiments in the most suitable conditions.

Raman Theory

Detailed theoretical explanation of Raman effect can be found elsewhere [102–104]. In the following only fundamental equation will be then presented, in particular those which will be useful to the understanding of experimental results. When monochromatic radiation of frequency ω_0 is incident on systems, some scattering of the radiation occurs. If the frequency content of the scattered radiation is analyzed, it will be observed that not only the frequency ω_0 associated with the incident radiation is

present but, in general, pairs of new frequencies of the type $\omega_0 \pm \omega_s$ appears. The frequencies ω_s are found to lie principally in the range of associated with transitions between vibrational and electronic levels. Furthermore the scattered radiation usually has a characteristic polarization different from that of the incident radiation Moreover it depends on the direction of observation. The scattering without change of frequency is called Rayleigh scattering and that with change Raman scattering. Raman bands at frequencies less than the incident one $(\omega_0 - \omega_s)$ are referred to as Stokes bands and those at frequencies greater than incident one $(\omega_0 + \omega_s)$ as anti-Stokes bands. Then, the final effect of the Raman scattering is a transition between the vibrational levels V of the electronic ground state of the molecule with Stokes part representing V=1 $\rightarrow$ V=0 transition (absorption of a photon) and anti-Stokes one representing V=0 $\rightarrow$ V=1 transition (emission of a photon). The intensity of Raman bands is linked to the probability of transition between two state which is dependent on the population of initial state and the availability of final states which, in turns, has the temperature dependence

$$\frac{\mathrm{I}_{Stokes}}{\mathrm{I}_{anti-Stokes}} \propto e^{-\hbar\omega/K_B T}. \tag{4.1}$$

Several approaches exist to describe the Raman scattering, differing in the physical basis adopted. In the classical approach radiation is treated as an electromagnetic wave and the material as an assembly of independent classical oscillators. A second approach in quantum mechanics still maintain a classical treatment of the radiation but treats materials from a quantistic point of view. Another method is to quantize both the radiation and the material system, which belong to the quantum electrodynamics theory.

In the following it will be presented some basic concept derived from the quantum mechanic approach, being the one that satisfactorily represent the phenomena without the complexity of a full quantized theory. In this hybrid approach the electric and magnetic fields associated with the incident electromagnetic radiation are regarded as perturbations of the initial state of the material. Perturbative methods are used to describe the properties of the perturbed system.

The quantum-mechanical description of the Raman effect, using the time-dependent perturbation formalism, allows to obtain, for a given normal mode Q_i, a more rigorous definition of the final intensity of the Raman scattered photons. Nevertheless, the relationships between unperturbed time-dependent wavefunction of the initial and final states $\psi_i^{(0)}$ and $\psi_f^{(0)}$ and the perturbed time-dependent ones $\psi_i^{(1)}$ and $\psi_f^{(1)}$ are derived under some assumption: (i) the perturbation is of the first order, (ii) the interaction Hamiltonian for the perturbation is entirely electric dipole in nature, (iii) the perturbation is produced by the time-dependent electric field associated with a plane monochromatic electromagnetic wave of frequency ω_0.

In quantum-mechanics any direct transition between two energy levels is accompanied by emission or absorption of electromagnetic waves, if the dipole moment of the transition is non-zero, i.e.

$$\mathbf{p^{(1)}}_{fi} = \left\langle \psi_f^{(1)} \left| \hat{\mathbf{p}} \right| \psi_i^{(0)} \right\rangle + \left\langle \psi_f^{(0)} \left| \hat{\mathbf{p}} \right| \psi_i^{(1)} \right\rangle \neq 0; \tag{4.2}$$

where $\hat{\mathbf{p}}$ is the induced dipole moment operator. For a scattering process from an electromagnetic wave the dipole moment of the transition become

$$\mathbf{p}_{fi} = (\left\langle \psi_f^{(1)} \left| \hat{\alpha} \right| \psi_i^{(0)} \right\rangle + \left\langle \psi_f^{(0)} \left| \hat{\alpha} \right| \psi_i^{(1)} \right\rangle)\mathbf{E}; \tag{4.3}$$

with $\hat{\alpha}$ the transition polarizability operator, which is linked to the polarizability tensor representing the ability of the electronic cloud of a system to be deformed by the electric field of the interacting photons. It is possible to obtain a rigorous representation of Raman effect starting from the Raman scattering tensor $[\alpha_{\rho\sigma}]_{fi}$, which components are obtained accordingly to the Kramers-Heisenberg expression

$$[\alpha_{\rho\sigma}]_{fi} = \frac{1}{\hbar} \sum_{r \div i,f} \frac{\langle \psi_f \left| \hat{p}_\rho \right| r \rangle \langle r \left| \hat{p}_\sigma \right| \psi_i \rangle}{\omega_{ri} - \omega_0 - i\Gamma_r} + \frac{\langle \psi_f \left| \hat{p}_\rho \right| r \rangle \langle r \left| \hat{p}_\sigma \right| \psi_i \rangle}{\omega_{ri} + \omega_0 + i\Gamma_r}. \tag{4.4}$$

where $|r\rangle$ are the wavefunctions describing the virtual states and Γ_r represent their respective half-width. The broadening of the state is related to its finite lifetime, being a non-equilibrium state, through the uncertainty principle $\tau = 1/2\Gamma_r(\omega)$. Instead initial and final state are assumed to have infinite lifetimes, an approximation valid in the time scale of Raman process.

If none of transition frequencies coincides with an electronic excitation and then $\hbar\omega_0 < E_e - E_g$ the resulting Raman signal associated to a given normal mode is weak. This phenomenon is consequence of the transition probability between two state; being a virtual state a non stationary state in nature, the transition to this state is not favored. On the contrary excited electronic level and the use of an exciting laser with a frequency which falls in an optical transition of the system lead to resonant Raman scattering characterized by intense spectra.

If the ω_0 match (or is very close to) the frequency for an electronic transition of the molecule (Resonance Raman condition), then the Kramers-Heisenberg expression assume the simplified form

$$[\alpha_{\rho\sigma}]_{fi} = \frac{1}{\hbar} \sum_{r \div i,f} \frac{\langle \psi_f \left| \hat{p}_\rho \right| r \rangle \langle r \left| \hat{p}_\sigma \right| \psi_i \rangle}{\omega_{ri} - \omega_0 - i\Gamma_r}; \tag{4.5}$$

where only terms having as denominator $(\omega_{ri} - \omega_0 - i\Gamma_r)$ become dominant. It is important to notice that, in the Resonance Raman condition, $[\alpha_{\rho\sigma}]_{fi}$ should become greater than in conventional Raman condition due to the smallness of the denominator. In this conditions the intensity of the associated normal mode should be

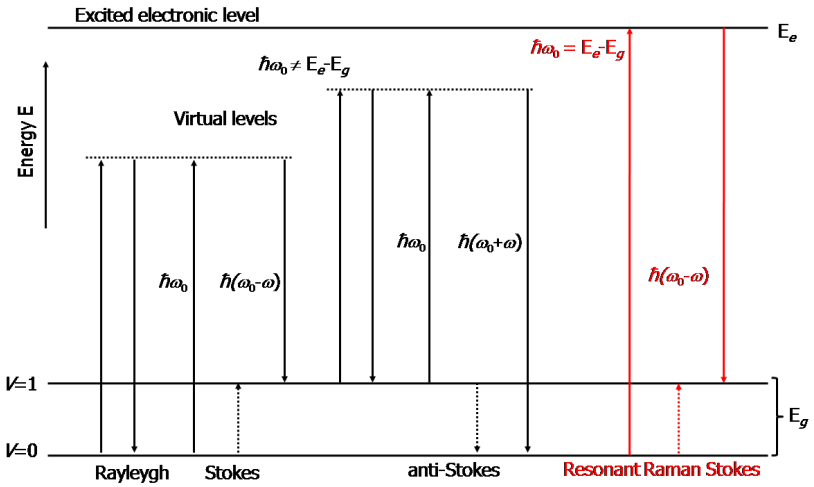

Figure 4.1: Schematics of the non resonant Stokes and anti-Stokes transitions and of a resonant one.

enhanced. In order to have $[\alpha_{\rho\sigma}]_{fi} \neq 0$ for a given normal mode the numerator has to be non-zero also.

4.2 Scanning Electron Microscope - SEM

The Scanning Electron Microscope (SEM) uses a focused beam of high-energy electrons to produce high-resolution three dimensional images of the surface structure of the sample. The signals that derive from electron-sample interactions reveal information about the sample including external morphology (texture), chemical composition, and crystalline structure and orientation of materials making up the sample.

In a typical SEM electrons which are thermionically emitted from a tungsten cathode or emitted via field emission (FE), are accelerated toward an anode. The electron beam, which typically has an energy ranging from a few hundred eV to 100 keV, is focused by one or two condenser lenses into a beam with a very fine focal spot sized 1 nm to 5 nm. The beam passes through pairs of scanning coils in the objective lens, which deflect the beam horizontally and vertically so that it scans in a raster fashion over a rectangular area of the sample surface. When the primary electron beam interacts with the sample, the electrons lose energy by repeated scattering and absorption within a teardrop-shaped volume of the specimen known as the interaction volume, which extends from less than 100 nm to around 5 nm into the surface. The size of the interaction volume depends on the beam accelerating voltage, the atomic

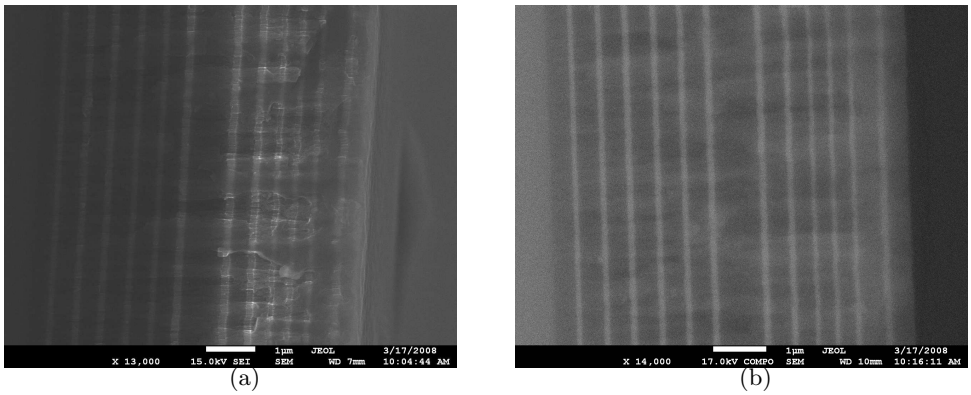

(a) (b)

Figure 4.2: SEM immagines: (a) photonic crystall SEM immagine acquired by secondary electrons; (b) photonic crystall SEM immagine acquired by backscattered electrons.

number of the specimen and the specimen density. The energy exchange between the electron beam and the sample results in the emission of electrons and electromagnetic radiation which can be detected to produce an image, as described below.

The most common imaging mode monitors low energy (50 eV) *secondary electrons*. Due to their low energy, these electrons originate within a few nanometers from the surface. The electrons are detected by a scintillator-photomultiplier device and the resulting signal is rendered into a two-dimensional intensity distribution that can be viewed and saved as a Digital image.

Another imaging mode consists in detecting *backscattered electrons* (BSE), which take origin in the electron beam, that are reflected or back-scattered out of the specimen interaction volume. Backscattered electrons may be used to detect contrast between areas with different chemical compositions, especially when the average atomic number of the various regions is different, since the brightness of the BSE image tends to increase with the atomic number.

Differences between the two operational modes becomes clear locking at figure 4.2. There, the same sample, a photonic crystal , was analysed both using secondary electrons (fig. 4.2 (a)) and using backscattered electrons (fig. 4.2 (b)). As it can be seen, more clear details appear in the second case. Backscattered images were currently used to evaluate the dimensions of the NCD crystallites, the surface roughness and presence of surface damaging after plasma treatments. Analyzing the samples in the direction of the thickness, an evaluation of the adhesion between diamond film and substrate is also possible.

If the SEM apparatus is provided with an x-ray detector, it is also possible performing *x-ray microanalysis*, identifying x-rays, which are produced by the interaction

of electrons with the sample. Identification of the different chemical element may be obtained allowing compositional analyses.

The SEM instrument used during the PhD work ia a Thermal Field Emission SEM JSM-7001F (see fig. 4.3) that is present in the Physics department of the University of Trento (IDEA Laboratory).

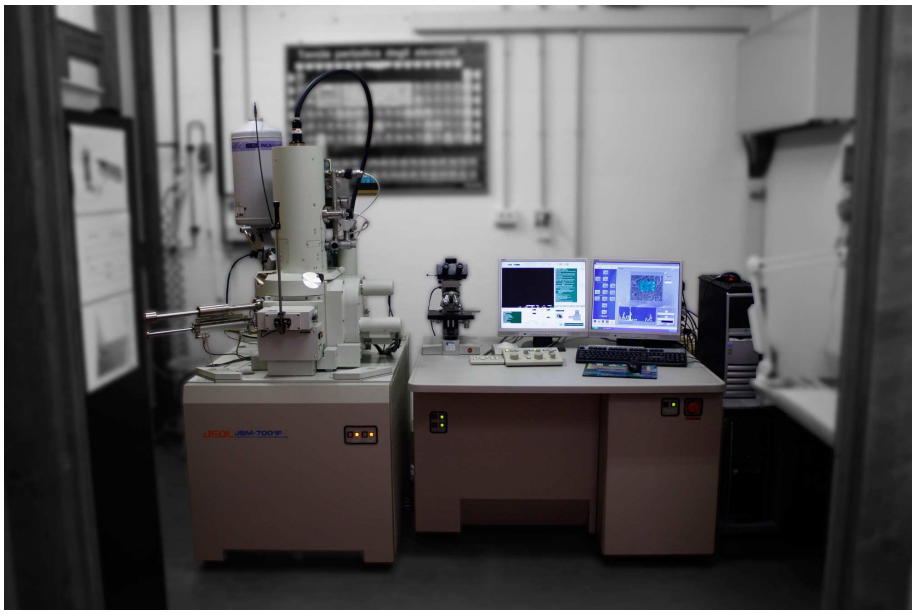

Figure 4.3: SEM instrumentation located at IDEA laboratory of University of Trento.

4.3 Spectrophotometer

The spectrophotometry is the quantifiable study of electromagnetic spectra. It is more specific than the general term electromagnetic spectroscopy in that spectrophotometry deals with visible light, near-ultraviolet, and near-infrared.

A spectrophotometer is a photometer that can measure intensity as a function of the light source wavelength. Important features of spectrophotometers are spectral bandwidth and linear range of absorption measurement.

Absorption measurements on liquid solutions and thin films can be carried out by means of two spectrophotometers. The first one is a UV/VIS spectrophotometer (Perkin-Elmer l15) working in the range (200 - 900) nm. The second one is a UV/VIS/IR spectrophotometer (Perkin-Elmer l19) operating in the range (200 - 3200) nm.

4.4 m-line apparatus

Dealing with thin films the m-line technique allows an accurate measurement of the propagating modes from which the refractive index and the thickness of the film can be determined.

This technique is based on the optical coupling between a high refractive index prism and the film to be characterized [105]. The technique applies the principle of distributed coupling through evanescent fields to the modes of thin-film waveguides.

In this coupler, the prism is placed above the thin-film guide and is separated from it by a small gap of low refractive index (air or oil).

In these conditions, the incident light is totally reflected at the base of the prism. As a result the waves in the prism and in the film are coupled through their evanescent fields in the (air or oil) gap. By proper orientation of the direction of the incident beam, with respect to the prism surface and therefore with the film surface, it is possible to excite any of the film guided modes. In figure 4.4 a schematic representation of the prism-film coupling method is reported.

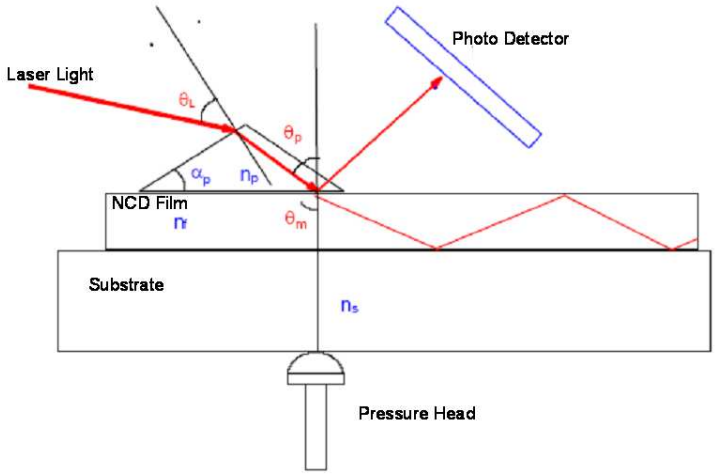

Figure 4.4: Schematic picture of prism film coupling for m-line measurements.

When light is coupled into one of the waveguide modes, because of film inhomogeneities, the optical energy is rapidly scattered into other modes and then coupled back to the outside medium through the other face of the prism (see figure 4.4). Thus the detector, where the light beam is reflected, sees a series of bright lines (called *m-lines*) with a intense spot. Each line represents a mode of different order m while

the bright spot is the beam totally reflected from the base of the prism. When the spot is on the m^{th} bright line, this means that we are exciting the m^{th} mode. Inside the spot a dark line is visible and it represents the energy lost from the excited mode by scattering. The coupling between prism and film takes place when the component of the propagation constant parallel to the film surface is equal for the wave in the prism and the wave in the guiding film. We have coupling when the propagation

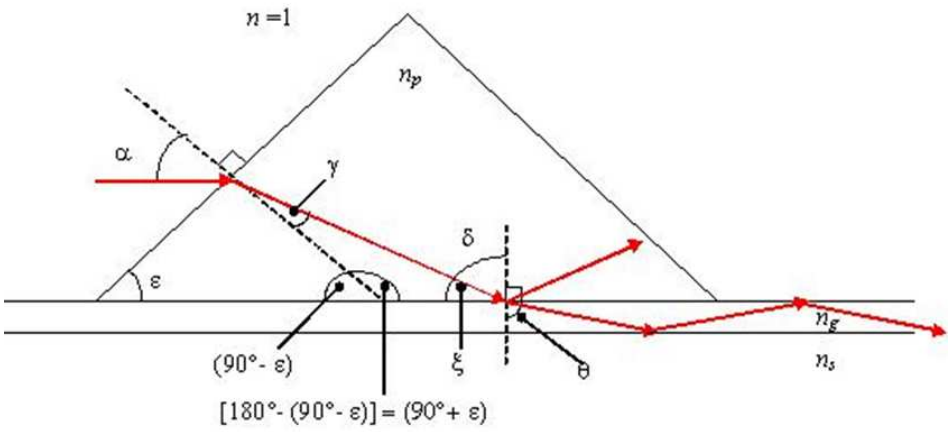

Figure 4.5: Prism-film coupling: relation between propagation angles in ambient, prism and film.

constant in the prism is the same of the propagation constant in the guide (see fig. 4.5):

$$\frac{2\pi}{\lambda} n_a \sin\alpha = \frac{2\pi}{\lambda} n_p \sin\gamma; \tag{4.6}$$

$$\frac{2\pi}{\lambda} n_{prism} \sin\delta = \frac{2\pi}{\lambda} n_{guide} \sin\theta. \tag{4.7}$$

where n_a is the refractive index of air (so it is equal at 1), n_p is the refractive index of the prism and n_{eff} is the refractive index of the excited mode. When there is the total reflection at the interface prism-guide ($\theta = 90$ °) so that a modes in the guide could be excited, the equation 4.6 becomes:

$$\sin\beta = n_p \sin\gamma; \tag{4.8}$$

and the equation4.7 changes in:

$$n_p \sin\delta = n_{eff}. \tag{4.9}$$

The light propagation angle inside the waveguide can be easily related to the angle between the laser beam and the normal to the surface prism. The relation between the angles are:

$$\xi = 180^\circ - (90^\circ + \varepsilon) - \gamma = 90^\circ - \varepsilon - \gamma; \tag{4.10}$$

$$\delta = 90^\circ - \xi = \varepsilon + \gamma = \varepsilon + \sin^{-1}\left(\frac{\sin\alpha}{n_p}\right). \tag{4.11}$$

Using eq. 4.11 we can rewrite eq. 4.7 as:

$$n_{eff} = n_p \sin\theta = (\sin\alpha)(\cos\varepsilon) + (\sin\varepsilon)\sqrt{n_p^2 - \sin^2\alpha}. \tag{4.12}$$

Using the eq. 4.12 it is also possible write the guide mode dispersion equation in terms of angle α instead of angle θ.

If the characteristic of the prism (n_p and ε) are known as well as the substrate refractive index (n_s), and at least two modes are supported by waveguide, we can estimate both thickness and refractive index of the guiding film.

In practice, m-line analysis means the measure of all the incident angles, α_i, for which the *dark lines* in the reflected spot are observed.

Chapter 5

Structural, morphological and optical properties of NCD films

In a plasma process, as the Chemical Vapor Deposition (CVD), the growth parameters dictate the properties of the synthesized material [106]. In the case of diamond, the concentration of methane, hydrogen, the introduction of nitrogen and the deposition temperature play an essential role on the quality of the deposited films. Modulation of these elements leads to a variety of diamond films with different grain sizes, abundance of graphitic phase, and optical transparences.

All the sample used in this work were grown on silicon substrate by researchers of the Institute of Electron Devices & Circuits of the Ulm University - Germany using a high frequency CVD apparatus [107, 108]. The investigation of the electrochemical properties of the nanocystalline diamond (NCD) films (see chapter 6-8) requires a selection of high quality samples.

A powerful method to carry out this selection is the Raman spectroscopy [109]. This is an optical technique which is sensitive to the structure of the material analyzed. Using Raman spectroscopy it is then possible to discriminate between the sp^3 and sp^2 diamond phases determining the goodness of the NCD films [110].

Numerous Raman studies on NCD synthesized by CVD, were carried out with excitations in the visible and near-UV regions. Unfortunately the strong fluorescence and photoluminescence from CVD diamond accompanying these excitations generally limits the sensitivity of the Raman technique. Much better results are obtained using wavelengths in the UV region because they suppress the fluorescence and photoluminescence leading to prevalent contributions from Raman spectra [111]. Moreover UV radiation reduces the dominant Raman scattering from sp^2 C atoms thus increasing the intensity from sp^3 bonding [112].

In addition electrical and contact angle measurements were carried out for a more complete characterization of the diamond surfaces.

It turns out that the best NCD samples have properties similar to single-crystal diamonds. For this reason also optical properties such as transmittance and refractive index are investigate in this work.

A total of 93 diamond films were characterized during this PhD work. For each of the experiments performed (see chapter 6-8), samples were chosen on the basis of their specific properties.

5.1 Example 1

Generally, a set of samples belonging to the same deposition process were provided by the Ulm University. To control the good uniformity of the CVD process along the Si substrate, SEM analysis on all samples have been done.

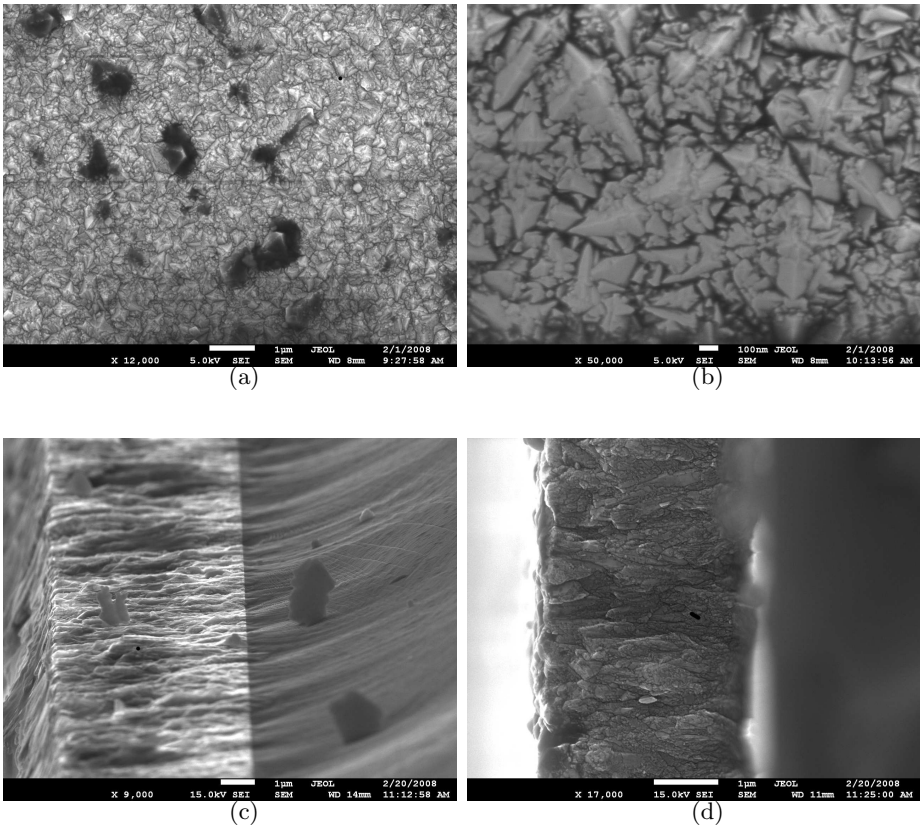

(a) (b) (c) (d)

Figure 5.1: SEM pictures: morphology, grain size and film adhesion on the silicon substrate.

To control the surface homogeneity, images were acquired at low magnifications in different sample points. As an example, in fig. 5.1 four secondary electron images are reported. In the first two images, we can see that the grains show a preferential growth orientation. Also the corrugation of the surface is visible. The morphology presents a mixture of larger grains in the range of 0.5 μm and of smaller grains in the range of 0.2 μm (see fig. 5.1 (b)). Possible inclusions of amorphous carbon at the grain boundaries cannot be detected. The next two images show a section of the NCD film. In both the images a very good adhesion of the NCD film to the substrate appears. Also the thickness of the films can be evaluated.

The degree if roughness of the NCD surface makes the m-line characterization not possible. The big crystallite dimension prevents a good interfacing with the coupling prism and may be cause of damaging. For this reason only transmittance was measured for these kind of samples. At this aim the substrate was removed with hydrofluoric acid to obtain a window to measure the transmittance without any substrate interference. The transparency of CVD diamond films is affected mainly by two factors: light scattering due to surface roughness, and absorption by sp^2 bonded carbon phases [113].

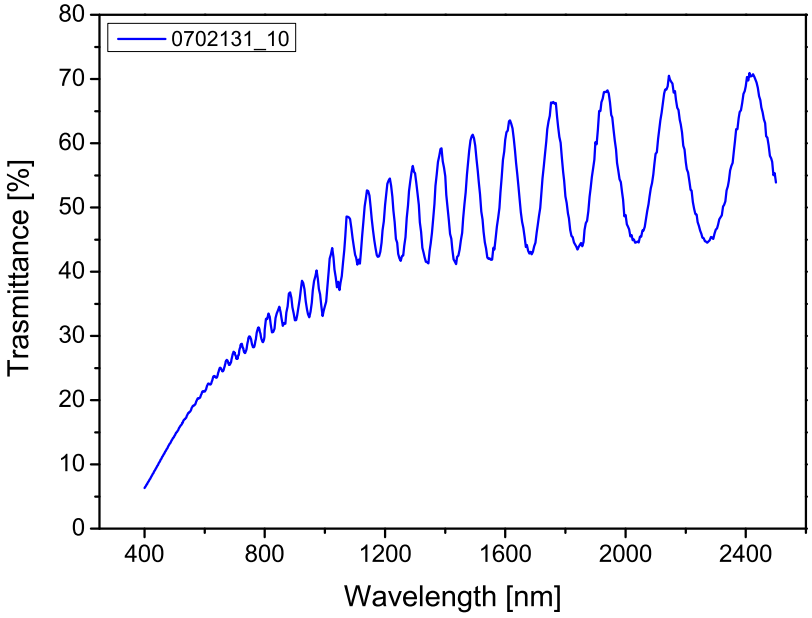

Figure 5.2: Transmittance spectra of NCD thin film (silicon substrate removed).

As shown in fig. 5.2, for UV and visible light below 500 nm wavelength the sample presents low transmittance. This effect stems from the fact that in this

wavelength range only the diamond crystals are transparent, while other carbon phases like graphite or amorphous carbon adsorb light. Above 500 nm wavelength the transmittance is limited by light scattering due to the roughness and to the grains with size comparable to the wavelength.

The oscillating trend of the transmittance is due to the interference between the radiation reflected by the diamond surface and that reflected by the diamond-silicon interface. The oscillation depends therefore on the sample thickness.

Raman spectroscopy was then used to evaluate the film quality. The result is shown in figure 5.3. The spectrum is roughly composed by two main features: a sharp peak at 1332 cm^{-1} which is characteristic of the diamond Raman shift. A second large feature is present at 1589 cm^{-1}. This component represents the G-band which derives from the graphitic inter-grain phase. This component is always presents in the nanocrystalline diamond films Raman spectra.

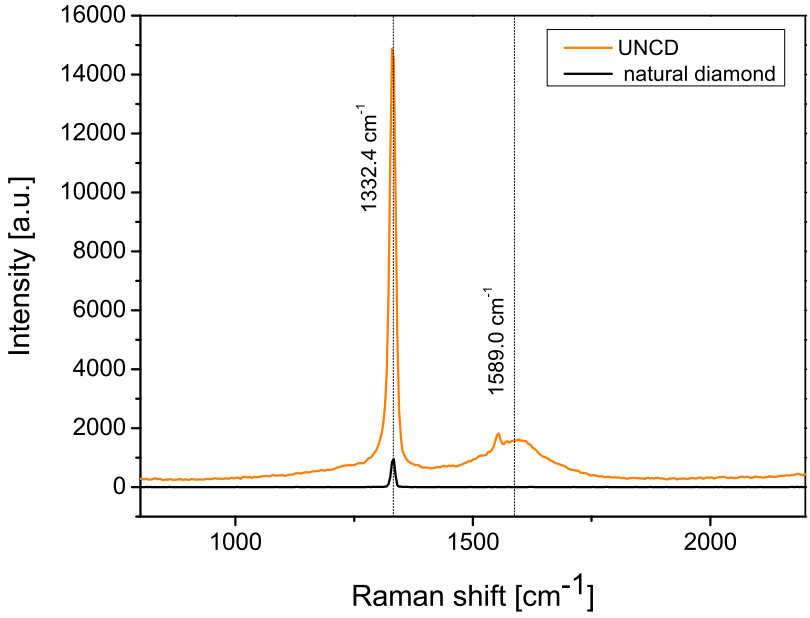

Figure 5.3: UV(λ = 244 nm) Raman spectra.

The correspondent surface characterizations are shown in the next two pictures. Fig. 5.4 shows the survey of the NCD sample. Essentially, on the carbon C1s peak is present (negligible contribution from oxygen). The position of this peak falls at 285.0 eV corresponding to hydrogenated diamond surface. This is confirmed also by the contact angle measurement which is shown in fig. 5.5. The correspondent value of the contact angle is θ = 95 ° and the sheet resistance ρ = 2.7 MΩ/□.

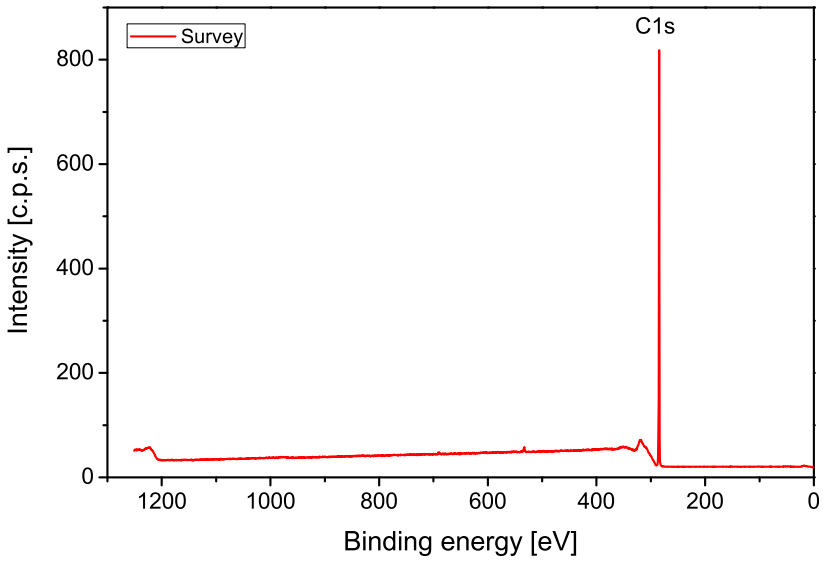

Figure 5.4: Survey spectra.

These values are typical of a good hydrogenated surface. Such kind of samples with perfect hydrogen terminations and negligible oxygen content were selected for the electrochemical characterization which are discussed in the chapter 6.

Figure 5.5: Wetting angle on as hydrogenated diamond surface.

5.2 Example 2

Another set of samples provided by the University of Ulm was composed by 14 heteroepitaxial samples characterized by 150 nm, 100 nm and 20 nm grain size as shown in fig. 5.6. SEM was important to display the different surface morphologies.

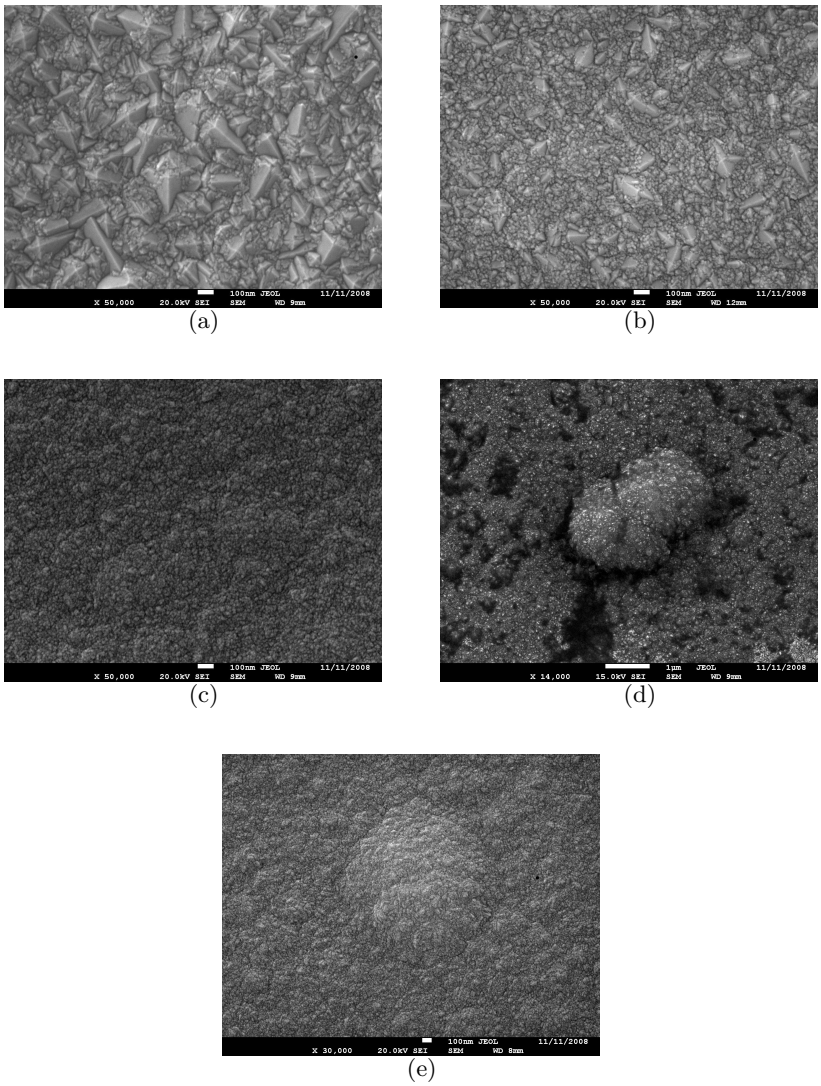

Figure 5.6: SEM image from samples with different surface morphologies and grain size: (a) 150 nm, (b) 100 nm, (c) 20 nm. Pictures (d) and (e) are particular features found on the 20 nm grain size sample

Consistent differences are observed among the dimensions of the grain size as expected. It is interesting to note that, even though the grain size are randomly oriented, samples (a) and samples (b) show a preferential growth orientation. Their morphology presents a mixture of larger grains in the range of 200 nm and of smaller grains in the range of 100 nm. At higher magnification the SEM images reveal a pretty homogeneous surface in the case of the sample (c) characterized by the smaller grain size.

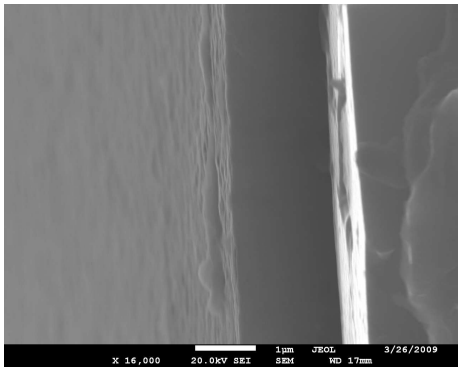

Figure 5.7: SEM section of sample characterized by 20 nm grain size.

The same sample was analyzed along the surface normal. Fig. 5.7 displays the section of the 20 nm grain size sample. The SEM micrograph puts in evidence a perfect adhesion of the diamond film to the silicon substrate and a film thickness which is around 1.52 μm.

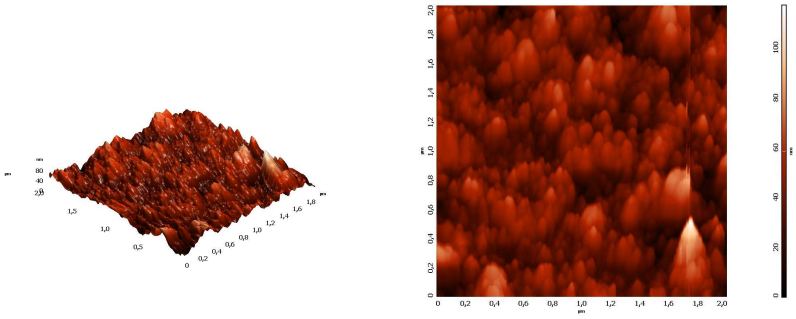

(a) (b)

Figure 5.8: (a) and (b) non contact AFM 5 x 5 μm^2 map of NCD surface .

To better assess the surface roughness several 5 x 5 μm^2 AFM maps were performed on this sample to have a good statistics. An example of AFM map is shown

in fig. 5.8 (a) and (b). The root mean square roughness obtained for the NCD was 12.33 nm. The degree of roughness obtained from AFM is in good agreement with the expected grain size value of 20 nm. This crystallite size is compatible with the m-line coupling technique.

To perform m-line measurements, a Metricon 2010 instrument, was used based on the single prism coupling technique. The system is equipped with the 632.8 nm, 1319 nm and 1542 nm wavelengths and both TE and TM polarizations were considered. A rutile prism (n = 2.8654 @ λ = 633 nm) was used to inject the radiation into the diamond film. To reduce the drawbacks caused by the surface roughness and increase the coupling efficiency, diodomethane sulfur oil (n = 1.7586 @ λ = 633 nm) was uniformly shed between the prism and the diamond surface. Figure 5.9 illustrates

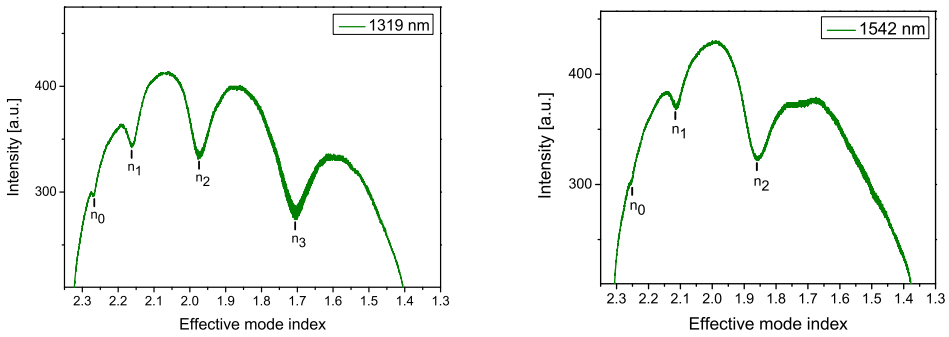

(a) m-line spectra at 1319 nm.

(b) m-line spectra at 1542 nm.

Figure 5.9: m-line spectra, at 1319 nm and 1542 nm, of NCD film on silicon. The vertical lines in fig. (a) and fig. (b) represent the position of the modes in the diamond film.

the m-line spectra in TE polarization of NCD film obtained using 1319 nm and 1542 nm operating wavelengths. No modes were excited with the TM polarized light. By also using a 633 nm laser excitation, no modes were detected. Generally this wavelength is not used to characterize the optical properties of NCD films because at this frequency they exhibit a pronounced absorbance [114]. The values of the refractive index measured in TE polarization at 1319 nm and at 1542 nm are 2.301 $\pm$ 0.001 and 2.299 $\pm$ 0.001 respectively. These values well agree with the refractive index of natural diamond which is 2.390 at 1200 nm and 2.386 at 1500 nm [113] confirming the high quality of our nanocrystalline diamond films.

Figure 5.10 shows the index profile reconstructed from the effective index at 1319 nm and at 1542 nm using *Chiang algorithm*. The index profile exhibits a step-like behavior. Its value is maximum at the surface and remains fairly constant

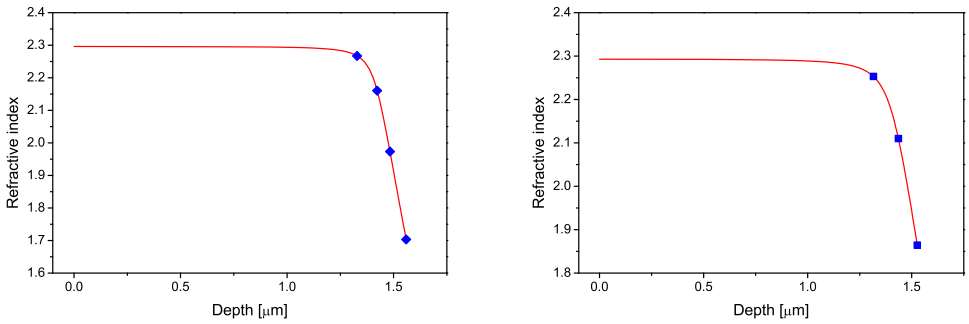

(a) Refractive index profile at 1319 nm.

(b) Refractive index profile at 1542 nm.

Figure 5.10: Refractive index profile of the NCD film reconstructed from measurements at 1319 nm fig. (a) and at 1542 nm fig. (b) respectively. The points shown correspond to the values of the refractive index indicated in the spectra (a) and (b).

throughout the thickness while it decreases rapidly near the film/substrate interface. The constancy of the refractive index along the film thickness is a desired property in view of potential applications.

The NCD film thickness obtained using the m-line technique is (1.57 ± 0.02) μm. This value is in good agreement with those obtained by SEM analysis (1.52 μm).

M-line measurements demonstrate it is possible to obtain effective coupling between prism and NCD film deposited on silicon wafer and this is a further indication of the good optical quality of the film surface. These results indicate that thanks to the good optical properties and the low surface roughness, these NCD films could be employed to fabricate systems for photonic application.

As done in the previous example, the quality of the NCD sample was evaluated also by Raman scattering in the ultraviolet region with excitation at 244 nm (observe the different excitation wavelength respect the previous experiment). The Raman spectrum shown in the figure 5.11 is in agreement whit typical Raman spectra of NCD film [115]. It exhibits three well-defined features. We verified that intensity and position of these peaks do not change for different positions on the film. The peak 1332 cm^{-1} is characteristic of high quality crystalline diamond [116] while the narrow peak 1550 cm^{-1} comes from oxygen of the atmosphere. The broad peak 1579 cm^{-1} is non diamond carbon and it is constituted by two components: 1550 cm^{-1} assigned to diamond like carbon (DLC) phases [117] and the peak at 1580 cm^{-1} assigned to G band [118]. The additional shoulder at 1480 cm^{-1} is related to transpolyacetylene formed during the CVD process [118].

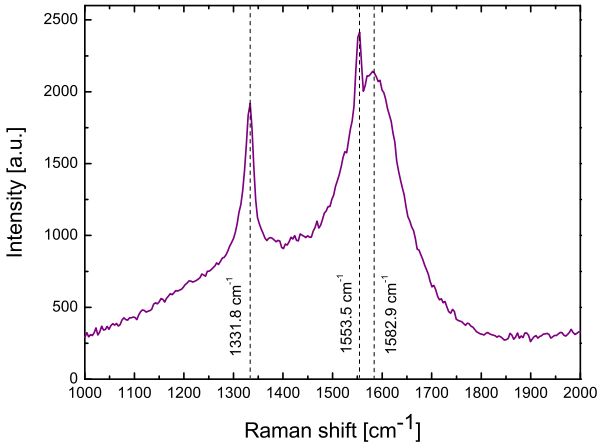

Figure 5.11: Raman spectra from the NCD sample with a 244 nm excitation wavelength.

5.3 Example 3

The previous examples demonstrate that it is possible to grow nanocrystalline diamond films with good optical properties. Surface roughness is one of the major problems considering the propagation of light throughout thin film. Ten ultra-nanocrystalline diamond (U-NCD) thin films deposited on silicon were analyzed to assess if guiding modes are or not supported.

SEM and AFM measurements were performed to characterize the samples surfaces.

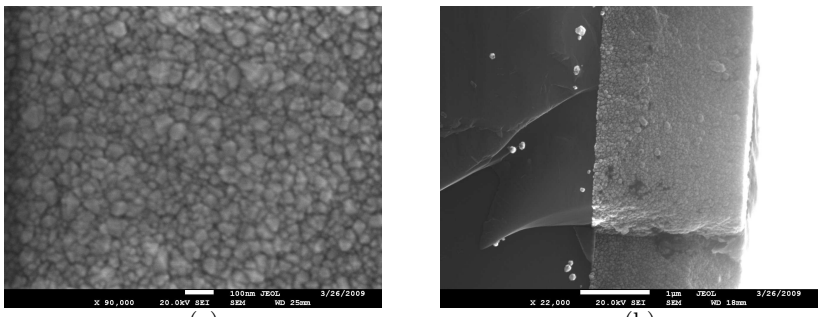

(a) (b)

Figure 5.12: SEM pictures: (a) morphology and grain size; (b) section of thin film.

The SEM image showed in fig. 5.12 (a) reveals a homogeneous surface having a

pretty low roughness. As previously, fig. 5.12 (b) demonstrates a good adhesion of the U-NCD films to the substrate.

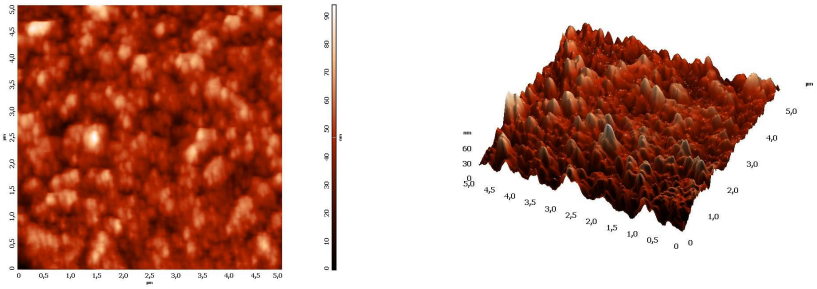

(a) (b)

Figure 5.13: An example of AFM maps from U-NCD films.

To exactly measure the degree of roughness, AFM was used. The topography of the sample surfaces obtained from AFM is reported in fig. 5.13. Unfortuately the surface is more rough than expected. The R_a and R_q parameters were calculated using different 5 x 5 μm^2 and 2 x 2 μm^2 maps. In the first case R_a = 8.81 nm and R_q = 11.1 nm. This value are in agreement with those estimated from 2 x 2 maps: R_a = 8.49 nm and R_q = 10.6 nm.

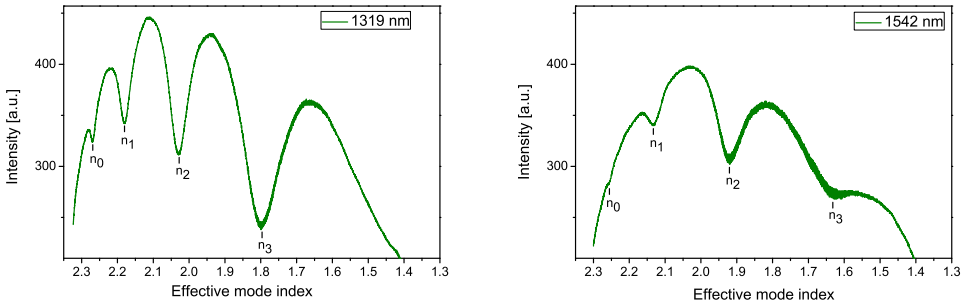

(a) m-line spectra at 1319 nm. (b) m-line spectra at 1542 nm.

Figure 5.14: m-line spectra, at 1319 nm and 1542 nm, of NCD film on silicon. The vertical lines in fig. (a) and fig. (b) represent the position of the modes in the diamond film.

As in the previous case m-line measurements in TE and TM polarizations were performed to measure the refractive index. Figure 5.14 illustrates the presence of guiding modes in TE polarization of NCD film obtained using 1319 nm and 1542 nm

operating wavelengths. No modes were excited with the TM polarized light as well as using a 633 nm laser excitation. Results are listed in table 5.1 which summarizes the refractive index of guiding modes.

Table 5.1: Modes guide refractive index.

λ **(nm)**	n_0 $\pm$ 0.001	n_1 $\pm$ 0.001	n_2 $\pm$ 0.001	n_3 $\pm$ 0.001
1319	2.270	2.180	2.030	1.801
1542	2.253	2.134	1.919	1.637

The values of the refractive index measured in TE polarization at 1319 nm and at 1542 nm are 2.298 $\pm$ 0.001 and 2.290 $\pm$ 0.001 respectively. These values are compatibles with previous values estimated in "Example 2" and with the refractive index of natural diamond which is 2.390 at 1200 nm and 2.386 at 1500 nm [113]. The high quality of our nanocrystalline diamond films was confirmed again. A comparison with the previous samples shows that for $\lambda = 1319$ nm the number of modes increases as well as their intensities.

Raman spectra obtained exciting at 244 nm the U-NCD sample were acquired (see fig. 5.15). In this case the diamond peak is less appreciable respect to the NCD previous samples. The reason of this phenomenon is the pronounced D-band at 1355 cm^{-1} The D-band is associated to small size graphite clusters [119].

The higher intensity of the D-band peak is therefore an indication of higher content of graphitic phases [120] at the gain boundaries due to the reduction of the crystallite size of the U-NCD sample. The sample also shows a sharp G-band at 1580 cm^{-1} and the transpolyacetylene peak at 1480 cm^{-1} [121].

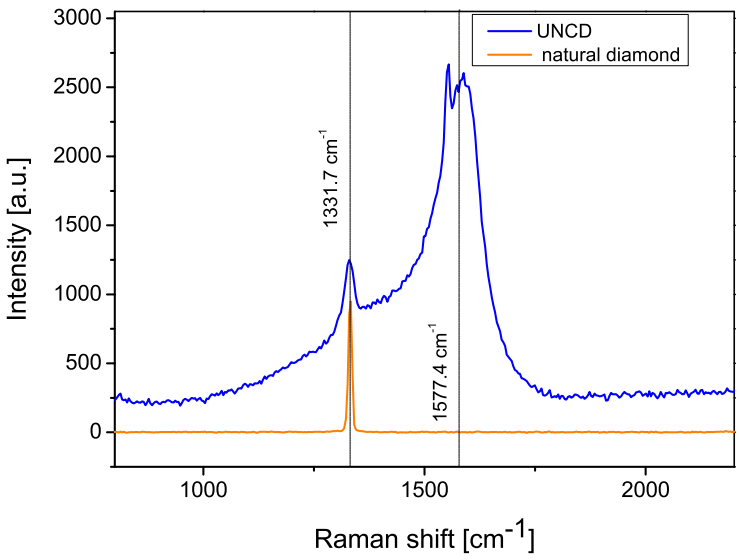

Figure 5.15: Example of UV ($\lambda = 244$ nm) excited Raman spectra.

Chapter 6

Investigation of the diamond surface oxidation by UV irradiation

The current technology offers the possibility to change the diamond termination and graft chemical functionalities in a thinly controlled way. This makes diamond very appealing because this possibility may be exploited for the realization of innovative biosensors. In fact, oxygen may be used to passivate selected zones of the diamond surface rendering them highly resistive. In other zones, the sensing area for instance, hydrogen termination may be used to obtain a semiconducting character. The next step is the chemical activation of the sensing area to enable a molecular recognition. This may be performed attaching for example DNA single strands with appropriate cross linkers and amin groups grafted on diamond. The realization of a biosensor, on the other hand, requires a perfect control of the electronic properties of the surface. Since these last strictly depend on the surface termination, a correlation with the surface chemistry have to be made. This was done for the hydrogen termination. During the last decade a great effort was devoted by many researchers for understanding the semiconducting character of the hydrogenated diamond surface. Not a similar work was done for the oxidized diamond surface. In particular it is still not exhaustively studied how the surface characteristics change in relation to the oxidation process used. To answer this question oxidation induced by UV irradiation in an oxygen atmosphere or induced by wet chemical processes or by plasma were analyzed.

In this chapter a first *in situ* experiment concerning a controlled thermal desorption of oxygen from an UV oxidized diamond surface is described.
In a second *in situ* experiment oxygen desorptions from diamond surface oxidized via traditional processes as chemical attack and plasma were compared with that form

the UV-oxidated surface.

6.1 *In situ* thermal treatment of UV-oxidized H-NCD samples

The experiment

Two hydrogenated NCD samples, obtained from the same wafer, were introduced in the preparation chamber of PHI 454-590 instrument (see section **??**). Both the samples were heated at 400 ℃ for 30 min. in UHV to desorb contaminants and obtain perfectly clean surfaces. Two UV sources were then used to irradiate the diamond surfaces to induce oxidation in the following experimental conditions:

- the D1 sample was oxidized in air for 3 h by a Xe discharge lamp operating at 400 W characterized by a rather intense emission at low wavelengths (maximum intensity in the range 200 nm 600 nm);
- the D2 sample was oxidized *in situ*[1] using a deuterium discharge lamp operated at 24 W (maximum intensity in the range 600 nm 1200 nm) and a O_2 pure atmosphere.

The experimental details are summarized in table 6.1.

Table 6.1: Experimental conditions used for the UV oxidation of the D1 and D2 samples. The first column reports the oxygen concentration measured after UV irradiation.

	O (%)	Duration (h)	Power (W)	Atm. O (%)	Pressure (bar)	Efficiency (%)
D1 Xe lamp	5.6	3	400	20.95	1	0.0223
D2 ^{2}H lamp	8.2	4	24	100.00	1	0.0854

After the UV oxidation XPS was performed on the two D1 and D2 surfaces to measure the oxygen abundance which are summarized in table 6.1.

In situ oxygen desorption was then carried out on both the oxidized samples. At this aim the thermal treatments (TT) were performed on both samples using increasing temperatures and a duration of 30 min. Table 6.2 lists the experimental conditions used for the D1 and D2 annealings.

[1] After the surface cleaning the sample was transferred in UHV in a second small chamber devoted to surface functionalization.

Table 6.2: Description of the thermal treatments (TT) performed on the two diamond samples.

	D1		D2	
	T(℃)	Time (min)	T(℃)	Time (min)
Cleaning	400	30	400	30
Oxidation	//	180[a]	//	240[b]
TT1	400	30	300	30
TT2	400	30	400	30
TT3	600	30	600	30
TT4	700	30	800	30
TT5			970	30

[a] Oxidation performed in *air*.

[b] Oxidation performed in *in situ*.

After each TT, XPS and UPS were carried out to determine the level of oxygen left on the D1 and D2 surfaces and the correspondent change of their electronic properties.

The effect of the UV irradiation on D2 diamond sample C1s core line before and after treatment is shown in figure 6.1.

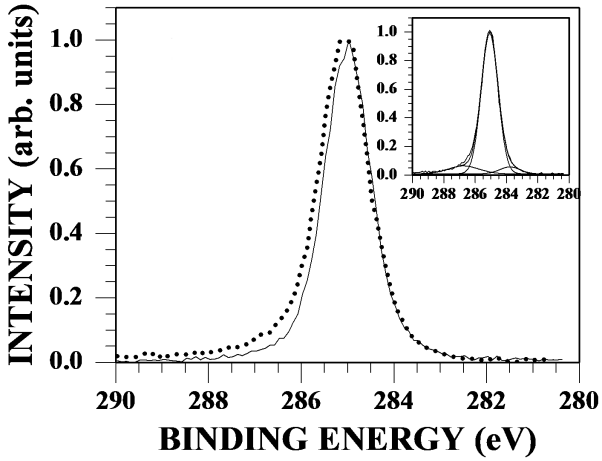

Figure 6.1: A) C1s core line of diamond sample D2 before (solid line) and after in situ UV oxidation (dotted line). An increased tail on the high binding energy side of the oxidized diamond spectrum reveals the presence of ether-like, carbonyl and carboxylic bonds.

The two core lines clearly differ in the presence of carbon - oxygen bonds. The C1s peaks were fitted using Gaussian components, each one corresponding to a specific chemical bond. The broader tail relative to the oxidized diamond surface reveals the presence of different C-O bonds. Peak fitting (not shown) leads to a component related to carboxylic and carbonylic groups, falling at $\sim$ 289 eV and $\sim$ 287.5 eV respectively. Component at $\sim$ 286.5 eV was associated to single carbon - oxygen bonds as in a C-O-C and C-OH configuration. Finally, carbon from pure diamond peaks at $\sim$ 285 eV as commonly found in the literature. At lower energy, non diamond carbon phases likely due to inter-grain phases are found. Observe that spectra are normalized to a common intensity to put in evidence the effect of the UV oxidation.

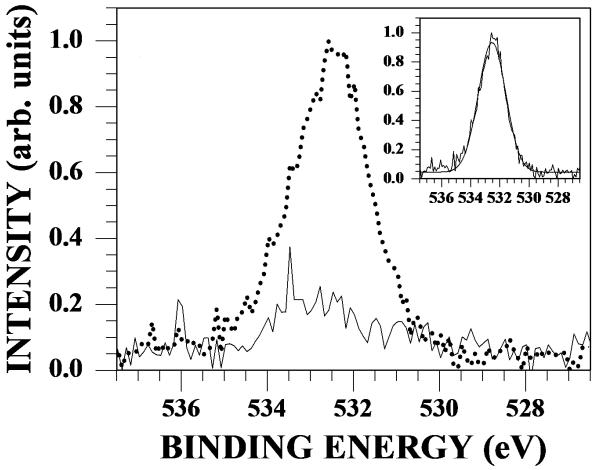

Figure 6.2: O1s core line from the same samples (solid line before, dots after UV oxidation). In the insets an example of the core line fit performed on the spectrum from the UV-oxidized sample.

Figure 6.2 represents the oxygen O1s core line form cleaned and oxidized samples. A remarkable increase of the O1s intensity in correspondence of the UV irradiation may be observed. The insets show an example of the core line fit. It is worth noting that the oxygen atomic concentration (in O%) generated by the UV irradiation on the D1 and D2 surfaces (see table 6.1) refers to oxygen located only on the diamond surface. Since the sampling depth in the XPS analysis is $\sim$ 3-4 nm, the level of the diamond oxidation is very high.

Starting from the experimental conditions in which the oxidations were performed, it is possible to estimate the efficiency of the different photon wavelengths.

At this aim the extent of diamond oxidation was normalized for the UV-lamp power, for the oxygen concentration of the atmosphere in which the oxidation pro-

cess was performed and for the duration of the UV irradiaiton. The results are summarized in the last column of the table 6.1. As can be seen, there is consistent difference between the two lamp efficiencies due to the higher energy of the ^{2}H lamp.

In figure 6.3 is shown the trend of the oxygen concentration estimated for the two D1 and D2 diamond samples during the whole sequence of surface treatments (UV exposure and successive annealing).

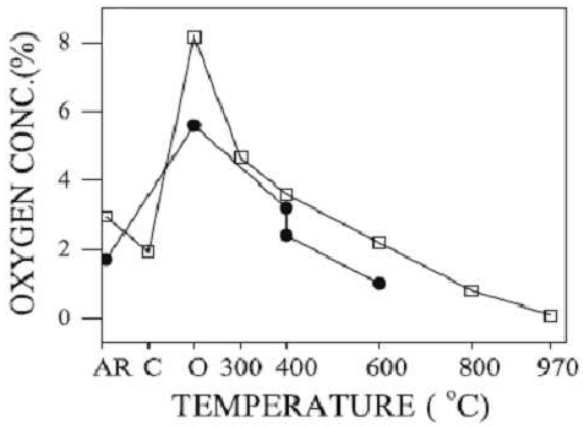

Figure 6.3: Trend of the oxygen concentration in the D1 (black circles) and D2 (open squares) samples as a function of the surface treatment performed (AR = as received, C = cleaned, O = oxidized, numbers represent the annealing temperature).

As can be observed, the thermal cleaning leads to a reduction of the initial oxygen concentration, although it is not completely removed from the surface. Nonetheless, we can assert that the thermal treatment is effective in eliminating the contaminants adsorbed on the diamond surface, as demonstrated by the O1s core line in fig. 6.2. Then we can conclude that the small amount of oxygen left results from within the diamond films and is introduced during diamond deposition.

After oxidation the O % decreases with the thermal treatments applied, indicating a continuous desorption from the diamond surface. We observe that desorption occurs already at 300 ℃, where the thermal treatment induces a reduction of $\sim$ 50 % in oxygen concentration.

These results are also confirmed by the HeI (see fig. 6.4) and HeII (see fig. 6.5) UPS spectra.

The sequence of HeI spectra in fig. 6.4 clearly shows the change in the cut-off position. In particular the cut-off of the second spectrum which corresponds to the cleaned hydrogenated diamond is placed at 17.7 eV the high value on the binding energy scale (BE) among the HeI spectra. Oxidation induces a strong decrease of

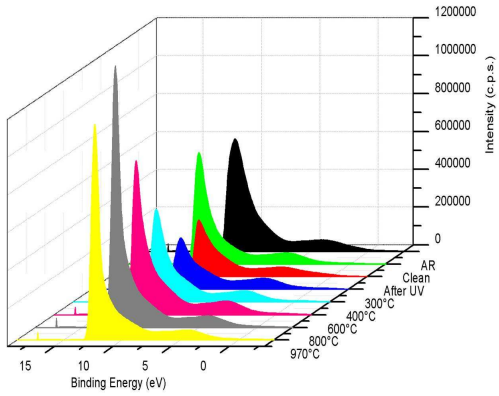

Figure 6.4: HeI (21.2 eV) spectra D2 diamond as function of the treatments applied.

the secondary electron peak. Although qualitative, variations of spectral intensity of the secondary electrons are linked to the electron afnity of the diamond surfaces [**?**]. Interestingly, the intensity of the secondary electron peak increases step by step with the application of the thermal treatments.

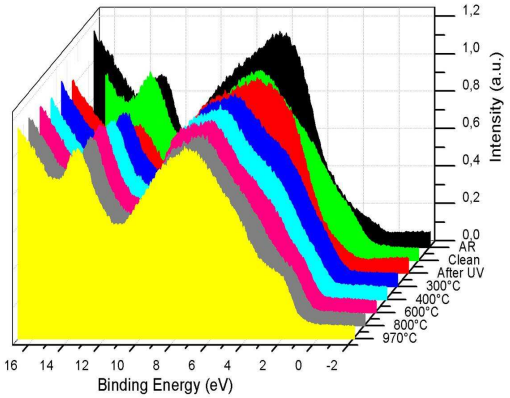

Figure 6.5: The correspondent HeII (40.8 eV) spectra of the virgin and treated diamond surfaces. AR, C and OX means *as received, clean* and *oxidized* respectively, numbers refer to annealing temperatures (℃).

In fig. 6.5 the correspondent HeII spectra are shown. Again the cleaning process leads to a strong change in the diamond density of states (DOS) leading to a valence band (VB) in agreement with literature. Both the oxidation processes induce an evident strong modication of the VB. As it can be seen in the third HeII spectrum, there is a prominent band broadening due to the appearance of the oxygen 2s com-

ponent at $\sim$ 5 eV. Also the feature at $\sim$ 13 eV attens and moves to higher BE. As for the HeI spectra, also in this case the application of the thermal annealing leads to a progressive decrease of the oxygen-related features. As a consequence the VB becomes similar to the original H-terminated diamond spectrum. The HeI, HeII spectral changes induced by oxidation and thermal treatments on the diamond electronic properties are mirrored by the behavior of the electron afnity χ.

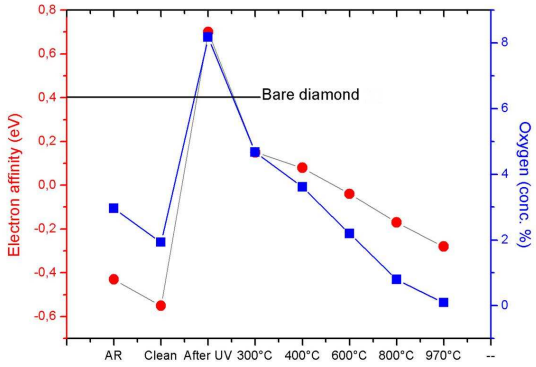

Figure 6.6: Trend of the electron affinity and the oxygen concentration, of the sample D2, as a function of the surface treatments carried out along the experiment. On the abscissa AR, C and OX means *as received, cleaned* and *oxidized* respectively, numbers refer to annealing temperature (℃).

Fig. 6.6 displays the trend of D2 sample χ as a function of the applied surface treatment. The rst annealing at 400 ℃ induces a reduction of the χ due to the desorption of the contaminants. Oxidation causes an abrupt increase of χ with a transition from NEA to PEA. The successive thermal treatments lead to a progressive decrease of the electron affinity which for the highest values of temperature becomes negative again. To appreciate the effect of the in situ UV irradiation, and the annealing treatment fig. 6.7 shows the survey of D2 sample .

The atomic C and O abundances on the two diamond samples estimated from XPS spectra and electron affinity values extimated by UPS are summarized in table 6.3. The cleaned sample shows a more pronounced NEA of - 1.55 eV, while a change from NEA to a positive EA (PEA) of 0.7 eV is obtained after surface oxidation as expected. The electron affinity then decreases with the number of annealing cycles and increase of temperature. The trend of the EA reflects that of the O %. A higher reduction of the EA is seen with the annealing at 300 ℃, which, as already observed, removes the higher part of oxygen from the surface. Further increases of the annealing temperature cause oxygen desorption, leading to negative values of the EA. This trend lasts untill to 970 ℃, where the maximum recovery of EA is observed, in spite of possible hydrogen desorption at this temperature.

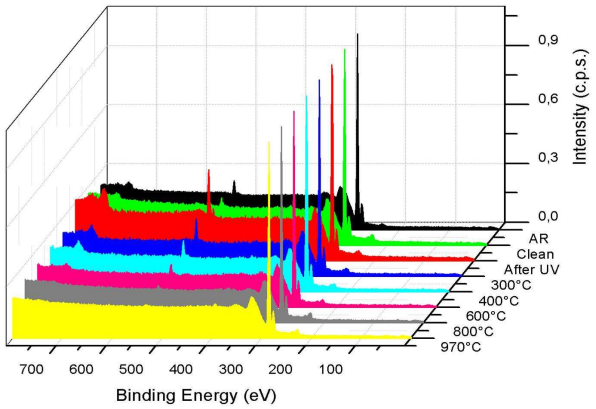

Figure 6.7: Survey of the sample D2 acquired for all the treatments.

Table 6.3: Oxygen atomic abundances (O %) computed from XPS spectra, electron affinity (EA) and cut-off values as estimated from HeI and HeII spectra. (TT: thermal treatment).

	D1			D2		
	O (%)	EA (eV)	Cut-off (eV)	O (%)	EA (eV)	Cut-off (eV)
as received	1.7	-0.06	16.6	2.9	-0.43	16.6
Cleaned	//	-1.26	17.4	1.9	-1.55	17.8
Oxidized	5.6	1.70	16.6	8.2	0.70	16.1
TT1	//	0.89	16.7	4.7	0.15	16.3
TT2	3.2	0.64	16.7	3.6	0.08	16.6
TT3	2.4	0.31	16.8	2.2	-0.04	16.6
TT4	1.0	0.30	16.8	0.8	-0.17	16.8
TT5	//	0.89	16.7	4.7	0.15	16.3
TT5				0.1	-0.28	16.9

Finally, fig. 6.8 shows an example of the effect of sample biasing, which was applied to detect low conductive states during UPS analysis. In the case of conducting surfaces, the position of the cut-off must shift accordingly to the applied negative voltage. Cut-off positions plotted as a function of the bias voltage should fall on a straight line with slope 1. Slopes different from one indicate the presence of surface charging effects i.e. low conductive surface states. In fig. 6.8 the black symbols correspond to the virgin and oxidized diamond surfaces. As it can be seen,

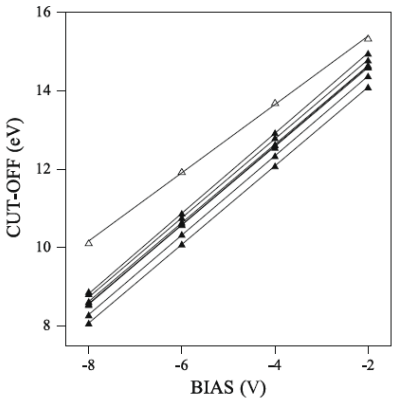

Figure 6.8: Effect of sample bias applied to the *in situ* treated diamond sample. The black symbols correspond to sample surfaces with high conductivity. While symbols corresponds to cleaned hydrogenated diamond surfaces, revealing the presence of charging effects i.e. a low surface conductivity state. Continuous lines show linear fits added as guide for the eye.

the cut-off values move accordingly to the applied voltage (the linear fit slope $\cong 1$). As it appears, there is a small shift among the straight lines. This accounts for the change of the cut-off position depending on changes of the surface termination i.e. electron affinity (EA) variations. The only sample showing a clear charging effect is the cleaned hydrogenated sample (white symbols). In this case, the slope is equal to 0.87 revealing the presence of a low conductive state typical of hydrogen terminated surface in ultra-high vacuum conditions.

Our experimental results point towards the UV oxidation being a rather complex process. First of all, we observe that our experimental results are in agreement with those obtained by Riedel et al. [3]. Although our apparatus does not allow to directly measure the diamond surface conductivity, we are very sensitive to charging effects induced by He radiation during UPS. As shown in figure 6.8, a low conductive state is revealed only in the case of the cleaned hydrogenated surface. The annealing at 300 ℃ performed in UHV leads to the desorption of atmospheric adsorbates and contaminants, but it does not affect the quality of the diamond hydrogenation. This is demonstrated by the electron affinity, which becomes slightly more negative (see table 6.3). In these conditions, the pure hydrogenated diamond surface shows a high resistance and the conductivity is lost [122]. What is surprising in our results is that the low conductive state was readily recovered by oxidizing the diamond surface by direct exposure to the UV irradiation. It is well known, in fact, that oxidation leads to positive electron affinity and to a high surface resistance [28]. In particular,

we observe that this occurs also when irradiation was performed in situ in pure O_2 atmosphere with deuterium generated UV photons.

The surface chemistry

We may now speculate on the different oxidative reactions, occurring on the diamond surface. We first observe, that apart from the different efficiencies in oxidizing the diamond surfaces, the oxidation in air or in pure oxygen atmosphere does not lead to substantial differences in the results. For this reason, the following discussion applies to both the processes. UV activation, performed in a high pure oxygen atmosphere, generates only oxygen radicals due to the lack of other different chemical species. This indicates that in our case a H_3O^+ - HCO_3^- redox couple as proposed by Maier [68] is unlikely to be responsible. In figure 6.9 are reported a series of alternative reactions, which may occur on the diamond surface under UV irradiation.

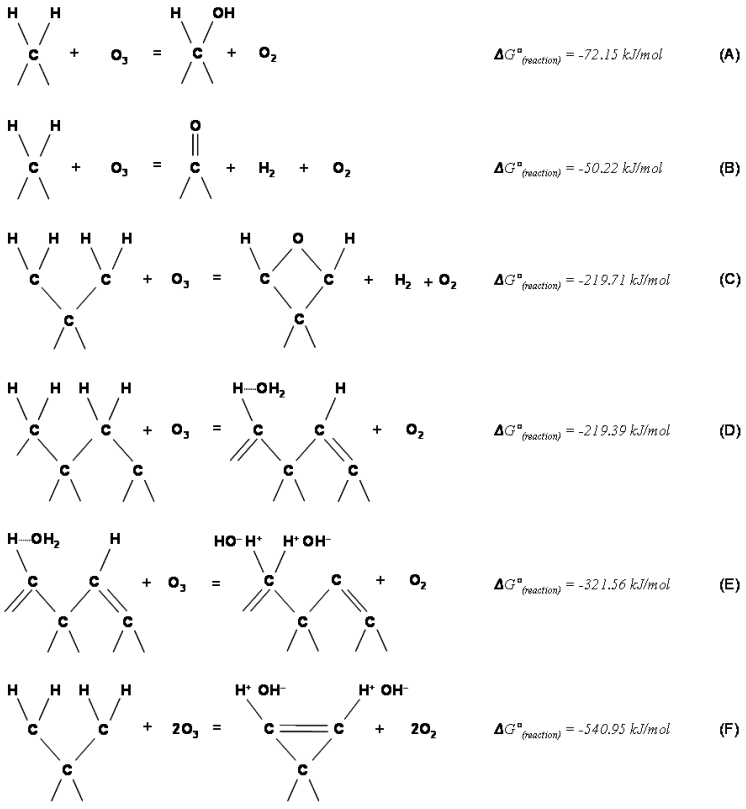

Figure 6.9: Possible oxidation reactions, which may occur on the diamond surface.

A chemical reaction is thermodynamically favored if:

$$\Delta G^{\circ}(products) - \Delta G^{\circ} = \Delta G^{\circ}(reaction) < 0; \tag{6.1}$$

which is the chemical version of the minimum energy theorem. We can estimate the variation of the Gibbs free energy of the reactions sketched in figure 6.9 to determine their degree of spontaneity. The values of the ΔG° (reaction) computed for each reaction are given in figure 6.9. As it can be observed, the Gibbs free energy values indicate, that all the six reactions may occur spontaneously at ambient temperature. Following these values, the process (E) and (F) are the more probable even if ΔG° (reaction) describes only the energetics of a given chemical reaction and it does not contain information concerning the kinetics. Furthermore, on the basis of the ΔG° (reaction) we can classify the six reactions. The reactions (A), (B) and (C) describe three possible oxidation processes, in which a strong covalent C − O bond forms. Different is the case of the second group of reactions, where more electrostatic interactions occur. In this case electric charges are displaced from their original position around H atoms, leading to electric dipoles and to surface conductivity. It is possible to describe the charge exchange i.e. the dipole formation, by computing the change of the chemical potential of the system, undergoing a given redox reaction. As described in previous articles [78, 123] we can apply the Nernst equation which relates μ to the concentration of the oxidizing/reducing chemical species present on the diamond surface at the equilibrium.

$$\mu = \mu_s - \frac{kT}{z} * \ln \left[\frac{\Pi_{i=1}^{N} \left([OX_i] \,/\, [OX_s] \right)^{n_i}}{\Pi_{j=1}^{M} \left([RED_j] \,/\, [RED_s] \right)^{m_j}} \right]; \tag{6.2}$$

where z is the total number of charges exchanged in the redox reaction between the N oxidized chemical species and the M reduced chemical species. $[OX_i]$ / $[OX_s]$ is the chemical activity in of the i-th oxidized species participating the redox reaction with its stoichiometry coefficient n_i. Conversely, $[RED_j] \,/\, [RED_s]$ is the chemical activity referred to the reduced species with its stoichiometry coefficient m_j. It is possible to estimate the value of the chemical potential for the various redox couples described by the four reactions of figure 6.9 B. Let R = $[O_3] \,/\, [O_2]$ be the partial pressure of these elements in the reactions (D), (E) and (F), then equation 6.2 may be rewritten as a function of the pH as:

$$\mu = \mu_s - \frac{0.058}{2} * \left[\log (R) + z * K \right]; \tag{6.3}$$

where z is the number of electrons exchanged in the redox reaction, while K corresponds to the pH, the pOH or the ratio of pH/pOH, depending on the reaction D-F. The pH is let to vary in the range 0 - 14 to describe different concentrations of reactants [68]. The maximum and the minimum values of the chemical potentials relative

Table 6.4: Minimum and maximum valuues of chemical potentials obtained for the reactions D, E and F described in fig. 6.9 for R in the range 0.1-1 and pH in the range 1-14.

Reaction	μ_{min}	μ_{max}
(D)	-5.67	-6.51
(E)	-4.84	-6.10
(F)	-7.27	-7.76

to these reactions are listed in table 6.4. As it can be seen, all potential windows are placed well below the diamond valence band maximum. This information, coupled to the correspondent ΔG° values, points towards the conclusion, that reactions D-F are very likely to occur on the diamond surface.

The system modeling

To further explore the energetics of the system, the hydrogenated diamond surface was modeled using the semi-empirical Modified Electronegativity Equalization Method (MEEM) [124]. After Parr and Pearson [125] the chemical potential of a given chemical element may be expressed as

$$\mu_0 = \frac{(I + A)}{2} = \chi^0; \tag{6.4}$$

where I is the ionization potential and A the electron affinity of the chemical element, while μ_0 and χ^0 are its chemical potential and its electronegativity in the neutral state respectively. After a chemical reaction, χ^0 changes in relation to the oxidizing/reducing power of the other reactants. A charge transfer among the elements will take place until any differential among the electronegativities of the elements is eliminated (χ equalization). The equalized χ corresponds to the system chemical potential at the equilibrium. No information on the path, how equilibrium is reached is contained. From literature [64,65,70,126–128], the position of the VBM for a (111) oriented diamond surface may be located at a mean value of 0.7 eV below the Fermi level. Assuming 1.3 eV for the NEA, and taking 5.5 eV for the diamond energy gap as commonly assumen, EF is located at - 3.5 eV below the vacuum level.

To model the hydrogen terminated diamond surface, a cluster composed by 48 carbon atoms organized on a diamond structure was considered. 46 hydrogen atoms were used to saturate the bonds on the cluster surface as shown in figure 6.10 A.

The application of MEEM led to a chemical potential of the system of - 3.45 eV, which well correlates with the value of - 3.5 eV. Similarly, we computed also the

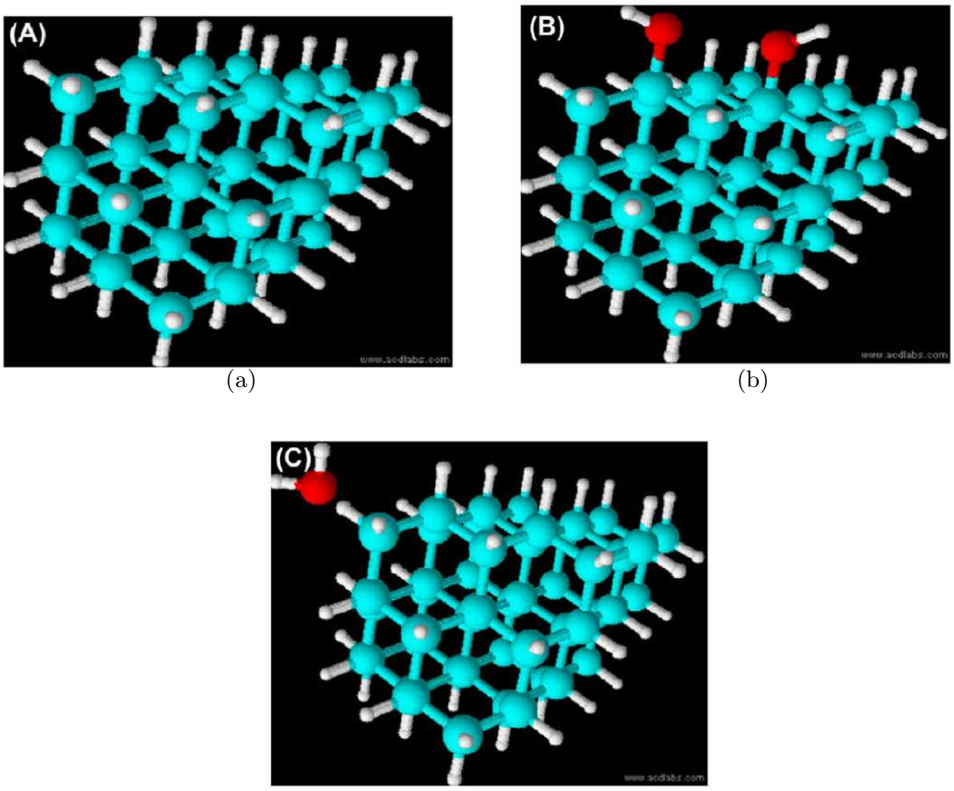

(a) (b) (c)

Figure 6.10: The clusters of diamond structured C atoms used for the estimation of the chemical potential. (A) Simple H-termination; (B) the weak interaction with two OH groups; (C) the hydrogen bond with a water molecule.

chemical potentials of the OH- and H_2O chemical species, which was equal to - 4.17 eV and - 4.6 eV respectively. As it can be seen, there is a rather large difference between the chemical potential of the hydrogenated diamond surface and that of OH- and H_2O, which in our hypothesis correspond to the second element of the redox couple. Then, the reactions D-F lead to a reduction of the energy of the system. Also, for the two systems shown in figure 6.10 B, and C the MEEM gives a chemical potential which levels at around - 3.5 eV. This value is not so different form 3.45 eV obtained from MEEM for the hydrogenated diamond cluster. Nonetheless we can then conclude that the interaction with an OH or an H_2O molecule leads to a reduction of the system chemical potential i.e. more stable condition.

Oxygen desorption and Electron affinity recovery

On the basis of these reactions we can now explain the recovery of the diamond surface properties.

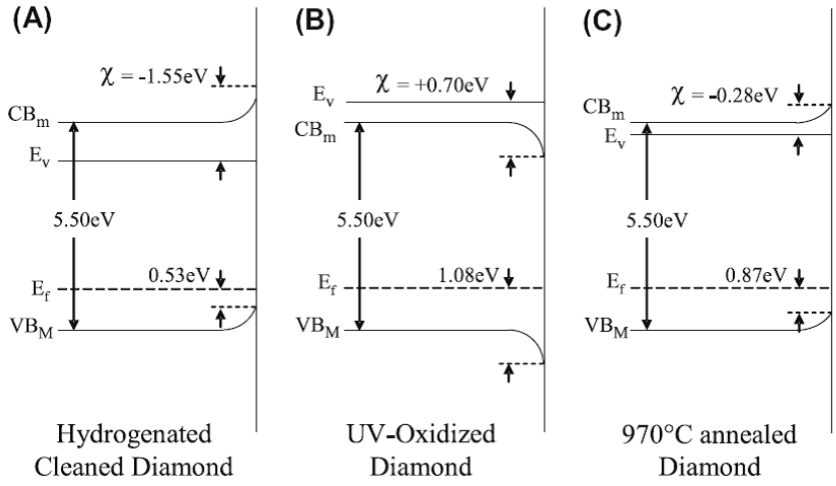

Figure 6.11: Band diagrams relative to the *in situ* treated diamon sample.

Figure 6.11 A shows the cleaned hydrogenated NCD with a negative electron affinity of - 1.55 eV. The reactions D-F lead, in fact, to interactions between the hydrogenated diamond surface and H_2O (through a hydrogen bond) or between H^+ and OH^-. It is known that the formation of covalent C-O bonds leads to a NEA to PEA transition as we observed experimentally (see table 6.3). This situation is described in figure 6.11 B where the reversal of the surface dipoles leads to a change of the band bending and the electron affinity becomes positive. It is also known that the thermal desorption of oxygen occurs at temperatures of $\sim$ 600 ℃ [129, 130] with emission of CO and CO_2. Other authors found a dependence of oxygen desorption on the diamond surface orientation [131]. For the (1,1,1) oriented hydrogenated diamond surface the authors found two peaks at 790 ℃ and 1030 ℃, while only one peak in the range of 760 - 890 ℃ was found for the (1,1,0) oriented diamond surface. Peaks at lower temperature were ascribed to desorption effects from the sample holder. These results are in contrast with those obtained by Foord et al. [5]. For a hydrogenated diamond surface activated with atomic oxygen these authors found CO and CO_2 desorption peaks at temperature of only 150 ℃. This is in agreement with our results, which show a decrease of the density of oxygen at 300 ℃, a temperature, which is lower than the one reported in the literature for CO and CO_2 desorption. In addition, as in our case, oxygen radicals were used also in the experiment of Foord.

Finally, the desorption of CO and CO_2 molecules leads to an irreversible damage of the hydrogenated diamond surface, which cannot explain our recovery of the NEA. The reduction ($\sim$ 50 %) of oxygen at only 300 °C enables us to hypothesize on the presence of weak O - H interactions as in the case of reactions D-F. In agreement with theoretical calculations [132], these bonds may break even during moderate thermal treatments, still leaving hydrogen on the diamond surface. The processes D-F allow us to explain also the recovery of the negative electron affinity as shown in the band diagram in figure 6.11 (C). Following these chemical reactions, the O atoms do not replace H atoms letting the original surface unchanged. Finally, these weak interactions lead to the formation of H-related holes. To explain the conductance recovery after UV activation, Riedel et al. [122] hypothesized an oxygen-defect based conductivity. This mechanism cannot explain our results because, following the Riedel model, our oxygen concentration should correspond to an irreversible oxidized surface in a low conductivity state. Our model explains the presence of correct surface dipoles and the subsequent diamond conductivity.

The role of grain boundaries

A final remark concerns the nature of our samples, which are nanocrystalline diamond films, and the role of the grain boundaries. There is a wide range of literature, showing the effect of grain boundaries on the diamond electronic properties. The amorphous carbon phase may strongly affect the surface conductivity, decoupling it from the kind of the diamond surface termination. There are experiments, showing that grain boundaries act as conducting channels, leading to electron exchange between NCD electrodes and an electrolytic solution [133]. In this case, the performances of ISFETS used as pH sensors are consistently lower in respect to those of the single crystalline diamond based devices. Other authors [134] found, that in NCD the conductivity is temperature dependent. They proposed a model, in which hydrogenation creates acceptor states and the hole mobility involves both valence and defects bands. Experiments performed on pn junctions made on doped NCD show a strong influence of the disordered NCD structure, and the junction characteristics seem to depend on both the amorphouos carbon and diamond properties [135]. The influence on the formation of heterostructures was analyzed with specific experiments [136]. Here, different kinds of amorphous networks were created on a diamond surface (pure a-C, hydrogenated a-C, amorphous carbon created via ion irradiation). The effect of such heterostructures is the introduction of π surface states, which pin the Fermi level E_f. This leads to a downward band bending due to a depletion of holes at the surface. Finally, NCD electrodes reveal a small response to changes of pH in titration experiments [137]. The presence of heterostructures can determine a loss of the ISFET pH sensitivity caused by the Fermi level pinning. In other words the ISFET pH insensitivity is ascribable to the lack of a good diamond/electrolyte cou-

pling with a drop of carrier density variations upon pH changes. All these effects lead to the conclusion that in NCD most of the findings are determined by the presence of defects and grain boundaries, which seem to control most of the material electronic properties. Although we are not excluding their influence, our experimental results cannot be explained without the formation of a redox couple on the diamond surface. The desorption of contaminants by thermal treatments leads to a reduction of the surface conductivity, which excludes a long range carrier transport along graphitic channels. In our case, the Fermi level appears not pinned, which is in contrast to the presence of a high density of defect states. Finally, the studies of Landstrass et al. [72] show the presence of an amorphous graphitic phase in their NCD Raman spectra. Nonetheless, the resistivity of those hydrogenated films strongly increases with sample annealing. The Landstrass interpretation points towards the role of hydrogen of passivating defect related traps and providing shallow acceptors, which dominate the conductivity of their NCD films. The annealing, which has an influence on the hydrogen concentration, should not change the structure and the chemistry of the amorphous phases around the diamond grains, but, as in our case, has a strong influence on the surface conductivity. In our NCD samples, the recovery of the NEA values after the thermal treatments, shows that the grain boundaries do not dominate the surface properties, because in this case the NCD annealing should lead to positive electron affinity typical of PAI terminations, but they may have an effect on the dynamics leading to equilibrium.

6.1.1 Conclusions

The process of UV oxidation of hydrogenated diamond surfaces was analyzed using UV and X-ray photoelectron spectroscopy. A series of six different chemical reactions are hypothesized to explain the recovery of the negative electron affinity with the application of thermal treatments. The experiments show that after UV activation there is a consistent increase of the oxygen concentration on the diamond surface and a transition from a negative to a positive electron affinity. On the contrary, the application of thermal treatments leads to a strong reduction of the oxygen concentration. At the same time a corresponding decrease of the electron affinity was observed. In particular, at the higher annealing temperatures, NEA values similar to those of the cleaned hydrogenated diamond were obtained. The recovery of the initial surface properties is explained on the basis of specific chemical interactions between the hydrogenated surface and the oxygen radicals produced by the UV irradiation. These reactions can also explain the presence of surface conductivity indirectly observed by polarizing the diamond samples.

6.2 *In situ* study of oxygen thermal desorption from NCD surfaces oxidized by different processes

In this section we want to compare three diverse procedures used to obtain high oxidation degrees of diamond surfaces. Aim of this study is to understand if the three procdures induce different carbon - oxygen bonds on the diamond surface leading to different electronic properties.

In the first procesure the diamond sample was immersed in a piranha solution (H_2SO_4 plus H_2O_2 in proportion 3:1) at 110 ℃ for 5 h. In the second one a plasma treatment (30 sccm O_2, 50 W RF power for 10 sec., at a pressure 0.03 mbar) was performed using a COPRA GTE200 source. Finally UV irradiation for 4 h in a pure O_2 atmosphere using a 24 W deuterium lamp was used.

The efficiency of the different oxidation methods is described in table 6.5 where the XPS concentrations of oxygen induced by the three oxidation methods are summarized.

Table 6.5: Atomic abundances of oxygen estimated by XPS spectra after diamond surface oxidation utilizing piranha solution, plasma treatment and UV irradiation.

	O conc. (%) ± 1%
Piranha	17.2
Plasma	11.1
UV irradiation	6.3

It can be observed that the wet process causes the higher sample oxidation while the UV irradiation the lower. On the other hand different kind of chemistry has to be expected as a result of the three different oxidation routes.

Figure 6.12 shows the C1s core lines acquired on the three surfaces just after the conclusion of the oxidation. In the inset an example of peak fitting is also shown.

With increasing the binding energy (BE) respect to the position of pure diamond (285 eV) the Gaussian components are associated to ether-like, carbonyl and carboxyl bonds respectively. To compare the effect of the different oxygen concentration on the diamond properties and if the carbon-oxygen bonds are equivalent, oxygen thermal desorption was performed for each oxidized surface. HeI and HeII spectra were acquired after each thermal treatment to determine changes of the electronic properties of the diamond thin films as a function of the oxygen abundance. At this aim linear fittings were performed to estimate the cut-off position from the HeI on the high energy side of the spectrum and the valence band maximum (VBmax) on the low energy tail of the HeII spectrum. The values of these parameters are summarized

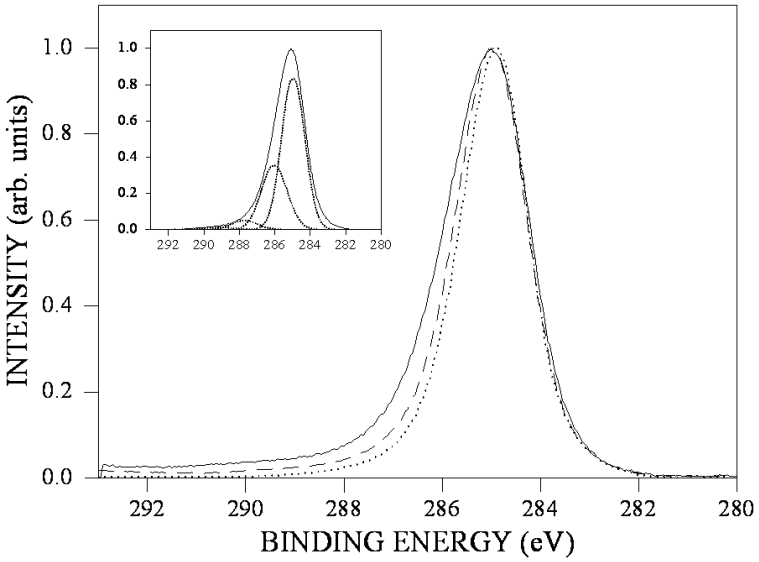

Figure 6.12: C1s core line together with the deconvolution in Gaussian component obtained from piranha oxidized diamond (solid line), O_2 plasma treated diamond (dashed line), UV irradiated diamond in pure O_2 atmosphere (dotted line). The subplot shows an example of peak fitting performed on the piranha oxidized sample.

in table 6.6 together with the value of the correspondent electron affinity (EA). As

Table 6.6: values of the cut-off and VBmax positions estimated on the cleaned diamond surfaces oxidized utilizing piranha solution, plasma treatment and UV irradiation, before oxygen desorption.

	Cut-Off (eV)	VBmax (eV)	E.A. (eV)
Piranha	17.3	3.4	1.8
Plasma	16.5	2.4	1.6
UV irradiation	16.8	2.9	1.8

it can be observed there some differences among the three samples. In particular the distance of the cut-off and of the VBmax respect to the Fermi energy results higher in the case of the piranha treated surface while, irrespectively of the oxygen concentration, it is minimal in the case of the plasma treated diamond. Intermediate values are assumed by the UV irradiated surface. Consistently, EA assumes the lower value in the case of plasma treated diamond. In panels (A), (B) and (C), figure

6.13 displays the trends of the oxygen concentration as a function of the annealing temperature for the different oxidation methods. All the three sample surfaces show

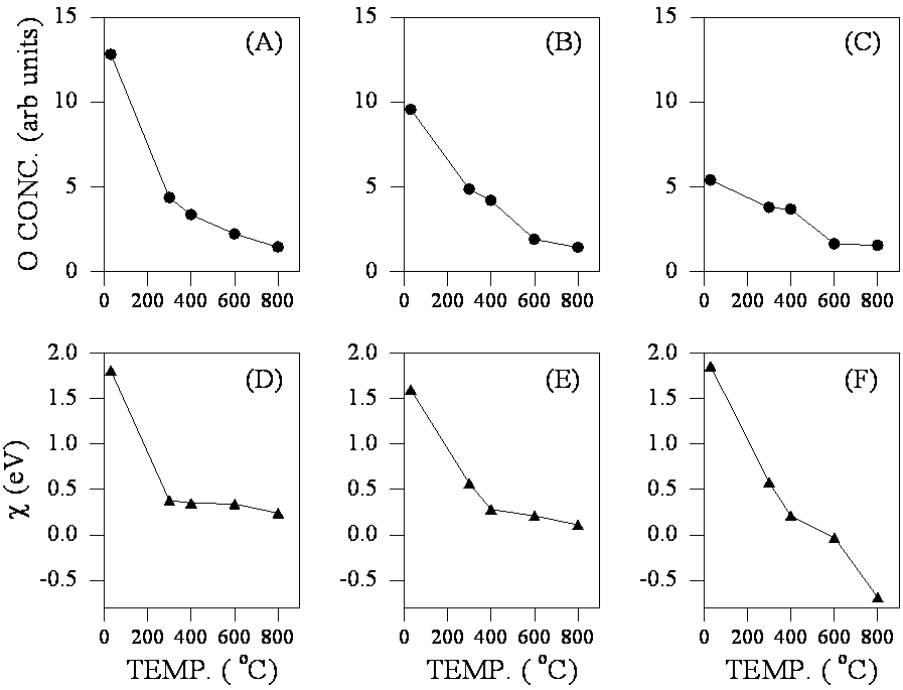

Figure 6.13: Trend of the normalized oxygen concentrations as a function of the desorption temperature: (A) piranha oxidized diamond, (B) O_2 plasma treated diamond, (C) UV irradiated diamond in pure O_2 atmosphere while in panels (D), (E) and (F) are plotted the correspondent electron affinities.

that the concentration of oxygen strongly decreases after the heating treatment at 300 ℃. Unexpectedly the decrease is higher for the piranha treated sample. Increasing the annealing temperature the oxygen desorption proceeds at a lower speed. The change of desorption rate is less evident in the case of the other two diamond films. Different kind of carbon-oxygen bonds could explain this trend since a high temperature is expected to break strong covalent bonds. In agreement with literature, this occurs at temperatures higher than 600 ℃. Although oxidation performed via RF plasma sources and UV radiation efficiencies are very different, in both the cases an electromagnetic radiation leads to the formation of ionized chemical species which can react with the diamond surface. Different oxygen abundances are produced but similar trends of oxygen desorption are seen in these two cases. The trend of the electron affinity reflects that of oxygen. This can be readily explained considering that the value of EA is related to the density of the electric dipoles present on the

diamond surface. As a consequence, after the first annealing, the electron affinity has an initial marked decrease in the case of the piranha treatment. EA remains more or less constant till to 600 ℃. Further increases of temperature causes a small oxygen desorption and then small variations of the electron affinity. The minimum EA value, achieved at 800 ℃ is comparable to that of a π terminated surface. Similar is the case of the plasma oxydized surface. In this case, even if the plasma treatment was mild to avoid surface damaging, the concentration of oxygen found on the surface is higher than that of the UV irradiated sample (see table 6.5). As in the case of the piranha treated diamond, the trend of the electron affinity mirrors that of oxygen and reaches a minimum at 800 ℃. Different is the case of the UV irradiated surface. Here the presence of a certain amount of weak bonds is hypothesized allowing an electron affinity recovery [138]. In these weak electrostatic bonds, oxygen does not replace the hydrogen atom involved in the surface termination. As a consequence when the electrostatic bond is broken, an outward dipole is regenerated and the EA becomes slightly negative [138]. To check this interpretation and correlate the modifications of the electron affinity to the surface treatments a careful C1s core line analysis is required.

Results are shown in figure 6.14 where the different behaviors of the ether and carbonyl bond concentrations as a function of the temperature are plotted.

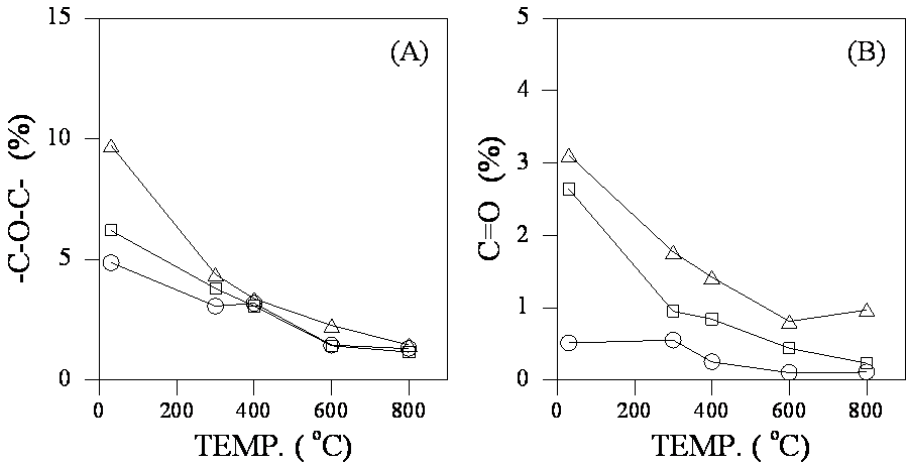

Figure 6.14: trend of the concentration of ether-like (A) and carbonyl (B) bonds in diamond samples oxidized by piranha solution (triangles), by oxygen plasma (squares) and UV irradiation (circles).

The ether like trend shown in figure 6.14 A is similar for the three samples. In all the cases its decrease mirrors that of the oxygen displayed in figure 6.13 for the three treatments. On the contrary, differences are observed in the case of the carbonyl

bonds. The piranha and plasma treatments lead to a certain amount of C=O bonds on the NCD surface. This is not the case of the UV treated diamond where only a very small amount of this kind of bond is found from the very beginning. This is in agreement with data from literature [139] where the effect of different oxidation methods (oxygen plasma, sulpho-cromic acid treatment) on single crystalline and NCD samples is analyzed. Also in that case it was observed that the high energy C1s components (carboxyl and carbonyl groups) are produced to a lower extent by UV irradiation with respect to the other oxidation methods. Similar evidences are shown also by other works obtained on NCD surfaces oxidized with chemical treatments [140, 141]. Following the results of these groups, the carbon oxygen stability increases on going from plasma treatments to chemical oxidation to anodic oxidation [**?**, 140, 141]. XPS analysis performed by these authors found presence of high energy oxygen-carbon bonds in all these treated NCD surfaces which confirms our evidence [140, 142]. Differently the UV treated NCD may be characterized by carbon oxidized components at low binding energies where also electrostatic interactions may be expected. In the other cases oxygen is involved in stronger carbon-oxygen bonds. Breaking these bonds leads to surface reconstruction and may cause surface damaging. Both these effects determine a positive electron affinity.

6.2.1 Conclusions

Three oxidized nanocrystalline diamond surfaces were considerated. They were annealed at the same temperature in UHV (P = 10^{-8} mbar). UPS and XPS were performed after each treatments in order to compare the effect of the same thermal treatment on the differently oxidized surfaces. XPS shows that different oxidation methods produce different abundances of carbonyl and etherlike bonds. The higher concentration of carbonyl groups found in the case of piranha and plasma oxidized NCD shows detrimental effects towards the recovery of negative value of EA. Presence of weaker carbon-oxygen bonds as in the case of UV irradiation, allows a negative electron affinity to be recovered by a thermal desorption of oxygen.

Chapter 7

Amination of NCD surfaces

The possibility to manipulate diamond surface termination is one of the most important peculiarity offered by the diamond surface [143].

The hydrogenated and oxygenated diamond surfaces may be functionalized with covalent grafting of biomolecules in particular amino groups. The formation of $C-NH_2$ bonds are interesting to immobilize biomolecules such as DNA which is very promising for biotechnological applications [144]. Usually amino groups are grafted on diamond surfaces through wet chemistry processes.

The electrochemical reduction of diazonium salts in aqueous solution allows the formation of a strong C-C bond between diamond and organic molecules [145], which may be followed by an irreversible multi-electron and multi-proton modification of the nitro group in amine (NH_2) groups [146]. UV irradiation of hydrogen-terminated diamond surface in the presence of a liquid film containing appropriate alkenes leads to the formation of an organic layer covalently grafted to the surface through C-C bonds.

In the last years also dry methods were reported in literature, as the chemical treatment of a chlorinated surface with ammonia gas under thermal condition [147], [148] or UV irradiation [149].

Recently direct amination of hydrogen-terminated surface using UV irradiation in ammonia gas [150, 151] or using radiofrequency plasmas of mixtures of He + NH_3 has been tested [152]. These new methods are very interesting because they are compatible with the semiconductor technology in order to realize electronic devices as field effect transistor to detect specific biomolecules like DNA [153].

Using UV irradiation to graft amino-groups, the presence of a certain amount of oxygen contamination on the diamond surface is generally reported.

In this chapter I will present our contribution for the study of the innovative technique *one step amination* introduced for the first time by Kawarada [150].

We performed an XPS *in situ* study. This means that the cleaning, the ami-

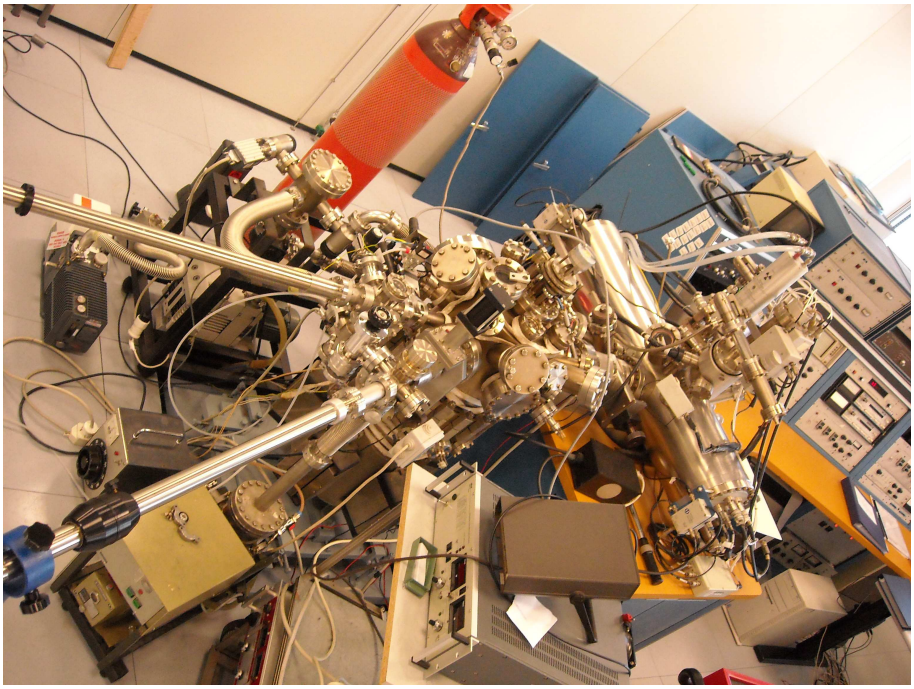

Figure 7.1: PHI 454-590 experimental apparatus see in section 3.4.5 equipped with a second preparative chamber equipped with a quartz win ow to perform *in situ* experiment using ammonia gas.

nation functionalization and the XPS characterization were performed in controlled atmosphere; so the samples never sow the air atmosphere. For this proposal the experimental apparatus PHI 454-590 introduced in the section 3.4.5 was modified. In the picture 7.1 we can see that a second preparative chamber, which was equipped with a quartz window, was connected at the preparative chamber already existing between a gate-valve.

Performing a *in situ* study we are able to understand if the oxygen takes part to the amination process when diamond surface is UV irradiated in an ammonia atmosphere.

Five NCD samples deposited on silicon characterized by H-terminated or O-terminated (chemically oxidized or UV oxidized) surfaces were irradiated with UV photons in different atmospheres (pure NH_3 or $NH_3 + O_2$).

XPS analysis shows, that the presence of oxygen both on the surface and in the gas mixture, strongly increases the efficiency of the UV surface amination.

7.1 H-NCD amination

Firstly two hydrogenated nanocrystalline diamond (H-NCD) samples were utilized in our experiments.

In order to desorb physio-adsorbates contaminants, they were annealed at 400 ℃ for 30 minutes at a pressure of 10^{-8} mbar. After the cleaning the surface hydrogenation was evaluated with Ultraviolet Photoelectron Spectroscopy (UPS), sheet resistance and contact angle. The high degree of hydrogenation of the diamond surfaces have been confirmed by water contact angle ($\theta = 94.77$ °) and sheet resistance ($\rho_s = 2.7$ MΩ / □). The effects of the cleaning treatments and the fully H-terminated clean surface shows a negative electron affinity (NEA) which was measured from HeI and HeII spectra as shown in figure 7.2.

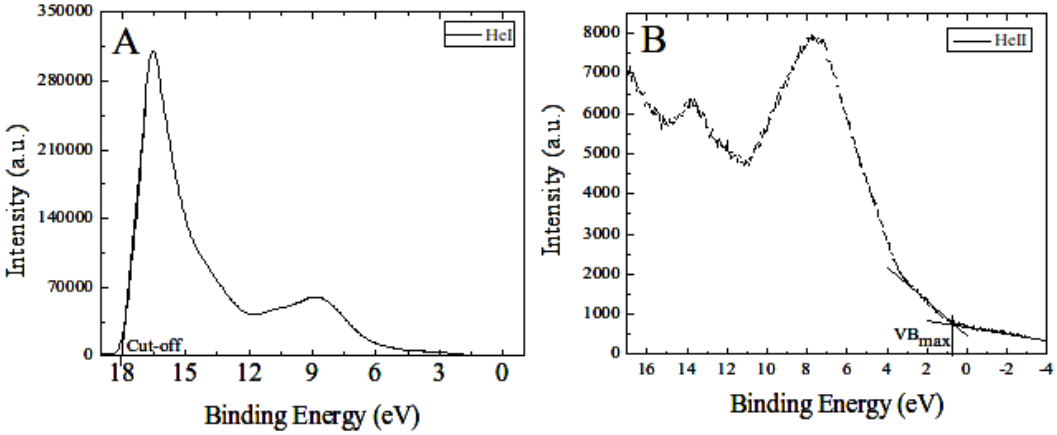

Figure 7.2: (A) HeI (21.2eV) spectrum of cleaned H-NCDa sample. Linear fit used to determine the cut-off position is also shown. (B) HeII spectrum of cleaned H-NCDa sample with linear fit to determine the position of the valence band maximum.

Fig. 7.2 A reports HeI spectra with linear extrapolation of the cut-off ($E_{cut-off}$ = 17.7 eV) instead the fig. 7.2 B shows HeII spectra with linear extrapolation of the maximum valence band (E_{MVB} = 0.64 eV). These parameters lead to a NEA = - 1.59 eV that is in agreement with values reported for hydrogenated diamond surfaces.

The success of the cleaning is also confirmed by XPS measurements. The fig. 7.3 displays the survey of as received (blue line) and cleaned (green line). As a first result we notice that the thermal treatment at 400 ℃ induces a reduction of the amount of oxygen on the diamond surfaces due to contaminants desorption.

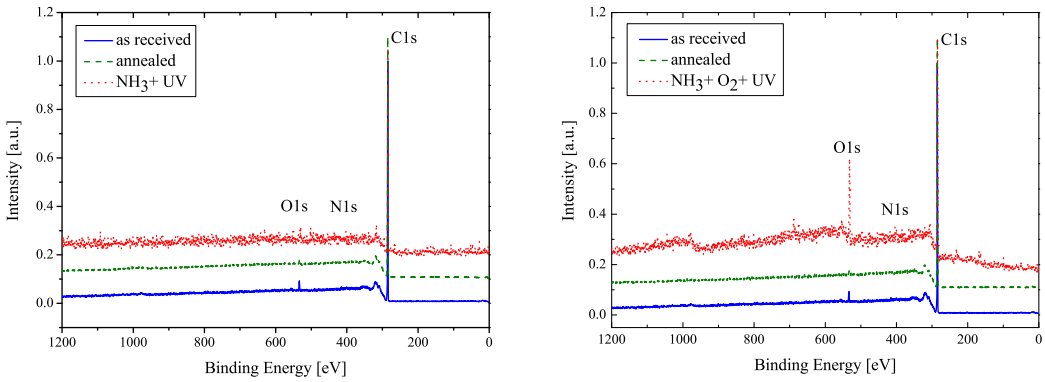

(a) H-NCDa (b) H-NCDb

Figure 7.3: (a) XPS survey spectra of as received (blue line), cleaned (green line) and aminated (red line) H-NCDa sample. (b) XPS survey spectra of as received (blue line), cleaned (green line) and aminated (red line) H-NCDb sample.

Then the H-NCD samples were transferred under UHV in a second chamber equipped with a quartz window (see fig. 7.1). The two samples were UV irradiated using a deuterium lamp (P = 24 W) at room temperature for 4 hours in presence of two different gas atmospheres:

- the sample H-NCDa was irradiated in 99.99 % pure ammonia;
- the sample H-NCDb was irradiated in a mixture of 99.99 % pure ammonia gas with a small amount of 99.99 % pure oxygen.

After the treatments XPS analysis were acquired without to expose the sample at the atmosphere. In the fig. 7.3, which shows the survey of as cleaned (green line) and aminated (red line) samples, we can see that the two different gas atmospheres utilized for the samples H-NCDa and H-NCDb showed different efficiencies in amination the diamond surfaces. In the case of sample H-NCDa the nitrogen content was around 0.3 at. % instead in the case of the sample H-NCDb the presence of a small amount of oxygen in the gas atmosphere led to a final nitrogen abundance of 5.70 at. % (see also tab. 7.1).

The nitrogen core lines of the H-NCDa and H-NCDb samples before and after amination are reported in fig. 7.4. In the case of sample H-NCDa the nitrogen

Table 7.1: Analyzed samples percentage atomic concentration of carbon, oxygen and nitrogen acquired at 90° and 15° (this angle is labeled by *) before the after the amination process.

	C (%) ± 1%	O (%) ± 1%	N (%) ± 1%
H-NCDa	99.20	0.80	0
after amination*	98.82	1.18	0
H-NCDb	99.35	0.65	0
after amination*	83.54	16.46	5.70

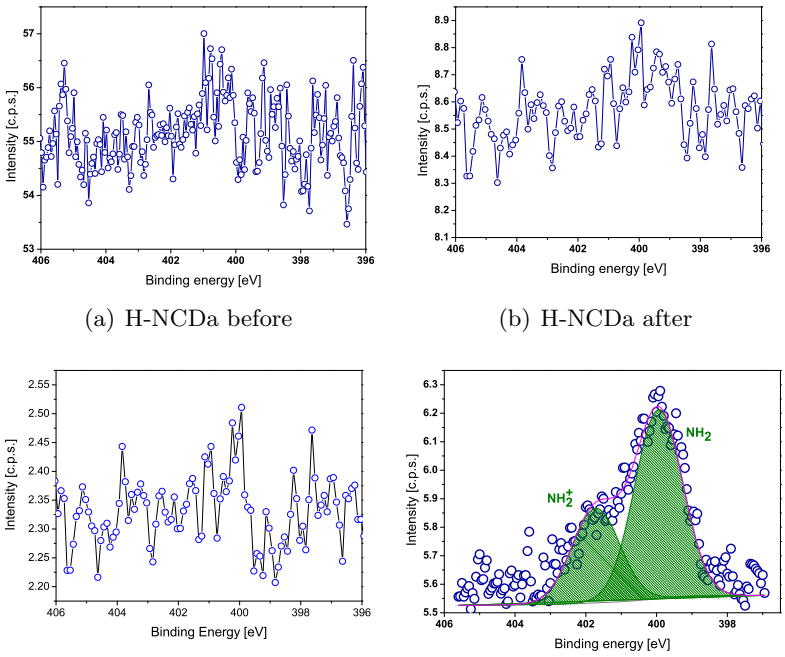

(a) H-NCDa before

(b) H-NCDa after

(c) H-NCDb before

(d) H-NCDb after

Figure 7.4: XPS spectra of the N1s core line.

contribution is hardly visible making peak fitting not reasonable (fig. 7.4 A). On the contrary, the aminated H-NCDb sample possess a well defined N1s peak deriving from the contribution of two distinct chemical bonds, as reported in figure 7.4 B). Two gaussian components are used for peak fitting: $C-NH_2$ is associated to the peak at 399.9 eV, while $C-NH_3^+$ is associated with the peak at 401.7 eV.

In order to understand if the oxygen is needed in the *one step amination* in molecules gas or if it could to play a role also in chemical bonding, another experiment concerning oxidized diamond surface were performed (see 7.2.)

7.2 O-NCD amination

With the main to understand which kind of oxygen is need to graft amimo groups on diamond surface, three different oxidation techniques were applied at three as-grown hydrogen-terminated films:

1. O-NCDc was exposed to an oxygen plasma stream using a COPRA GTE200 RF plasma source operated at 50 W for 10 sec. at a pressure of 0.03 mbar with a 30 sccm O_2 flux;

2. O-NCDd was produced via wet chemical oxidation using a piranha mixture (H_2SO_4, H_2O_2 in proportion 3:1 at 110 ℃ for 4 h);

3. O-NCDe was photochemically oxidized by UV-illumination for 4 h at 24 W in pure 2 bar O_2 atmosphere.

After oxidation, all the samples (plasma, acid, UV), were transferred without further cleaning in analysis chamber to perform XPS analysis. The C1s and O1s core lines were acquired to evaluate the diamond samples oxidation degree.

In order to obtain information on the chemical groups present on the surface, the chemical shifts of the C1s and O1s components were investigated. Fig. 7.5 shows core level peak-decompositions of the C1s and the respective O1s core line for the hydrogenated as-grown thin film (Fig. 7.5 a-b) and for the three different oxidized diamond samples (Fig.7.5 c-h).

Since the position of the NCD C1s core level changes because band bending, we fixed the most intense C^{II} component of C1s stemming from bulk sp^3 C-C bonds, at 250.00 eV. In all of the samples a very small contribution, indicated with C^I, due to π-bonded carbon atoms placed at $\sim$ 284 eV was found. It is likely deriving from the inter-grain non-diamond phase typical of any NCD. In the as-grown and in the O-NCD the contribution C^{III} of the CH_x groups are located at $\sim$ 0.5 eV higher binding energy respect to to the bulk sp^3 C-C bonds. Even if this component does not provide direct information about the abundance of hydrogen on the NCD surfaces, its position and intensity are very important in relation to amination as it will be discussed later on. Concerning oxidation, the three different methods induced the same kinds of oxygen-carbon bonds on the diamond surface. Referring to the core lines analysis shown in the fig. 7.5 we assigned CIV at $\sim$ 286.5 eV to C-OH- or C-O-C- bonds, CV at $\sim$ 288 eV to -O-C-O- and C^{VI} at $\sim$ 289 eV to (O=C)-O-. These chemical shifts are typical of carbon oxygen bonds found in organic and carbon-based

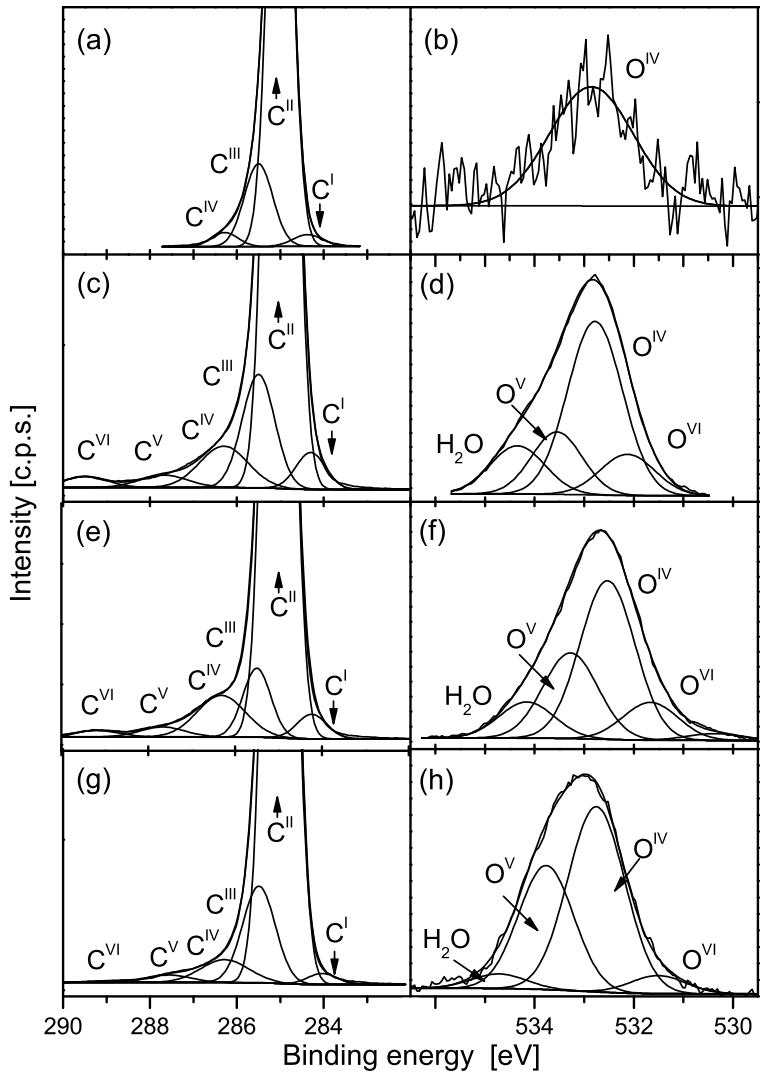

Figure 7.5: C1s (a, c, e, g) and O1s (b, d, f ,h) core-level spectra whit their corresponding peak fits. (a-b) H-NCD after cleaning process; (c-d) O-NCDc after plasma oxidation; (e-f) O-NCDd after wet piranha oxidation; (g-h) O-NCDe after UV oxidation.

materials [139], [154] are also valid for carbon-oxygen groups on diamond surfaces. If we consider the carbon-oxygen bonds, the component C^{IV} always is the dominating one.

Fig. 7.5 shows also the oxygen O1s core level analysis for each sample. The shift of oxygen components (C-OH, C-O-C, -O-C-O-) are very close in energy and for this reason, the O1s analysis is possible correlating the area of the C1s components with O^I components. For all the samples the abundance of each oxygen component (C-OH, C-O-C, O-C-O- and O-(C=O)-) was correlated with the correspondent from C1s to satisfy the relative stechiometry.
As a first result all the oxidation methods strongly increase the oxygen atomic concentration confirming their efficiency. Typically the as-received samples after cleaning showed $\sim$ 0.4 % O atom., while, after the treatment, we obtained 7.3 % for plasma, 7.8 % for piranha, 3.8 % for UV irradiation in oxygen atmosphere, respectively.

After the oxided surface characterization the sample were introduced in the UHV preparation chamber to perform the amination experiment *in situ*.

The three samples were irradiated in 99.99 % pure ammonia with the same deuterium lamp condition used for the H-samples (see section 7.1). After amination the surfaces were characterized by XPS without to expouse diamond surfaces sample at the atmosphere.

In the table 7.2 the atomic concentrations of all elements found on the diamond samples surface are reported. Non negligible nitrogen concentrations were found on all the O-NCD samples after UV irradiation in ammonia atmosphere. XPS analysis

Table 7.2: analyzed samples percentage atomic concentration of carbon, oxygen and nitrogen acquired at 90°and 15°(this angle is labeled by *) before the after the amination process.

	C (%) $\pm$ 1 %	O (%) $\pm$ 1 %	N (%) $\pm$ 1 %
H-NCDc	92.73	7.27	0
after amination	91.36	4.57	2.49
after amination*	88.27	6.34	4.10
H-NCDd	91.51	7.82	0.29
after amination	89.84	6.26	2.67
after amination*	85.93	7.99	3.75
H-NCDe	96.15	3.85	0
after amination	94.78	3.25	1.14
after amination*	93.28	4.41	1.34

of the N1s (see fig. 7.7) core level points out the presence of just one component at 400.2 eV related to $C - NH_2$ bonds. No evidence of C-NO (410 eV) chemical bond was found, confirming that exclusively amino groups are grafted by UV photons on

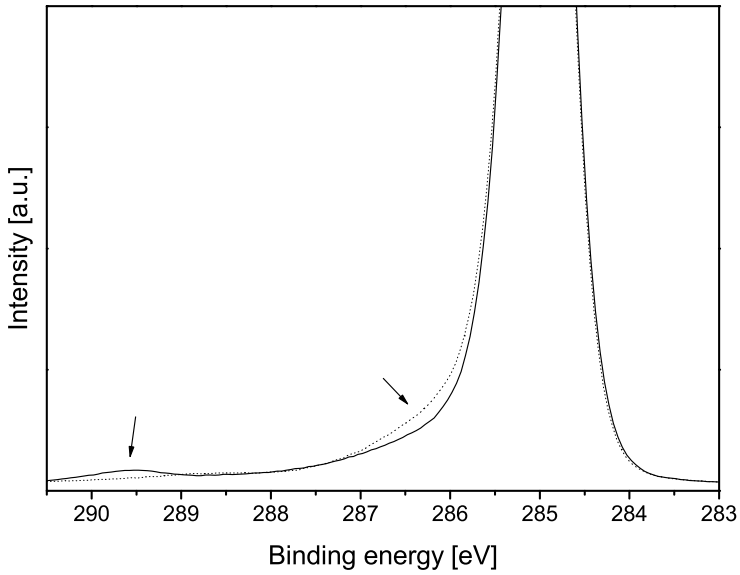

Figure 7.6: Comparison of O-NCDc C1s core level after oxidation (solid line) and after one step treatment (dot line).

the diamond surfaces. This finding is very important because only the NH_2 groups preserve the diamond surface conductivity which is important for devices applications.

The same result is also confirmed by the increase of the area of the C^{III} in the C1s core level. In fig. 7.6 an example of the C1s core level XPS spectra plasma oxidized sample, before and after the one step process are compared. In particular after amination the spectral intensity of the C1s slightly increases in the region overlapped to the CH_x region. For all the samples, the peak fitting shows that the increase of spectral power of the C^{III} component corresponds to the amount of NH_2 groups induced on the diamond surfaces. In addition the presence of amine groups on the diamond surface is always related to a decrease of the oxygen abundance. In particular, after the amination, a reduction of C^{VI} component in the C1s and of the correspondent oxygen component at $\sim$ 533 eV are found. This is a clear indication that oxygen-carbon chemical bonds at the diamond surface are modified.

Although the role of oxygen in the amination process remain still unclear, our data show that there is a correlation between the presence of oxygen and NH_2 grafting. In this regard, it is important to note that samples with highest oxygen abundance present the highest NH_2 concentration after amination. This occurs for the plasma and the piranha treated samples, which have an initial 7.27 % and 7.82 % O atom. conc. and a 2.49 % and 2.67 % of N atom.conc. after amination respectively (see

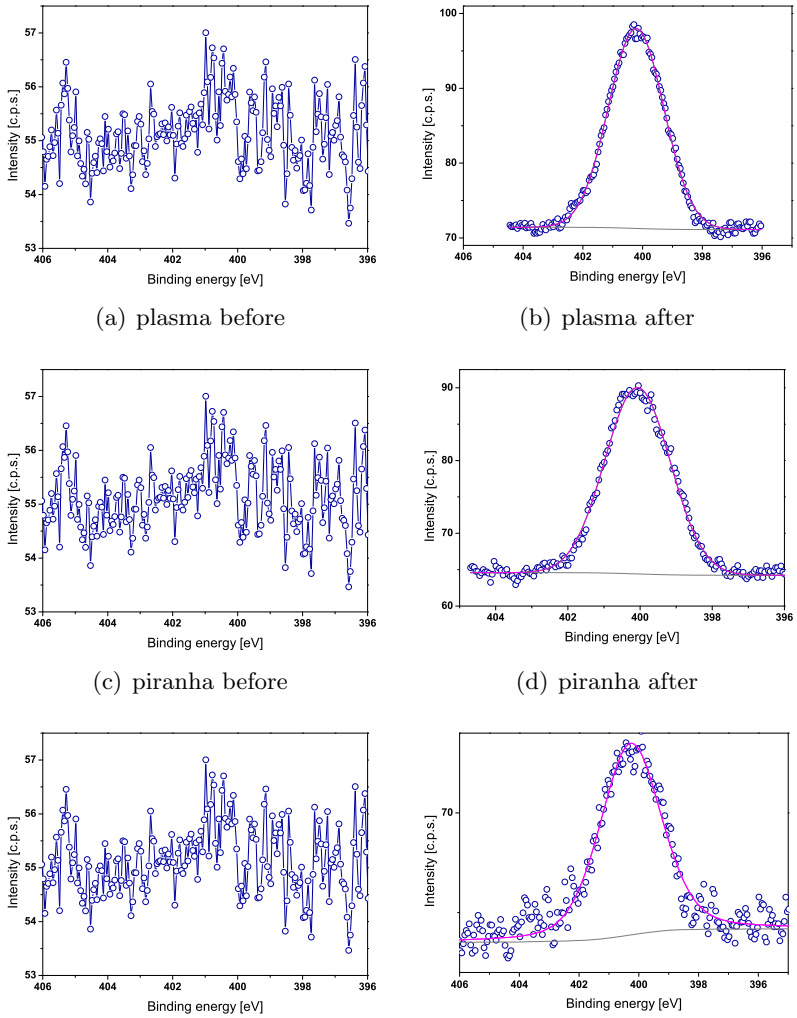

(a) plasma before (b) plasma after

(c) piranha before (d) piranha after

(e) UV-O before (f) UV-O after

Figure 7.7: XPS spectra of the N1s core line of the O-NCD sample acquired befor and after the tratment.

table 7.2).

7.3 Conclusion

In the fig. 7.8 all the results are summarized. We can see that nitrogen is present on the diamond surface only when also oxygen is present. So we can affirm that

the amount of amino groups found on the diamond surface is strictly correlated with the amount of oxygen revealed on the diamond surface after the treatment and experimental results show that oxygen not only in gaseous phase but also bonded to the diamond surface *catalyzes* the NH_2 grafting.

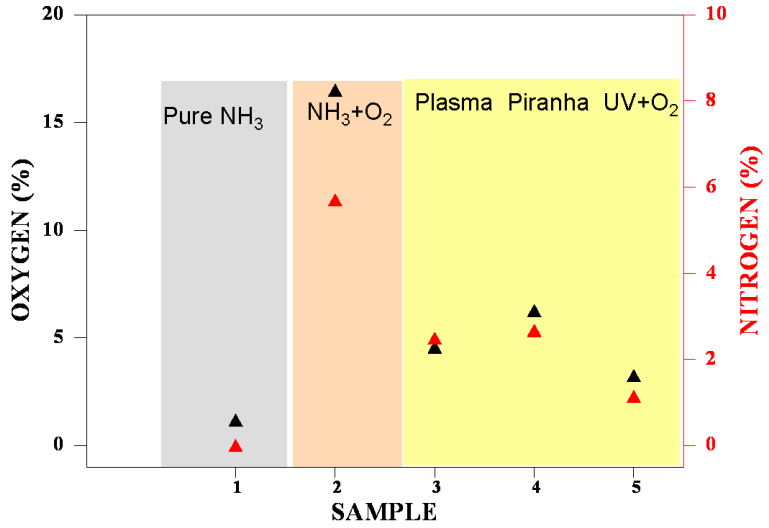

Figure 7.8: Nitrogen and oxygen concentration, checked after amination process, present on the all diamond surface considered in this chapter.

Future investigations are necessary to elucidate the role of the oxygen in the chemical process that occurs on the hydrogenated diamond surface.

Chapter 8

DNA adhesion on functionalized diamond surfaces

In this chapter the passivation of aminated diamond surface is presented. After that the experiment in which DNA was attached to diamond surface is described with both the confocal and XPS analisys.

8.1 Preparation of Diamond surfaces for DNA grafting

The DNA segments carry a high amount of electric charge. For this reason the direct interaction between DNA strands and aminated diamond surface leads to the denaturation of the chains. This prevents any process of hybridization with the appropriate counterparts and the fabrication of the biosensor. In this respect a correct orientation of the ligand molecules on the surface using a spacer arm as shown in figure 8.1 is crucial to make the ligand available for the target.

In the case of diamond, the spacing between the diamond surface and DNA segments is obtained using a special crosslinker like glutaraldehyde.

Among the many available protein crosslinking agents, glutaraldehyde has undoubtedly found the widest application in various fields such as histochemistry , microscopy, cytochemistry, leather tanning industry, enzyme technology, chemical sterilization, and biomedical and pharmaceutical sciences. Glutaraldehyde, a linear 5-carbon dialdehyde, is a clear, colorless to pale straw-colored, pungent oily liquid that is soluble in all proportions in water and alcohol, as well as in organic solvents. It is mainly available as acidic aqueous solutions (pH 3.0 - 4.0), rangcomplexity of its behavior in aqueous to 70 % (w/v). Glutaraldehyde has had great success because of its commercial availability and low cost in addition to its high reactivity. It reacts rapidly with amine groups at around neutral pH and is more efficient than other aldehydes in generating thermally and chemically stable crosslinks [155]. In fact,

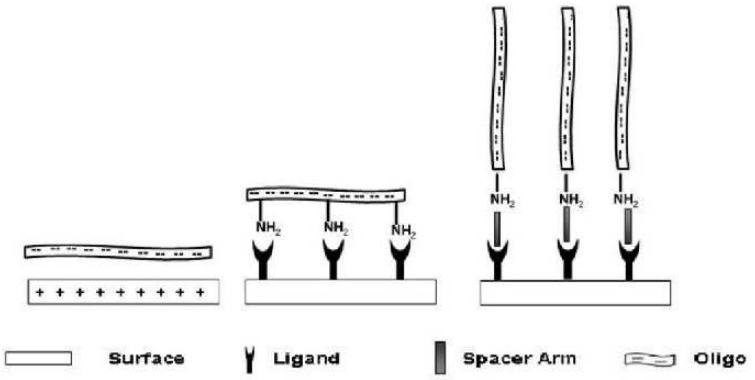

Figure 8.1: Three different schemes of the possible interactions of DNA on the diamond surface are possible: a) electrostatic interaction, that happens when the hydrogenated diamond surface is not properly functionalised; b) the interactiont of the DNA, when ammino groups are present but the surface passivation is not performed; c) the perfect interaction of DNA with surface species.

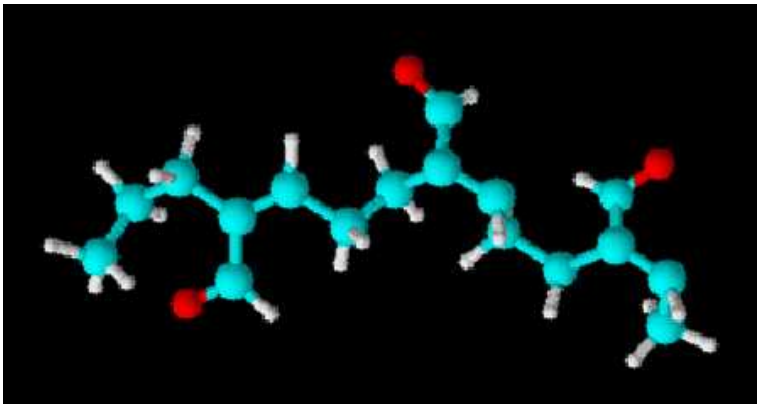

Figure 8.2: 3D scheme of glutaraldehyde.

studies of collagen crosslinking reactions with monoaldehyde (formaldehyde) and dialdehydes having chain lengths of two to six carbon atoms (glyoxal, malonaldehyde, succinaldehyde, glutaraldehyde, and adipaldehyde) demonstrated that the reactivity of this series is maximized with five carbon monomers; thus glutaraldehyde is the most effective crosslinking agent [156].

The glutaraldehyde (GDA) is defined *amine-amine cross linker* because its structure allows to induce bonds between the amine groups present on the solid substrate and the amino groups present in the biomolecuses of interest. The cross-linking

reaction can be carried out using an aqueous (GDA) solution at room temperature.

The fig. 8.3 shows which reactions are involved in the formation of the diamond glutaraldehyde DNA crosslinking.

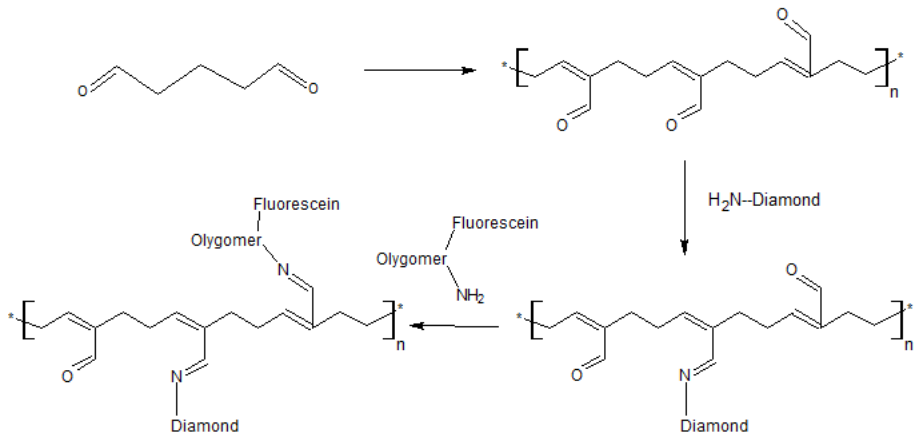

Figure 8.3: Reaction scheme of the diamond glutaraldehyde DNA crosslinking

8.2 Caracterisation DNA adhesion on functionalized diamond surfaces

In view of the fabrication of a biosensor essential is to verify the ability to bond DNA to the diamond sensing area. At this aim the differently aminated NCD surfaces discussed in section 7 were compared with respect to their ability to couple to the crosslinker needed to attach the oligonucleotides.

The diamond surfaces were functionalized accordingly to the method described by Zhang et al.. Briefly, the substrates were incubated with a 1 % glutaraldehyde (G5882, Sigma) solution in MilliQ water at room temperature for 1 hour and then washed three times with ultrapure water.

A 15 mer-oligonucleotides (20 μM in 3 x SSC buffer (S6639, Sigma)) were then immobilized on the surface at 38 ℃ for 2 hours, using a silicone frame to confine the treatment in a central region of the sample. The oligonucleotide sequence, 5'-NH_2-(CH2)6-GGT TGG TGT GGT TGG-fluorescein-3' (IDT DNA Technologies), carries an amino group at one end and a fluorescein molecule at the other end. With these terminations, the DNA single strands should bond to the glutaraldehyde through the amino groups while the fluorescent markers will indicate the presence of DNA and its localization. After incubation the substrates were rinsed once with washing buffer (phosphate buffer 0.1 M, 0.1 % Tween 20, pH 7.5), once with simple phosphate buffer and once with ultrapure water.

The substrates were then analysed using a confocal microscope (Leica TCS SP5 II) equipped with an argon laser and using a 20 x objective. Images were acquired on the edge of the area functionalized with the oligonucleotides. Due to the absence of labelled DNA outside the treated zone, differences in the fluorescence intensity should be revealed if the coupling process is effective.

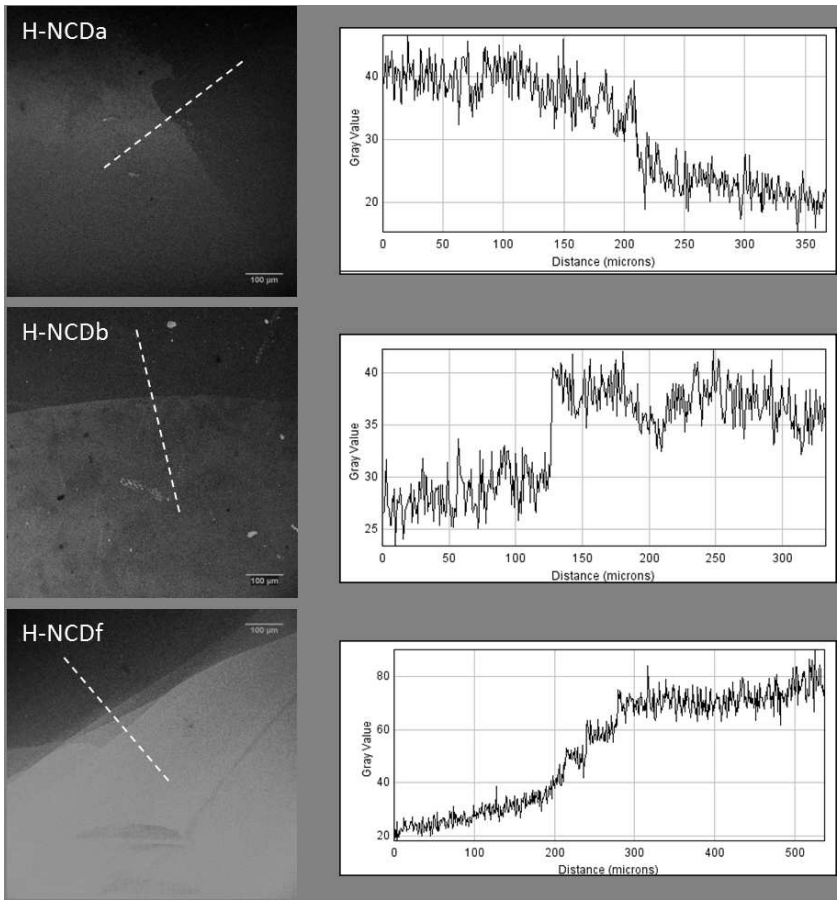

Figure 8.4: Example of fluorescence from DNA functionalized diamond samples H-NCDa, H-NCDb and H-NCDf. The profile of the fluorescence intensity was acquired on the on the edge of the treated areas as indicated by the dashed lines.

In fig. 8.4 are reported the fluorescence edge profiles for hydrogenated samples H-NCDa (functionalized using NH_3 plus UV), H-NCDb (functionalised by NH_3 plus O_2 and UV) and H-NCDf. (sample as received). For comparison in fig. 8.5 the same analysis is shown for samples O-NCDc, O-NCDd and O-NCDe which were aminated

starting from an oxidized diamond surface by plasma, piranha and UV irradiation respectively.

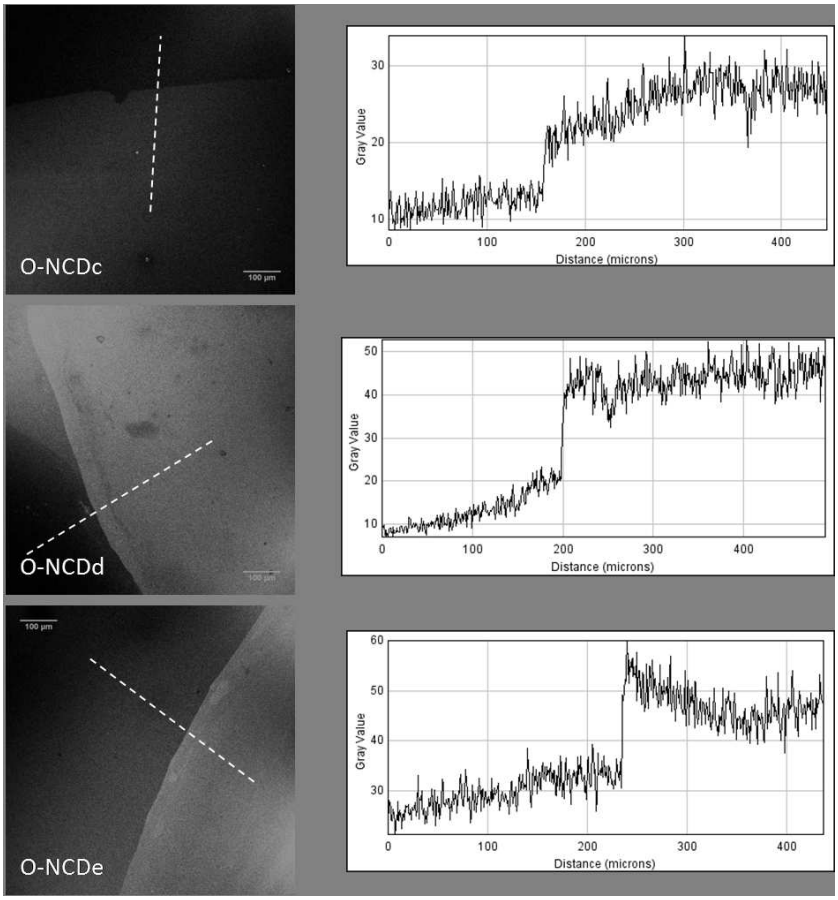

Figure 8.5: Example of fluorescence from DNA functionalized diamond samples O-NCDc, O-NCDd and O-NCDe. The profile of the fluorescence intensity was acquired on the on the edge of the treated areas as indicated by the dashed lines.

Figure 8.6 summarizes the results of the confocal microscope analysis. The mean fluorescence intensity measured for each of the six analyzed samples is here shown. It appears that the sample H-NCDf exhibits the higher fluorescence, i.e. the higher concentration of DNA attached on its surface. At a first glance, this is in complete contradiction with what one should expect. In fact, sample H-NCDf corresponds to the simple hydrogenated surface. These results indicate that the adhesion of DNA strands on hydrogenated NCD is very effective and no surface functionalization

seems to be needed. This is, on the other hand, a not correct conclusion as we will demonstrate later on.

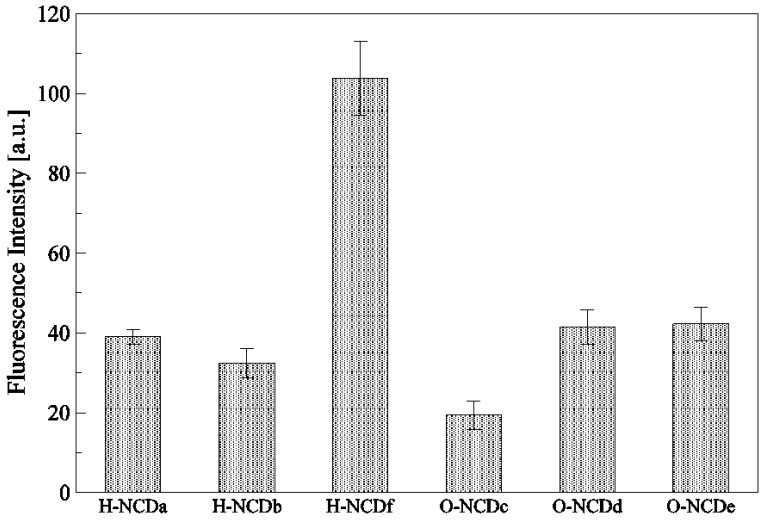

Figure 8.6: Fluorescence intensity of the six diamond samples. Images are acquired with a 20 x objective. The bars represent a mean of five values and the relative standard deviation is reported.

These experimental evidences may be explained considering the high electrostatic negative charges present on the DNA strands due to the phosphate groups on the deoxyribose backbone. These groups may easily interact with the slightly positive hydrogenated NCD surface. Unfortunately this coupling cannot be used to attach DNA on diamond. The interaction is so strong that the oligonucleotides loose their conformation and their power to hybridize with their counterparts. This is the reason to use glutaraldehyde as an intermediate cross linker to bond DNA on NCD avoiding non-specific interactions and denaturation.

To correctly evaluate the efficacy of the NCD functionalization with DNA, oligonucleotides adsorbed with non-specific couplings must be removed. At this aim a strong washing treatments were done at high pH. Accordingly to Zhang [150], the surfaces were immersed in a NaOH 0.2 M solution with 0.1 % SDS (SodiumDodecylSulfate, Pierce) for 20 minutes in orbital shaking. The samples were then washed with SSC 2x and water, and analysed with the confocal microscope. A background signal was subtracted from the fluorescence values recorded on the six NCD samples. The results are shown in figure 8.7.

After removal of the non-specific DNA strands, the fluorescence from the simple hydrogenated H-NCDf sample is completely eliminated. Different is the situation for

the other sample. Now the fluorescence observed derives exclusively from oligonucleotides immobilized on surface with a specific bond. Surprisingly figure 8.7 put forward that oligonucleotides bond more efficiently to the NCD samples which were aminated in an ammonia atmosphere using UV irradiation. This could derive from a better interaction of glutaraldehyde with the UV-aminated surfaces. Lower density of DNA strands seems to be present in the case of amination induced on oxidized NCD surfaces. This could be explained by a lower interaction of glutaraldehyde with the NCD caused by the presence of a high amount of oxygen making the bonds with the surface more difficult.

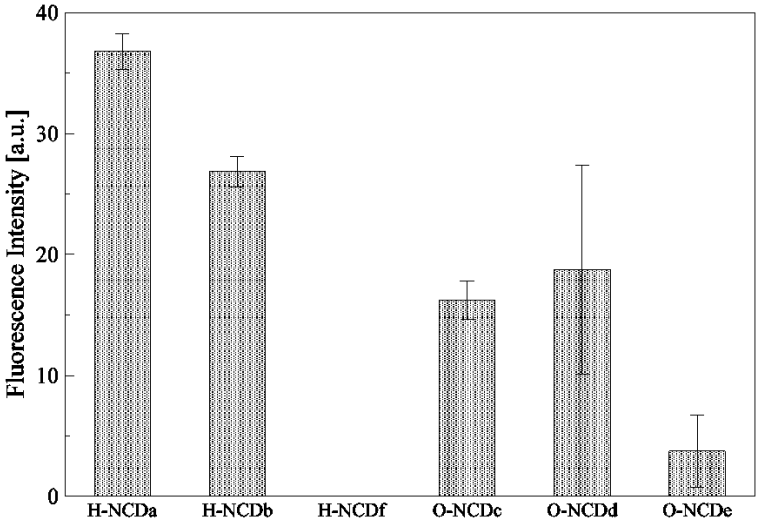

Figure 8.7: Fluorescence intensity from the sic NCD samples after elimination of non-specific adsorbed DNA. Images acquired with a 20 x objective. The bars represent a mean of five values and the relative standard deviation is reported.

The fluorescence intensity from the six NCD samples was correlated with the trend of nitrogen and phosphorus detected by XPS. Both these elements are, in fact, part of the DNA chains: nitrogen is present in all the four bases, Adenine, Guanine, Cytosine and Thymine. Phosphorus is present in the Phosphate Deoxyribose backbone. It turns out that the concentrations of both nitrogen and phosphorus should follow that of the fluorescence intensity. Nitrogen and phosphorus spectral intensities I(N) and I(P) measured on the six functionalized diamond surfaces are shown in figure 8.8 A,B. It appears immediately that these two elements exhibit rather different trends. In particular no correlation is observed between I(N) and the trend of the fluorescence while better agreement is present in the case of I(P). This could be explained considering that contribution to nitrogen may derive from the amine

groups induced on the NCD through the amination process. This is confirmed by the low value of I(N) found for the non-aminated H-NCDf sample. Different is the trend of I(P) which is in good agreement with that of the fluorescence. It has to be kept in mind, however, that the amount of DNA left on the NCD surface after the washing treatment is low. In addition also the cross section of phosphorus is low. The detection of this element is then not free of problems and caution has to be used when the spectral intensity of phosphorus is utilized to perform quantifications.

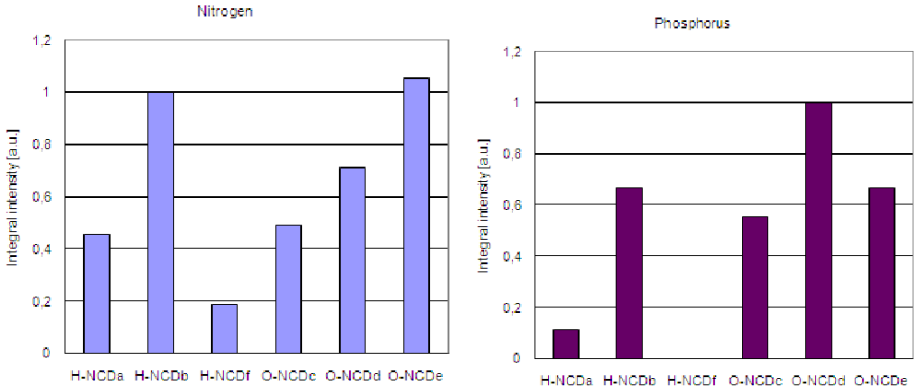

(a) (b)

Figure 8.8: spectral intensity of (A) nitrogen and (B) phosphorus core lines after removal of non-specific DNA strands.

8.2.1 Conclusions

In this experiment hydrogenated/oxidized NCD samples were aminated using different processes. The different surface chemistries were compared in terms of their ability to bond DNA strands. Results indicate that a crosslinker like glutaraldehyde is needed to avoid the formation of non-specific interactions between oligonucleotides and surfaces leading to DNA denaturation. After removal of non-specific DNA strands, the fluorescence images acquired with the confocal microscope show a higher intensity for the samples possessing a good amination. XPS confirms this evidence. The trend of phosphorous used as a DNA marker is in agreement with that of the fluorescence. These outcomes demonstrate the good efficiency of the process of NCD amination. In particular the density and the stability of the amine groups grafted on the NCD surfaces allow specific bonds of DNA mediated by the glutaraldehyde cross linker. In addition, the abundances of the oligonucleotides attached to the NCD surfaces are compatible with those needed to fabricate a NCD based biosensor.

Chapter 9

Conclusions

This work describes a careful characterization of the surface properties of nanocrystalline diamond. In view of biosensing application, the chemical, electronic, and optical properties of this extraordinary material were investigated. The samples here considered are diamond films deposited by chemical vapor deposition. This technique generates thin polycrystalline diamond films, the crystallite size depending on the deposition conditions. Bulk properties were firstly studied. At this aim, optical probes were used. Raman spectroscopy in the UV range demonstrates that the characteristics of the NCD films we dealt with, are dictated by the purity of the crystallites. The inter-grain, non-diamond phase plays a minor role. In this respect, the quality of NCD samples is comparable to that of monocrystalline diamonds. This is confirmed also by m-line analysis which provides the NCD refractive index n. As a matter of fact, n measured at two different wavelengths was very similar to that of monocrystalline diamond. m-line was used also to verify the presence of guiding modes in the NCD films. The optical quality of NCD was verified also measuring their transmittance. Spectra put forward that the effect of scattering by the randomly oriented crystallites, by the surface roughness and by the grain boundaries is non-negligible. The better samples with respect to their bulk optical properties, were selected to study the correlation between electronic and chemical surface characteristics.

The diamond surface is very stable and chemically inert. A general problem related to the development of a biosensor, is the preparation of the device sensing area. UV photons were used to induce an oxygen termination and to graft functional groups. Concerning oxidation, the kind of chemical bonds induced by UV irradiation in air and in pure oxygen atmosphere was studied. We focused on the changes of the electronic properties of diamond induced by oxidation and by oxygen desorption during thermal treatments at increasing temperature.

Experiments demonstrate that UV-induced oxidation is very peculiar. UV and X-

ray photoelectron spectroscopies show a strong reduction of the oxygen concentration with annealing and, at the same time, a corresponding decrease of the electron affinity. A series of six different chemical reactions are hypothesized to explain the recovery of the negative electron affinity that is characteristic of a hydrogenated diamond surface. Interestingly, this effect was observed for the first time.

The process of NCD oxidation was further analyzed. To compare UV-irradiation with other oxidation methods three NCD thin film were oxidized using piranha solution, oxygen plasma and UV photons. Again thermal desorption of oxygen was performed to understand the changes of electron affinity in relation to the different oxidation process used.

XPS shows that different oxidation methods produce different abundances of carbonyl and etherlike bonds. The higher concentration of carbonyl groups found in the case of piranha and plasma oxidized NCD shows detrimental effects towards the recovery of a negative electron affinity. This last is recovered in presence of weaker carbon-oxygen bonds obtained mainly by UV irradiation.

UV photons were used also to verify the possibility to graft amino groups on the diamond surface. Experiments show that UV irradiation in pure NH3 atmosphere is ineffective. We demonstrated that oxygen is needed to obtain good diamond aminations. To understand the role of oxygen, experiments were carried out using hydrogen terminated surfaces and NCD oxidized using three different techniques (oxygen plasma, piranha solution and UV irradiation). Amination was performed in situ irradiating with UV photons both in pure ammonia and in a mixture of pure NH_3 and O_2. Results show that the presence of oxygen either bonded to the NCD surface or in the gas phase, is essential to obtain a NCD amination. In agreement with literature, we demonstrated that an efficient one step amination of hydrogenated diamond surfaces requires the presence of an electron negative element which in this case is oxygen.

To conclude our investigation, the different surface chemistries were compared in terms of their ability to bond DNA strands. Experiments were performed bonding oligonucleotides directly to hydrogenated diamond surfaces. The fluorescence intensity reveals a high abundance of DNA fixed to H-NCD. Unfortunately this fluorescence disappears when surfaces are washed to remove all the DNA strands attached with non-specific interactions. This put forward the need of a cross-linker to avoid non-specific interactions which cause oligonucleotide denaturation. Good amination of NCD surfaces led to a good interfacing with glutaraldehyde. Optical confocal microscopy demonstrates that the presence of this cross-linker induced specific bonding of DNA to NCD surfaces. The fluorescence intensity obtained from NCD possessing different degree of amination is in agreement with the trend of phosphorus from XPS analyses.

Bibliography

[1] J. E. Field. *The Properties of Natural and Synthetic.* Diamond. Academic Press, London, 1992.

[2] J. C. Angus. *Structure and thermochemistry of diamond.* Proceedings of the International School of Physics Enrico Fermi, Course CXXXV, The physics of diamond, edited by A. Paoletti and A. Tucciarone, Societ‘ Italiana di Fisica, 1997.

[3] J. Ristein, F. Maier, M. Riedel, M. Stammer, and L. Ley. *Diam. Relat. Mater.*, 10:416, 2001.

[4] E. Kohn and C. Manfredotti. *Adv. Sci. and Technol.*, 48:151, 2006.

[5] J. S. Foord, L. C. Hian, and R. B. Jackman. *Diam. Relat. Mater.*, 10:710, 2001.

[6] H. Notsu, I. Yagi, T. Tatsuma, D. A. Tryk, and A. Fujishima. *J. Electroanal. Chem.*, 492:31, 2000.

[7] J. Shirafuji and T. Sugino. *Diam. Relat. Mater.*, 5:706, 1996.

[8] J. S. Foord, C. H. Lau, M. Hiramatsu, R. B. Jackman, C. E. Nebel, and P. Bergonzo. *Diam. Relat. Mater.*, 11:856, 2002.

[9] T. Yamada, T. Yokotama, and A. Sawabe. *Diam. Relat. Mater.*, 11:780, 2002.

[10] J. I. B. Wilson, J. S. Walton, and G. Beamson. *J. Electron. Spectrosc. Relat. Phenom.*, 121:183, 2001.

[11] C. Saby and P. Muret. *Diam. Relat. Mater.*, 11:851, 2002.

[12] J. Ristein. *Surf. Sci.*, 600:3677, 2006.

[13] T. Ando, K. Yamamoto, M. Ishii, M. Kamo, and Y. Sato. *J. Chem. Soc. Faraday Trans.*, 89:3635, 1993.

[14] P. E. Pehrsson and T. W. Mercer. *Surf. Sci.*, 460:49, 2000.

[15] H. Notsu, I. Yagi, T. Tatsuma, D. A. Tryk, and A. Fujiwara. *Electrochem. Solid State Lett.*, 2:522, 1999.

[16] I. Yagi, H. Notsu, T. Kondo, D. A. Tryk, and A. Fujishima. *J. Electroanal. Chem.*, 473:173, 1999.

[17] C. H. Goeting, F. Marken, A. Gutierrez-Sosa, and R. C. Compton. *Diam. Relat. Mater.*, 9:390, 2000.

[18] H. Notsu, T. Fukazawa, T. Tatsuma, D. A. Tryk, and Y. Fujiwara. *Electrochem. Solid-State Lett.*, 4:H1, 2001.

[19] D. Dalabouglise, B. Marcus, M. Mermoux, P. Bouvier, J. Chane-Tune, J. P. Petit, P. Mailley, and T. Livache. *Chem. Commun.*, page 2698, 2003.

[20] H. Kanazawa, K. S. Song, T. Sakai, Y. Nakamura, H. Umezawa, M. Tachiki, and H. Kawarada. *Diam. Relat. Mater.*, 12:618, 2003.

[21] M. Riedel, J. Riestein, and L. Ley. *Diam. Relat. Mater.*, 13:746, 2004.

[22] L. Tang, C. Tsai, W. W. Gerberic, L. Kruckeberg, and D. R. Kania. *Biomaterials*, 16:483, 1995.

[23] K. Takahashi, M. Tanga, O. Takai, and H. Okamura. *Bio Ind.*, 17:44, 2000.

[24] W. Yang and al. *Nature Mater.*, 1:253, 2002.

[25] J. Wang, M. A. Firestone, O. Auciello, and J. A. Carlisle. *Langmuir*, 20:11450, 2004.

[26] G. J. Zhang, K. S. Song, Y. Nakamura, T. Ueno, T. Funatsu, I. Ohdomari, and H. Kawarada. *Langmuir*, 22:3728, 2006.

[27] H. Umezawa, K. Tsugawa, S. Yamanaka, D. Takeuchi, H. Okushi, and H. Kawarada. *Jpn. J. Appl. Phys.*, 38:L1222, 1999.

[28] T. Sakai, K. S. Song, H. Kanazawa, Y. Nakamura, H. Umezawa, M. Tachiki, and H. Kawarada. *Diam. Relat. Mater.*, 12:1971, 2003.

[29] J. Fritz, E. B. Cooper, S. Gaudet, P. K. Sorger, and S. R. Manalis. *Proc. Natl. Acad. Sci. U.S.A.*, 99:14142, 2002.

[30] G. Zeck and P. Fromhertz. *Proc. Natl. Acad. Sci. U.S.A.*, 98:10457, 2001.

[31] J.A. Carlisle. *Nature Mater.*, 10:668, 2004.

[32] H. Okamura, H. Yamano, and M. Tanga. *Mater. Technol.*, 22:173, 2004.

[33] W.H. Chen, S.C. Lee, S. Sabu, H.C. Fang, S.C. Chung, C.C. Han, and H.C. Chang. *Anal. Chem.*, 78:4228, 2006.

[34] A. Hartl and al. *Nature Mater.*, 3:736, 2004.

[35] K. F. Chong and al. *Langmuir*, 23:5615, 2007.

[36] T. Kondo, K. Honda, Y. Einaga, D. A. Tryk, and A. Fujishima. *Diam. Electrochem.*, 149, 2005.

[37] G.M. Swain. *Semicond. Semimet.*, 77:121, 2004.

[38] S. H. P. Serrano, R. C. Mendes de Barros, J. M. S. da Silva, and P. Favero. *Reisdorfer. Electroanalyt. Asp. Biol. Signif. Comp.*, 51, 2006.

[39] A. Broz, V. Baresova, A. Kromka, B. Rezek, and M. Kalbacova. *Phys. Status Solid A*, 9:2038, 2009.

[40] F. R. Kloss, M. Najam-Ul-Haq, M. Rainer, R. Gassner, G. Lepperdinger, W. C. Huck, G. Bonn, F. Klauser, X. Liu, N. Memmel, E. Bertel, J. A. Garrido, and D. Steinmueller-Nethl. *Journal of Nanoscience and Nanotechnology*, 7:4581, 2007.

[41] W. Kaiser and W. L. Bond. *Phys. Rev.*, 115:857, 1959.

[42] C. Kittel. *Introduzione alla fisica dello stato solido.* Boringhieri, 1971.

[43] G. S. Painter, D. E. Ellis, and A. R. Lubinsky. *Phys. Rev. B*, 4:3610, 1971.

[44] J. Schafer, J. Ristein, R. Graupner, L. Ley, and al. *Phys. Rev. B*, 53:7762, 1996.

[45] O. I. Leipunskii. Usp. Khim, 1939.

[46] H. Liu and D. S. Dandy. *Diamond chemical vapor deposition: nucleation and early growth stages.* Noyers Publications, 1995.

[47] K. Nassau. *Synthesis of bulk diamond: history and present status.* Noyes Publications, 1993.

[48] J.C. Angus, H. A. Will, and W. S. Stanko. *J. Appl. Phys.*, 39:2915, 1968.

[49] W. G. Eversole. Can. patent no. 628, 567, 112, 1959.

[50] B. V. Derjaguin and B. V. Splitsyn. Ussr authors' certificate no. 399,134; 1980. urrs patent no. 399,134.

[51] P. W. May. *Phil. Trans. R. Soc. Lond. A*, 358:473, 2000.

[52] S. Bhattacharyya, O. Auciello, J. Birrell, J. A. Carlisle, L. A. Curtiss, A. N. Goyette, D. M. Gruen, A. R. Krauss, J. Schlueter, A. Sumant, and P. Zapol. *Appl. Phys. Lett.*, 79:1441, 2001.

[53] C. Wild, P. Koidl, W. Müller-Sebert, H. Walcher, R. Kohl, N. Herres, R. Locher, R. Samlenski, and R. Brenn. *Diam. Relat. Mater.*, 2:158, 1993.

[54] C. Wild, R. Kohl, N. Herres, W. Müller-Sebert, and P. Koidl. *Diam. Relat. Mater.*, 3:373, 1994.

[55] G. Kern, J. Hafner, J. Furthmüller, and G. Kresse. *Surf. Sci.*, 745:352, 1996.

[56] R. Graupner and al. *Phys. Rev. B*, 55:10841, 1997.

[57] R. Graupner and al. *Phys. Rev. B*, 60:18023, 1999.

[58] K. C. Pandey. *Phys. Rev. Lett.*, 47:1913, 1981.

[59] X. M. Zheng and P. V. Smith. *Surf. Sci.*, 262:219, 1992.

[60] Loh K. P., Xie X. N., Yang S. W., and Pan J. S. Wu P. *Diam. Rel. Mater.*, 11:1379, 2002.

[61] Frauenheim et all. *Phys. Rev. B*, 48:18189, 1993.

[62] Z. Jing and Whitten J. L. *Surf. Sci.*, 314:300, 1994.

[63] L. Ostrovskaya, V. Perevertailo, V. Ralchenko, A. Dementjev, and O. Loginova. *Diam. Relat. Mater*, 11:845, 2002.

[64] B. B. Pate. *Surf. Sci.*, 83:165, 1986.

[65] F.J. Himpsel, J. A. Knapp, J. A. Van Vechten, and A. E. Eastman. *Phys. Rev. B*, 20:624, 1979.

[66] J. Van der Weide, Z. Zhang, P. K. Baumann, M. G. Wensell, J. Bernholc, and R. J. Nemanich. *Phys. Rev. B*, 50:5803, 1994.

[67] F. Maier, J. Ristein, and L. Ley. *Phys. Rev. B*, 64:165411, 2001.

[68] F. Maier, M. Riedel, B. Mantel, J. Ristein, and L. Ley. *Phys. Rev. Lett.*, 85:3472, 2000.

[69] N. B. Hanney and C. P. Smith. *J. Am. Chem. Soc.*, 68:171, 1946.

[70] J. B. Cui, J. Ristein, and L. Ley. *Phys. Rev. B*, 59:5847, 1999.

[71] J. Topping. *Proc. R. Soc. London A*, 114:67, 1927.

[72] M. I. Landstrass and K. V. Ravi. *Appl. Phys. Lett.*, 55:975, 1989.

[73] T. Maki, S. Shikama, M. Komori, Y. Sakuta, and T. Kobayashi. *Jpn. J. Appl. Phys.*, 31:1446, 1992.

[74] T. Sugino, Y. Sakamoto, A. Furuya, and J. Shirafuji. *Mater. Res. Soc. Symp. Proc.*, 339:45, 1994.

[75] K. Hayashi, S. Yamanaka, H. Okushi, and K. Kajimura. *Appl. Phys. Lett.*, 68:376, 1996.

[76] S. Albin and L. Watkins. *Appl. Phys. Lett.*, 56:1454, 1990.

[77] A. Denisenko and al. *Diam. Relat. Mater.*, 9:1138, 2000.

[78] D. Shin, H. Watanable, and C. E. Nebel. *Diam. Relat. Mater.*, 15:121, 2006.

[79] W. E. Spicer. *Phys. Rev.*, 112:114, 1958.

[80] C. N. Berglund and W. E. Spicer. *Phys. Rev.*, 136:A1030, 1964.

[81] G. D. Mahan. *Phys. Rev. B*, 2:4334, 1970.

[82] L. D. Landau and M. I. Lisfitz. *Quantum Mechanics: Non-Relativistic Theory.* 3rd Edition Pergamon Press, Oxford, 1977.

[83] L. H. Thomas. *Proc. Cambridge Philos. Soc.*, 23:542, 1927.

[84] E. Fermi. *Z. Phys.*, 48:73, 1928.

[85] M. Anderle and M. G. Cattania. *Metodi per la Caratterizzazione Chimico-Fisica delle Superfici.* Patron ed. Bologna, Italia, 1991.

[86] C. J. Powell and al. *J. Elect. Spectrosc.*, 1:98, 1999.

[87] S. Tanuma and al. *Surf. Interface Anal.*, 17:911, 1991.

[88] D. Briggs and J. T. Grant. *Surface Analysis by Auger and X-Ray Photoelectron Spectroscopy.* IM Publications and Surface Spectra Limited, 2003.

[89] G. Beamson and D. Briggs. *High Resolution XPS of Organic Polymers.* Joh Wiley and Sons, Chichester, 1992.

[90] K. Siegbahn and al. *ESCA Applied to Free Molecules.* North Holland, Amsterdam, 1969.

[91] D. A. Shirley and al. *Phys. Rev. B*, 5:4709, 1972.

[92] S. Tougaard and al. *Phys. Rev. B*, 25:4452, 1981.

[93] S. Tougaard and al. *Solid State Commun.*, 61:547, 1987.

[94] T. A. Carlson. *Photoelectron and Auger Spectroscopy.* Plenum, New York, 1976.

[95] Y. Park, V. Choong, Y. Gao, B. R. Hsieh, and W. C. Tang. *Appl. Phys. Lett.*, 68:2699, 1996.

[96] L. Ostrovskayaa and al. *Diam. Relat. Mater.*, 11:845, 2002.

[97] Y. Kaibara and al. *Diam. Relat. Mater.*, 12:560, 2003.

[98] C. V. Raman. On the molecular scattering of light in water and the colour of the sea. *Proc. Royal Soc. London A*, 11(708):64, 1922.

[99] C. V. Raman and K. S. Krishnan. A new type of secondary radiation. *Nature*, 121(3048):501, 1928.

[100] C. V. Raman. The molecular scattering of light. In *Nobel Lectures, Physics 1922-1941*, page 267. Elsevier, 1965.

[101] A. Smekal. Zur quantentheorie der dispersion. *Naturwissenschaften*, 11:873, 1923.

[102] D. A. Long. *The Raman Effect.* John Wiley & Sons, West Sussex, England, 2002.

[103] W. H. Weber and R. Merlin. *Raman scattering in material science*, volume 42 of *Material Science.* Springer-Verlag, Berlin, Heidelberg, New york, 2000.

[104] M. H. Brodsky, E. Burstein, M. Cardona, L. M. Falicov, M. V. Klein, R. M. Martin, A. Pinczuk, A. S. Pine, and Y.-R. Shen. *Light Scattering in Solids I*, volume 8 of *Topics in Applied Physics.* Springer-Verlag, Berlin, Heidelberg, New York, 1983.

[105] P. K. Tien and R. Ulrich. *Journal of the Optical Society of America*, 60:1325, 1970.

[106] V. Ralchenko, I. Sychov, I. Vlasov, A. Vlasov, V. Konov, A. Khomich, and S. Voronina. *Diam Relat. Mater.*, 8:189, 1999.

[107] K. Janischowsky and al. *Diam. Relat. Mater.*, 12:336, 2003.

[108] T. Zimmermann and al. *Diam. Relat. Mater.*, 15:203, 2006.

[109] M. Yoshikawa, G. Katagiri, H. Ishida, A. Ishitani, M. Ono, and K. Matsumura. *Appl. Phys. Lett.*, 55:2608, 1989.

[110] C. Casiraghi, F. Piazza, A. C. Ferrari, D. Grambole, and J. Robertson. *Diam. Relat. Mater*, 14:1098, 2005.

[111] W. R. Bormett, S. A. Asher, R. E. Witowski, W. D. Partlow, and R. Pettit F. Lizewski. *J. Appl. Phys.*, 77:5916, 1995.

[112] P. K. Tien, R. Ulrich, and J. R. Martin. *Appl. Phys. Lett.*, 14:291, 1969.

[113] A. M. Zaitsev. *Optical properties of diamond a Data Handbook*. Springer, 2000.

[114] T. Sharda, T. Soga, and T. Jimbo. *Diam. Relat. Mater.*, 10:561, 2001.

[115] T. Soga, T. Sharda, and T. Jimbo. *Phys. Solid State*, 46:720, 2004.

[116] D. S. Knight and W. B. White. *J. Mater. Res.*, 4:385, 1989.

[117] B. Marcus, L. Fayette, M. Mermoux, L. Abello, and G. Lucazeau. *J. Appl. Phys.*, 76:3463, 1994.

[118] S. Piscanec, M. Lazzeri, F. Mauri, A. C. Ferrari, and J. Robertson. *Phys. Rev. Lett.*, 93:185503, 2004.

[119] A. C. Ferrari and J. Robertson. *Phys. Rev. B*, 61:14095, 2000.

[120] S. M. Huang, Z. Sun, Y. F. Lu, and M. H. Hong. *Surf. Coat. Technol.*, 151-152:263, 2002.

[121] A. C. Ferrari and al. *Phil. Trans. R. Soc. Lond. A*, 362:2477, 2004.

[122] M. Riedel and al. *Phys. Rev. B*, 69:125338, 2004.

[123] C. E. Nebel, H. Kato, B. Rezek, D. Shin, D. Takeuchi, H. Watanabe, and T. Yamamoto. *Diam. Relat. Mater.*, 15:264, 2006.

[124] G. Speranza, L. Minati, and M. Anderle. *J. Phys. Chem. A*, 110:13857, 2006.

[125] R. G. Parr and R. G. Pearson. *J. Phys. Chem. Soc.*, 105:7512, 1983.

[126] L. Diederich, O. M. Kuttel, E. Schaller, and L. Schlapbach. *Surf. Sci.*, 349:176, 1996.

[127] G. Francz and P. Oelhafen. *Diam. Relat. Mater.*, 4:539, 1995.

[128] C. Bandis and B. B. Pate. *Phys. Rev. B*, 52:12056, 1995.

[129] S. Torrengo, L. Minati, M. Filippi, A. Miotello, M. Ferarri, A. Chiasera, E. Vittone, A. Pasquarelli, M. Dipalo, E. Kohn, and G. Speranza. *Diam. Relat. Mater.*, 18:804, 2009.

[130] J. C. Zheng, X. N. Xie, A. T. S. Wee, and K. P. Loh. *Diam. Relat. Mater.*, 10:500, 2001.

[131] K. Bobrov, H. Shechter, A. Hoffman, and M. Folman. *Appl. Surf. Sci.*, page 196, 2001.

[132] D. Petrini and A. Larsson. *J. Phys. Chem. C*, 111:795, 2007.

[133] R. Müller, A. Denisenko, and E. Kohn. *Diam. Relat. Mater.*, 12:554, 2003.

[134] O. A. Williams, M. D. Whitfield, R. B. Jackman, J. S. Food, J. E. Butler, and C. E. Nebel. *Diam. Relat. Mater.*, 10:423, 2001.

[135] T. Zimmerman, M. Kubovich, A. Denisenko, K. Janischowsky, O. A. Williams, D. M. Gruen, and E. Kohn. *Diam. Relat. Mater.*, 14:416, 2005.

[136] P. Reinke and P. Oelhafen. *Phys. Rev. B*, 60:15772, 1999.

[137] R. Müller, A. Denisenko, M. Adamschilk, and E. Kohn. *Diam. Relat. Mater.*, 11:651, 2002.

[138] G. Speranza, S. Torrengo, M. Filippi, L. Minati, E. Vittone, A. Pasquarelli, M. Dipalo, and E. Kohn. *Surf. Sci.*, 604:753, 2010.

[139] F. Klauser, S. Ghodbane, R. Boukherroub, S. Szunerits, D. Steinmller-Nethl, E. Bertel, and N. Memme. *Diam. Relat. Mater.*, 19:474, 2010.

[140] C. Pietzka, A. Denisenko, A. Romanyuk, P. J. Schäfer, L. A. Kibler, J. Scharpf, and E. Kohn. *Diam. Relat. Mater.*, 19:213, 2010.

[141] M. Dipalo, C. Pietzka, A. Denisenko, H. El-Hajj, and E. Kohn. *Diam. Relat. Mater.*, 17:1241, 2008.

[142] A. Denisenko, C. Pietzka, A. Romanyuk, H. El-Hajj, and E. Kohn. *J. Appl. Phys.*, 103:014904, 2008.

[143] S. Szunerits and R. Boukherroub. *J. Solid State Electrochem*, 12:1205, 2008.

[144] B. Sun, S. E. Baker, J. E. Butler, H. Kim, J. N. Russell, L. Shang, K-Y tse, and R. yang, W. Hamers. *Diam. Relat. Mater.*, 16:1608, 2007.

[145] T. C. Kuo, R. L. McCreery, and G. M. Swain. *Electrochem. Solid State Lett.*, 2:288, 1999.

[146] P. Allongue, M. Delamar, B. Desbat, O. Fagebaume, R. Hitmi, J. Pinson, and J. M. Savéant. *J. Am. Chem. Soc.*, 119, 1997.

[147] J. B. Miller and D. W. Brown. *Langmuir*, 12:5809, 1996.

[148] T. Ando, R. E. Rawles, K. Yamamoto, M. Kamo, Y. Sato, and M. Nishitani-Gamo. *Diam. Relat. Mater.*, 5:1136, 1996.

[149] K. I. Sotowa, T. Amamoto, A. Sobana, K. Kusakabe, and T. Imato. *Diam. Relat. Mater.*, 13:145, 2004.

[150] G. J. Zhang, K. S. Song, Y. Nakamura, T. Ueno, T. Funatsu, I. Ohdomari, and H. Kawarada. *Langmuir*, 22:3728, 2006.

[151] J. H. Yan, K. S. Song, G. J. Zhang, M. Degawa, Y. Sasaki, I. Ohdomari, and H. Kawarada. *Langmuir*, 22:11245, 2006.

[152] F. Arefi-Khononsare, J. Kurdi, M. Tatoulian, and J. Amouroux. *Surf. Coat. Technol.*, 142-144:347, 2001.

[153] K. S. Soup, G. J. Zhang, Y. Nakamura, K. Furukawa, T. Hiraki, J. H. Yang, T. Funatsu, I. Ohdomari, and H. Kawarada. *Phys. Rev. E*, 74:041919, 2006.

[154] G. Speranza, L. Minati, and M. Anderle. *J. Appl. Phys.*, 102:043504, 2007.

[155] p. Kevin and M. R. Frederic. *Ann. Rev. Biochem.*, 46:223, 1977.

[156] I. Migneault, C. Dartiguenave, M. J. Bertrand, and K. C. Waldron. *BioTechniques*, 37:790, 2004.